



Politecnico di Bari

Repository Istituzionale dei Prodotti della Ricerca del Politecnico di Bari

Improved pre-processing techniques to enhance the accuracy of extracted information from passive satellite data

This is a PhD Thesis

Original Citation:

Improved pre-processing techniques to enhance the accuracy of extracted information from passive satellite data / Novelli, Antonio. - (2017). [10.60576/poliba/iris/novelli-antonio_phd2017]

Availability:

This version is available at <http://hdl.handle.net/11589/100176> since: 2017-03-24

Published version

Politecnico di Bari
DOI: 10.60576/poliba/iris/novelli-antonio_phd2017

Terms of use:

Altro tipo di accesso

(Article begins on next page)



POLITECNICO DI BARI

D.R.R.S

Doctor of Philosophy in Environmental and
Building Risk and Development

Coordinator: Prof. Michele Mossa

XXIX CYCLE
Curriculum: Environment and Natural Re-
sources

DICATECh

Department of Civil, Environmental, Building
Engineering and Chemistry

**Improved pre-processing techniques to
enhance the accuracy of extracted
information from passive satellite data**

Prof. Eufemia Tarantino
Department of Civil, Environmental,
Building Engineering and Chemistry
Politecnico di Bari

Prof. Manuel Angel Aguilar Torres
Departamento de Ingeniería
Escuela Superior de Ingeniería
Universidad de Almería

PhD Candidate: Antonio Novelli

Abstract English

In this thesis, the attention was focused on the enhancement of the pre-processing stage for passive remotely sensed data. The proposed enhancements were firstly related to a single land cover class and then to the relative radiometric corrections of passive multispectral satellite data. The first of the two big chapters was related to the extraction of Plastic Covered Greenhouse (PCG) and to the development of new procedures and tools that demonstrated their usefulness by achieving high accuracies. Although the specific LC considered, the solutions showed in this chapter can be considered valid also in other environments.

In the second chapter a new algorithm is proposed for PIF (Pseudo Invariant Features) extraction and relative radiometric normalization. The new Threshold Relative Radiometric Correction Algorithm (TRRCA) can be labelled as a supervised one and combines three methods for the detection of PIF: Moment distance index (MDI), Normalized Difference Vegetation Index (NDVI) masks, morphological erosion and dilate operators. To prove its effectiveness, the algorithm was tested by using L8 scenes in different environments over the world. Lastly, the results achieved with the TRRCA were compared with the well-known IR-MAD (Iteratively Reweighted Multivariate Alteration Detection). These comparisons have shown that the proposed algorithm can be a valid, and in some cases better, alternative to existing approaches.

key words: Pre-processing; Relative Radiometric Correction; Plastic Cover Greenhouse; OBIA; Sentinel-2; Landsat 8

Abstract Italiano

L'obiettivo di questa tesi è il miglioramento della fase di pre-processing per dati satellitari telerilevati passivi. I miglioramenti proposti sono stati in primis rivolti ad una singola classe di copertura del territorio e, in seguito, alla generale correzione radiometrica relativa di dati satellitari multispettrali passivi. Il primo dei due grandi capitoli è connesso alla problematica dell'estrazione coperture plastiche in ambito agricolo e allo sviluppo di nuove procedure e strumenti che hanno dimostrato la loro efficacia ottenendo elevate accuratezze nei risultati. Sebbene i risultati ottenuti nel primo capitolo siano specifici per una singola classe di copertura dei suoli, le soluzioni ottenute possono essere considerate valide anche per problematiche simili ma relative ad altre classi di copertura.

Nel secondo capitolo è stato proposto un nuovo algoritmo per l'individuazione di PIF (pseudo invariant features) e correzione radiometrica relativa di dati satellitari passivi. Il nuovo algoritmo (TRRCA, Threshold Relative Radiometric Correction Algorithm) può essere definito come un algoritmo supervisionato che combina tre metodi per il rilevamento dei PIF: Momentum Distance Index (MDI), maschere di Normalized Differenced Vegetation Index (NDVI), operatori morfologici di erosione e dilatazione. Per testare l'efficacia dell'algoritmo TRRCCA sono state selezionate scene satellitari L8 acquisite in differenti regioni sparse per il mondo. Infine, i risultati ottenuti con l'algoritmo TRRCA sono stati confrontati con il celeberrimo algoritmo IR-MAD (Iteratively Reweighted Multivariate Alteration Detection) mostrando come l'algoritmo proposto possa essere una valida, e in alcuni casi migliore, alternativa agli approcci esistenti.

key words: Pre-processing; Relative Radiometric Correction; Plastic Cover Greenhouse; OBIA; Sentinel-2; Landsat 8

Index

Abstract English	3
Abstract Italiano	4
Acronyms	7
Figures	10
Tables	12
Equations	13
INTRODUCTION.....	16
CHAPTER 1: The extraction of Plastic Covered Greenhouse.....	18
1.1 Introduction	18
1.1.2 Introduction: Pixel-based approach.....	20
1.1.3 Introduction: OBIA approach.....	21
1.2 Related works	22
1.3 Study areas	25
1.4 Satellite data bands.....	27
1.5 Pixel-based Approach	29
1.5.1 Pixel-Based Approach: Defining ad hoc normalized difference indices to extract plastic cover surfaces.....	31
1.5.2 Pixel-Based Approach: Using binary confusion matrixes for extracting plastic covered areas	34
1.5.3 Pixel-Based Approach: Results	36
1.6 OBIA approach: dataset.....	38
1.6.1 OBIA approach: segmentation stage.....	39
1.6.2 OBIA approach: Segmentation quality assessment	40
1.6.3 OBIA approach: Training set and Features extraction.....	44
1.6.4 OBIA approach: Random Forest classifier design and classification accuracy assessment.....	45
1.6.5 OBIA approach: Segmentation procedure result.....	49
1.6.6 OBIA approach: Random Forest classifier results.....	51

1.7 OBIA approach: AssesSeg, a command line tool to assess the quality of segmentations 56

1.7.1 OBIA approach: AssesSeg 57

1.7.2 OBIA approach: AssesSeg output results..... 61

ACKNOWLEDGEMENTS Chapter 1 66

REFERENCES of Chapter 1 67

CHAPTER 2: A new Threshold Relative Radiometric Correction Algorithm (TRRCA) of Multiband Satellite Data..... 75

2.1 Introduction..... 76

2.2 Pseudo-Invariant Features Extraction 78

2.3 Study Areas and Dataset..... 81

2.4 Proposed algorithm 86

2.4.1 Morphological operators 88

2.4.2 Vegetation Mask..... 89

2.4.3 Moment Distance Index mask 90

2.4.4 Radiometric Normalization coefficients estimation and selection of potentials high quality PIF extraction..... 92

2.4.5 The IR-MAD correction algorithm 95

2.5 TRRCA application and comparisons with IR-MAD algorithm 97

2.5.1 TRRCA tests results 98

2.5.2 Comparisons with the IR-MAD algorithm 112

ACKNOWLEDGEMENTS Chapter 2 121

References of Chapter 2 122

Conclusions..... 129

European curriculum vitae format..... 132

Acronyms

Band Combinations (BC)
Bottom Of Atmosphere (BOA)
Canonical Correlation Analysis (CCA)
Coefficient of Determination (R²)
Correlation Coefficient (r)
Corresponding Segment (CS)
Decision Tree (DT)
Digital Elevation Model (DEM)
Egyptian (E)
Enhanced Thematic Mapper plus (ETM+)
Euclidean Distance 2 (ED2)
Extraction and Classification of Homogeneous Objects (ECHO)
Ground Control Points (GCPs)
Ground Sample Distance (GSD)
High Quality PIF (HQ-PIF)
Independent Check Points (ICPs)
Italian (I)
Iteratively Reweighted Multivariate Alteration Detection (IR-MAD)
Kappa Index of Agreement (KIA)
Land Cover (LC)
Landsat 8 (L8)
Left Pivot (LP)
Level 1C (L1C)
Level 2 data (L2A)
Maximum Likelihood (MLC)
Moment Distance Index (MDI)
Multi Spectral (MS)
Multi Spectral Instrument (MSI)
Multi-Resolution Segmentation (MRS)
Nepalese (N)
Normalized Difference Sandy Index (NDSI)
Normalized Difference Vegetation Index (NDVI)
Number-of-Segments Ratio (NSR)
Object Based Image Analysis (OBIA)
Reference Objects (ROs)
Operational Land Imager (OLI)
Ortho Ready Standard Level-2A (ORS2A)
Orthogonal Distance Regression (ODR)
Overall Accuracy (OA)

Panchromatic (PAN)
PIF normalized (PIF_{norm})
Pixel-Based (PB)
Plastic Covered Greenhouse (PCG)
Plastic Surface Index (PSI)
Potential Segmentation Error (PSE)
Producer's Accuracy (PA)
Pseudo Invariant Features (PIF)
Quality Assessment (QA)
Random Forest (RF)
Reference (R)
Relative Radiometric Normalization (RRN)
Rescaled Brightness Temperature (T_{bres})
Right Pivot (RP)
Root Mean Square Error (RMSE)
Scale Parameter (SP)
Sentinel-2 (S2)
Target (T)
Spanish (S)
Thematic Mapper (TM)
Thermal Infrared Sensor (TIRS)
Threshold Relative Radiometric Correction Algorithm (TRRCA)
Top Of Atmosphere (TOA)
User's Accuracy (UA)
WorldView-2 (WV2)

Satellite bands

Blue (B)
Cirrus (CI)
Coastal (C)
Coastal Aerosol (CA)
Green (G)
Near Infrared (NIR)
Near Infrared-1 (NIR1)
Near Infrared-2 (NIR2)
Red (R)
Shortwave Infrared-1 (SWIR1)

Shortwave Infrared-2 (SWIR2)
Water Vapor (WV)

Figures

Figure 1. The Study area (RGB visualization) within the Province of Taranto in the Apulia Region (Southern Italy). Reference System: UTM WGS84 Zone 33N.	26
Figure 2. Location of the Spanish study area depicted by means of the Red band of the Sentinel-2 image. Coordinate system: ETRS89 UTM Zone 30N	27
Figure 3. Examples of sampled pixels (in a RGB visualization) belonging to plastic covered areas collected for the four L8 scenes of the Apulian test area.	30
Figure 4. Mean values of sampled pixels over the four subsets for the Apulian test Area (Pixel-Based approach). The thermal channel was used only for plastic covered areas to enhance their detection.	33
Figure 5. Pixel-Based method: Results for a small sample area related to the A, B, C, D subsets visualized in RGB to enhance the presence of plastic covers and in white to show the final detected areas.	37
Figure 6. Pixel-Based method: Results for a small urban/rural sample area related to the A, B, C, D subsets visualized in RGB to enhance the presence of plastic covers and in white to show the final detected objects mixed with false positive areas.	37
Figure 7. Discrepancies examples between reference polygon and corresponding segments: (a) one reference polygon vs. many corresponding segments; (b) one reference polygon vs. one corresponding segments; (c) many reference polygon vs. many corresponding segments. Source (Liu et al. (2012)).	42
Figure 8. OBIA Approach: Manually digitized ground truth of the whole study area. Coordinate system: ETRS89 UTM Zone 30N.	48
Figure 9. OBIA Approach: Visual comparison over the WV2 orthoimage (RGB visualization) of different best segmentations depending on the image data: a) best estimate L8-based segmentation; b) best estimate S2-based segmentation; c) best estimate WV2-based segmentation. Coordinate system: ETRS89 UTM Zone 30N.	50
Figure 10. OBIA Approach: Comparisons of the best classification results for the four considered combinations. Coordinate system: ETRS89 UTM Zone 30N.	53
Figure 11. AssesSeg procedure implemented for each geometry (that respects the overlapping criteria) within an output segmentation file.	57
Figure 12. AssesSeg command line output.	58
Figure 13. Looping process tree designed with eCognition in order to obtain input segmentation files for AssesSeg computations.	60
Figure 14. OBIA Approach: Scatter plots ED2- Number of Reference Objects. Computation executed with AssesSeg.exe.	64
Figure 15. OBIA Approach: 95 % Confidence intervals computed from the scatterplots depicted in Figure 14.	65
Figure 16. Reference-Italian (R-I) and Target-Italian (T-I) scenes used in this study. Coordinate System UTM WGS 84 zone 33N.	83

Figure 17. Reference-Nepalese (R-N) and Target-Nepalese (T-N) scenes used in this study. Coordinate System UTM WGS 84 zone 45N.....	83
Figure 18. Reference-Spanish (R-S) and Target-Spanish (T-S) scenes used in this study. Coordinate System UTM WGS 84 zone 30N.	84
Figure 19. Reference- Egyptian (R-E) and Target- Egyptian (T-E) scenes used in this study. Coordinate System UTM WGS 84 zone 35N.....	84
Figure 20. Flowchart of the proposed PIF extraction method.	87
Figure 21. Schematic diagram of MDI applied on a sample spectral reflectance curve of a green vegetation. Note that the number of points between LP and RP pivots can vary depending on the number of bands analyzed or the width of the pivot wavelength region (source Salas et al., 2016).	91
Figure 22. Scatter plots for the Italian study area.	102
Figure 23. Scatter plots for the Nepalese study area.....	104
Figure 24. Scatter plots for the Spanish study area.....	107
Figure 25. Scatter plots for the Egyptian study area.....	109
Figure 26. Comparison of RGB visualizations of Reference (R) image (on the left) and corrected Target (T) image (on the right) with overlapped PIF. a) Italian test area (I) (Coordinate System UTM WGS 84 zone 33N); b) Nepalese (N) test area (Coordinate System UTM WGS 84 zone 45N); c) Spanish (S) test area (Coordinate System UTM WGS 84 zone 30N); d) Egyptian (E) test area (Coordinate System UTM WGS 84 zone 35N).	114

Tables

Table 1. Landsat 8 OLI and TIRS scenes used in the Pixel-Based approach proposed in this Chapter.	29
Table 2. Ranges of the investigated thresholds for each proposed index implemented in the Pixel-Based approach.	34
Table 3. Combination of the index thresholds with the highest OA achieved for the PB Method	36
Table 4. Sentinel-2 (S2) and Landsat 8 (L8) object based features (feat.)	46
Table 5. OBIA Approach: Best estimate ED2 values and their associated input bands and Scale, Shape and Compactness parameters.	49
Table 6. OBIA Approach: Achieved OA, KIA, PA and OA for the considered classifications. These results should be understood as true accuracies, and not as estimated ones, since they were computed using a ground truth comprising the whole working area.	52
Table 7. OBIA Approach: Importance of the best ten features achieved for the best L8 classifications.	55
Table 8. OBIA Approach: Importance of the best ten features achieved for the best S2 classifications.	55
Table 9. OBIA Approach: Modified ED2 and its associated scale parameter (shape and compactness were fixed to 0.5) for the tested Sentinel-2 (S2) and Landsat 8 (L8) equal-weighted band combinations. Computation executed with AssesSeg.exe	62
Table 10. OBIA Approach: Modified ED2 and its associated scale and shape parameters (compactness was fixed to 0.5) for the tested Sentinel-2 (S2) and Landsat 8 (L8) equal-weighted band combinations. In grey, the best results achieved. Computation executed with AssesSeg.exe	62
Table 11. OBIA Approach: Modified ED2 and its associated scale and shape parameters (compactness was fixed to 0.5) for the tested WorldView2 (WV2) equal-weighted band combinations. In grey, the best results achieved. Computation executed with AssesSeg.exe	63
Table 12. Reference (R) and Target (T) scenes used in this study for the Italian (I), Nepalese (N), Spanish (S) and Egyptian (E) test areas.	85
Table 13. Landsat 8 Operational Land Imager (OLI) bands.	86
Table 14. Thresholds used to test the influence of <i>MNDVI</i> in different environment. The showed Interval of values are open intervals with a step of 0.05.	90
Table 15. Results over an ideal no-change condition in which all the pixels in Reference and Target scenes are PIF.	95
Table 16. Number of High Quality PIF (HQ-PIF) extractions for the selected Italian (I), Nepalese (N), Spanish (S) and Egyptian (E) test areas.	99

Table 17. Implemented thresholds and kernel size for the selected Italian (I), Nepalese (N), Spanish (S) and Egyptian (E) test areas. These parameters were the input of the proposed method implemented in the comparisons with the IR-MAD algorithm.	112
Table 18. Number of TRRCA HQ-PIF for the selected Italian (I), Nepalese (N), Spanish (S) and Egyptian (E) test areas compared with IR-MAD number of PIF at 99% and 95% of no-change probability.	113
Table 19. Italian (I) test area: Evaluated band-by-band gain, offset, correlation r and RMSE. F p-value, t p-value, W p-value are p-values for the two sample F test, two sample t test and the Wilcoxon rank sum test. The result h = 1 indicates a rejection of the null hypothesis, and h = 0 indicates a failure to reject the null hypothesis at the 5% significance level.	117
Table 20. Nepalese (N) test area: Evaluated band-by-band gain, offset, correlation r and RMSE; F p-value, t p-value, W p-value are p-values for the two sample F test, two sample t test and the Wilcoxon rank sum test. The result h = 1 indicates a rejection of the null hypothesis, and h = 0 indicates a failure to reject the null hypothesis at the 5% significance level.	118
Table 21. Spanish (S) test area: Evaluated band-by-band gain, offset, correlation r and RMSE; F p-value, t p-value, W p-value are p-values for the two sample F test, two sample t test and the Wilcoxon rank sum test. The result h = 1 indicates a rejection of the null hypothesis, and h = 0 indicates a failure to reject the null hypothesis at the 5% significance level.	119
Table 22. Egyptian (E) test area: Evaluated band-by-band gain, offset, correlation r and RMSE; F p-value, t p-value, W p-value are p-values for the two sample F test, two sample t test and the Wilcoxon rank sum test. The result h = 1 indicates a rejection of the null hypothesis, and h = 0 indicates a failure to reject the null hypothesis at the 5% significance level.	120

Equations

Equation 1. Sampled plastic covered pixels by means of quality assessment band.	31
Equation 2. Rescaled brightness temperature	32
Equation 3. Normalized green Difference Vegetation Index.	32
Equation 4. Plastic Surface Index (PSI) equation.	33

Equation 5. Normalized Difference Sandy Index (NDSI) equation.....	34
Equation 6. I-th Mask definition for the Pixel-Based approach.	34
Equation 7. Plastic Surface Extraction equation for the Pixel-Based approach.	34
Equation 8. Euclidean Distance 2 Equation.....	43
Equation 9. Potential Segmentation Error Equation.	43
Equation 10. Number-of-Segment Ratio Equation.....	43
Equation 11. New Potential Segmentation Error Equation.	43
Equation 12. New Number-of-Segment Ratio Equation	43
Equation 13. Linear equation between reference and target.	77
Equation 14. TOA reflectance Equation.	85
Equation 15. TOA reflectance equation corrected with the sun elevation angle.	86
Equation 16. TRRCA equation.	87
Equation 17. Candidate Bright PIF.	88
Equation 18. Candidate Dark PIF.	88
Equation 19. Morphological Dilation for the reference scene.	88
Equation 20. Morphological Dilation for the target scene.	88
Equation 21. Morphological Erosion for the reference scene.	88
Equation 22. Morphological Erosion for the target scene.	88
Equation 23. Morphological mask.	89
Equation 24. NDVI equation.	89
Equation 25. Mask NDVI equation.....	90
Equation 26. Moment distance from the left pivot.	92
Equation 27. Moment distance from the right pivot.....	92
Equation 28. Moment distance index.....	92
Equation 29. Mask MDI equation.	92
Equation 30. ODR variables definition.....	93
Equation 31. Relationship between true and observed values equations.....	93
Equation 32. Orthogonal distance equation of residual.	93
Equation 33. α and β equations: potential quality parameter terms.	95
Equation 34. linear band combinations of two considered images.	96
Equation 35. Two generalized eigenvalue problems.	96
Equation 36. MAD Variates.	96
Equation 37. Sum of squares of uncorrelated and normally distributes random variables.	97

INTRODUCTION

In the last decades, the technical and research communities have seen an enormous increasing of geospatial/geolocated data. Land use, fauna and flora, permanent ice monitoring, drought, traffic and cultural heritage need a constant and multitemporal monitoring. Coupled with the increased availability of resources there is the need for timely and accurate information about the type, quantity, and extent of them.

For example, to assess the risk and plan effective emergency response, is important to know the position of roads to fire and police stations, hospitals, and emergency shelters; for rare species is important to improve the habitat conditions and to know: what the habitat constraints are, where a specific habitat is located, where one or more species lives and how variations to the habitat (and its neighbourhoods) could possibly interact with species distribution. It is clear that the understanding of the location and distribution of resources over time is crucial to plan an effective management of them.

The simplest way to represent geolocated information is with maps. Maps can provide a measure of the extent, location and density of resources. However, a map can be considered as a model (Reddy, 2008) that for its conception reduces the complexity of the real world. The use of geolocated information inevitably introduces errors and the problem of the accuracy of the information that we are using.

From this point of view, the accuracy of any spatial data set is a combination of both positional and thematic accuracy. In particular, the problem of the accuracy and of the extraction of reliable information is not negligible when economic resources can be saved because of this. However, because the thematic accuracy is much more complex than the positional accuracy (Congalton and Green, 2008) this thesis work was mainly focused on the first one and in the enhancement of data pre-processing in order to extract high quality thematic information from processed data.

In this thesis, the improvement of the pre-processing of the satellite data is correlated to the retrieval of information stored in them data but not directly usable. This topic was analysed within two different themes, described in two big chapters. The first one is related to the enhancement of plastic covered greenhouse extraction and the second one on relative radiometric corrections of satellite data.

In the first chapter the extraction of thematic information is the main topic. Both pixel and Object Based Image Analysis (OBIA) approaches were tested. Particularly, innovative tools and procedures were implemented and directly developed for this purpose adding a scientific contribute in the related field. This chapter takes also into account the geometric accuracy of the extracted areas and the development of an executable tool to assess the geometric accuracy after a digital image segmentation process. Although the procedure and tools showed in this chapter are related to plastic greenhouse extraction, the achieved results and the showed methods can be considered valid also in other environments.

The second chapter adds a contribute in the field of pre-processing for change detection analysis. A new and performant relative radiometric normalization algorithm was developed and tested. The algorithm is related to the retrieval of pseudo invariant features between two multitemporal satellite images with a novel method and then compared with the most well-known relative radiometric correction algorithm.

Each chapter will be organized with its own introduction and description of the implemented data, chosen test areas, methods and results. This was necessary to properly introduce each exanimated topic and to show the application of the developed procedures and tools. The theory and methods that were not directly developed during this thesis work will be introduced only if strictly necessary. Indeed, a rich bibliography is provided in order to build a strong theoretical framework for the two chapters.

It is worth noting that part of the material showed in this thesis was already published in prestigious journals and as conferences proceedings with a peer review process.

CHAPTER 1: The extraction of Plastic Covered Greenhouse

In this first chapter are showed procedures and new methods to enhance the detection of a specific Land Cover (LC) typology. The effort was focused on the extraction of Plastic Covered Greenhouse (PCG) and in the development of new procedures and tools that demonstrated their usefulness by achieving high accuracies. Indeed, the spread of agricultural plastic coverings is a consequence of their positive impact on plants protected by their action. This, along with an equivalent positive impact on the local economy, explains why plastic coverings have become a common practice in some agricultural fields. On the other hand, plasticulture raises both environmental and landscape issues. Since agriculture is one of the most important economic activities of the examined study areas, a detailed site mapping is crucial both for the protection of the local economy and for the preservation of local environment and landscape. To this purpose:

- Four normalized difference indices were combined to extract PCG with Landsat 8 (L8) data;
- Were compared for the first time the performance between Sentinel-2 (S2) Multi Spectral Instrument (MSI) and L8 Operational Land Imager (OLI) headed up to greenhouse detection;
- Were developed and described the capabilities of a command line tool created to assess the quality of segmented digital images.

Although the specific LC considered, the solutions showed in this chapter can be considered valid also in other environments. Lastly, it is worth noting that part of the showed results were already published in peer reviewed journals (Novelli and Tarantino, 2015a, Novelli et al., 2016a, Aguilar et al., 2016c).

1.1 Introduction

Environmental modelling and spatial planning need the development of operational tools able to simplify the extraction of information from available data. This is especially true when the considered data are remotely sensed and the extracted information has an economic relevance (Blaschke, 2010).

This chapter is focused on the extraction of PCG. Plastic polymers have been extensively used in agriculture. Nowadays "plasticulture" (Lamont, 1996) is the term that specifies an agricultural practice in which plastic polymers are used to protect specific plantation. All over the world plasticulture applications range from plastic mulch film, row coverings, high and low tunnels, to plastic greenhouses (Espí et al., 2006). Although the implementation of plastic coverings in agricultural practices produces positive effects (especially in semi-arid environments), its widespread has negative consequences on the original landscape (Briassoulis et al., 2013). Indeed, plastic coverings alter the natural rainwater paths on the soil affecting both recharge and quality of groundwater. A typical effect caused by plastic covered areas is the concentration of the rainwater along the borders and the strips of fields, precluding water infiltration. This particular circumstance increases the probability of rainwater runoff to the detriment of groundwater recharge. Since agriculture is one of the most important economic activities within the analysed study areas, its adequate monitoring is necessary in order to avoid an uncontrolled development (and its related consequences) of rural areas (Aguilar et al., 2014, Picuno et al., 2011, Tarantino and Figorito, 2012).

Due to its peculiar characteristics, remote sensing PCG mapping is far to be solved (Agüera et al., 2008, Agüera et al., 2006, Aguilar et al., 2014, Levin et al., 2007, Tarantino and Figorito, 2012) as demonstrated by the increasing number of scientific works produced in the last decade (see section 1.2). In fact, different plastic materials with varying thickness, transparencies, ultraviolet and infrared reflection and transmission properties, additives, age and colours add complexity in PCG detection. Moreover, as plastic sheets are semi-transparent, the changing reflectance of the crops underneath them affects the greenhouse spectral reflectance itself (Levin et al., 2007).

The topic of PCG extraction is relevant with passive remotely sensed data with which PCG detection has been carried out through two main approaches: Pixel-Based (PB) and Object Based Image Analysis (OBIA). In this chapter the main focus will be on the enhancement of PCG detection by means of OBIA, although will be shown also how to

exploit an artefact within the L8 Quality Assessment (QA) band to extract PCG in a pixel-based approach.

On the other hand, when there is the need to extract a particular LC by means of an OBIA procedure, it is important to point out two critical issues. Firstly, the shape of the real individual objects (in this case PCG) should be represented in the best way by the segments to classify; then the classification should be simple, accurate, robust, temporally stable and fast. This means that geometrically accurate segments should be identified by means of a small training sample size or even without training. Many reasons justify the use of an OBIA approach (e.g. geometric and neighbourhood information availability, reduction of salt and pepper effect in classifications, etc.). A general review of pros and cons of OBIA can be found in Blaschke (2010) and Blaschke et al. (2014). In this chapter the segmentation stage was performed by means of the Multi-Resolution Segmentation (MRS) algorithm (Baatz and Schäpe, 2000) included in the eCognition Developer software (Trimble, Sunnyvale, California, United States). MRS is one of the most widely used methods to perform image segmentation (Blaschke, 2010) and has already been successfully performed on plastic greenhouses by Tarantino and Figorito (2012) and Wu et al. (2016). However, in both cases the key parameters of the algorithm (scale, shape and compactness) were set up with a trial-and-error approach only validated by visual inspection. Indeed, it is important to note that segmentation quality evaluation controls the quality of the whole OBIA workflow. Among a variety of segmentation evaluation methods and criteria, discrepancy measurement is believed to be the most useful and is therefore one of the most commonly employed techniques in many applications (Clinton et al., 2010, Liu et al., 2012, Yang et al., 2015).

1.1.2 Introduction: Pixel-based approach

In this thesis work a PB approach was tested to produce a fast PCG extraction. For this last proposed method, also L8 Thermal Infrared Sensor (TIRS) data were implemented. Commonly, satellite TIRS data are used for retrieving land surface temperature (Bai et al.,

2015) and sea surface temperature (Tarantino, 2012). Yet TIRS data can also be used as ancillary information to better discriminate surfaces with similar spectral response, hardly ever recognizable when applying the most consolidated methods (Crocetto and Tarantino, 2009). With regard to PGC, in-situ thermal data are generally necessary to study and assess growing conditions, air flow and evapotranspiration and to define experiment conditions (Villarreal-Guerrero et al., 2012).

For the implemented PB approach the conjunct use of four normalized difference indices were proposed: the Normalized Difference Vegetation Index (NDVI) green index and three spectral indices purposely created for this study (rescaled brightness temperature, Plastic Surface Index and Normalized Difference Sandy Index) (Novelli and Tarantino, 2015a, Novelli and Tarantino, 2015b). In the PB approach the preliminary QA band analysis was found to be crucial in the sampling process of plastic covered surfaces. Lastly, this is the first work that exploited the L8 QA band for PCG extraction.

1.1.3 Introduction: OBIA approach

PCG extraction through OBIA considered the above mentioned problems (see section 1.1). Particularly, the focus was related to the evaluation of performances, in PCG extraction, between the two free of charge sensor L8 OLI and S2 MSI (Novelli et al., 2016a). This is the first time in which is proposed both a comparison regarding PCG detection between satellite data provided by the novel Sentinel-2A (S2) MSI and L8 OLI. Moreover, in this work S2 MSI Level 1C data (L1C, top of atmosphere reflectance) were atmospherically corrected (bottom of atmosphere reflectance values) by means of the Sen2Cor algorithm (Muller-Wilm et al., 2013) to generate a S2 MSI L2A product (Level 2 data). This is one of the first work to implement such user generated product. In fact, recent literature has shown many studies with simulated S2 MSI data but at the moment, only a few scientific papers have dealt with S2 MSI data (e.g. Du et al. (2016), Immitzer et al. (2016), Fernández-Manso et al. (2016), Pesaresi et al. (2016)). However, in the above mentioned studies were used S2 MSI L1C data for vegetation classification purposes (Immitzer et al., 2016), for

burn severity discrimination (Fernández-Manso et al., 2016), to detect build-up areas (Pesaresi et al., 2016) and to map water bodies (Du et al., 2016).

The proposed comparisons were undertaken by applying an OBIA approach coupled with Random Forest (RF) classifier (Breiman, 2001). Moreover, a further improvement was proposed for the segmentation quality assessment by means of discrepancy measurements. Specifically, this was achieved from a modified version of the Euclidean Distance 2 (ED2) index originally proposed by Liu et al. (2012). Besides the S2 and L8 based segmentations, it was also considered a more accurate segmentation obtained from a higher resolution WorldView-2 (WV2) image. In this sense, WV2 segmentation was employed as the basis to test the differences between S2 and L8 classification results connected to their only informative content. Very high Overall Accuracy (OA) values were obtained testing four different RF classification schemes by using a very small training set: L8 features with L8-based segmentation, L8 features with WV2-based segmentation, S2 features with S2-based segmentation and S2 features with WV2-based segmentation.

Lastly, in this chapter will be showed also the capability of a created command line tool (AssesSeg) that implements the above mentioned modified version of the supervised discrepancy measure ED2. Indeed, scientific literature proposes different methods to assess the segmentation quality both from unsupervised and supervised approaches (e.g. Drăguț et al. (2014), Liu et al. (2012)). However, in remote sensing OBIA applications, the proposed methods are not always coupled with tools able to automatically compute the described metrics. Specifically, in this thesis work, AssesSeg.exe was used to detect the best Band Combinations (BCs) for PCG detection from the three multispectral satellite data (S2, L8 and WV2).

1.2 Related works

Over the last decade, greenhouse detection has mainly been addressed by using different PB approaches supported by single satellite data, such as Landsat Thematic Mapper (TM) (e.g. Picuno et al. (2011)), L8 OLI/TIRS (e.g. Novelli and Tarantino (2015b)), IKONOS or QuickBird (Agüera et al., 2008, Agüera et al., 2006, Arcidiacono and Porto, 2010,

Arcidiacono and Porto, 2012, Carvajal et al., 2010) and WV2 (Tasdemir and Koc-San, 2014, Koc-San, 2013, Pala et al., 2015).

Specifically, in the most recent works, Colby and Keating (1998) carried out different classifications on Landsat TM scenes in which greenhouses were one of the researched classes. Thunnissen and De Wit (2000) used Landsat TM and Spot XS data in the updating of the national LC/land-use of the Netherlands (LGN3). Greenhouses were one of the 39 classes obtained through an integrated procedure characterized by multitemporal satellite imagery and the support of digital and analogue ancillary data. Mesev et al. (2000) used a modification of the MLC, on Landsat TM data, to find the increasing of built up areas to the detriment of agricultural lands with a high percentage of greenhouses. A specific study on greenhouses coverage was carried out by Zhao et al. (2004) with the implementation of an index model on Landsat TM data. Agüera et al. (2006) tried different band combinations with a Maximum Likelihood (MLC) classifier in order to enhance the detection of greenhouses with QuickBird satellite data. SÖNMEZ and Sari (2006) carried out a study in which was created a GIS-based database for greenhouse in the Antalya region (Turkey). In that work, greenhouses fields were vectorised by visual analysis of Ikonos data. Carvajal et al. (2006) presented a methodology to detect greenhouses based on the use of an Artificial Neural Network classifier from QuickBird data. Capobianco and Picuno (2008) and Picuno et al. (2011) performed supervised classifications and GIS analysis on Landsat TM data to evaluate the landscape impact of agricultural plastic coverings. Agüera et al. (2008) used MLC and texture analysis in order to compare IKONOS and QuickBird satellite data in LC (especially plasticulture) detection. Agüera and Liu (2009) proposed MLC with Extraction and Classification of Homogeneous Objects (ECHO) to identify the borders of PCG using IKONOS and QuickBird data. Then the irregular contours belonging to polygons were converted into straight lines using an algorithm based on the Hough transform. Carvajal et al. (2010) implemented four increasing levels of atmospheric correction as pre-processing for greenhouse detection. They used QuickBird and Ikonos data and then showed the accuracy obtained related to the specific pre-processing. Arcidiacono C. and S.M.C. Porto described their experiences in crop-shelter classification in many works (Arcidiacono and Porto, 2010, Arcidiacono and Porto, 2007, Arcidiacono and Porto, 2012). Particularly in their experiments were used both digital aerial photographs and a QuickBird scene. The

results were carried out through unsupervised and supervised classifications, texture analysis and object-oriented classification. Koc-San (2013) compared three different classification techniques (MLC, random forest and support vector machine) in order to extract plastic and glass greenhouses. An unsupervised classification approach and Gabor features were followed by Tasdemir and Koc-San (2014) in greenhouses detection. Working with multitemporal imagery, Lu et al. (2014) achieved a very simple but consistent decision tree classifier for extracting transparent plastic-mulched landcover from a very short Landsat 5 TM time series composed of only two images during an agricultural season. They proposed a plastic-mulched LC index (PMLI) by using the reflectance of red band (b3) and SWIR1 (b5). Furthermore, also large time series of MODIS surface reflectance daily L2G (250 m ground sample distance) covering the cotton crop period from the 85th day to the 150th day of the year were used by (Lu et al., 2015) for plastic-mulched LC extraction and “A simple threshold model for plastic-mulched land cover” was designed. It was based on the temporal-spectral features in the early stage of a growing season and on the number of days after planting. The implemented discriminator was a NDVI threshold. This rule achieved very good results along three different years. Novelli and Tarantino (2015b) used both Landsat 8 OLI and TIRS data to propose a normalized difference index for agricultural plastic cover detection. They worked on a test area under simplified conditions (e.g. all non-agricultural pixels were excluded with a mask). Hasituya et al. (2016) monitored plastic-mulched farmland by a single Landsat 8 OLI image using spectral and textural features.

OBIA approach is much more recent. Tarantino and Figorito (2012) worked with OBIA and RGB aerial photographs. Particularly, the selection of the optimal segmentations parameters was performed by visual inspection. GeoEye-1 and WV2 stereo imagery were compared by Aguilar et al. (2014) in order to evaluate the enhancement in the extraction of greenhouses obtained from the combined use of spectral information, elevation data, band indexes and texture analysis. They showed that the elevation data was an important feature for greenhouse classification. Furthermore, a comparison between traditional per-pixel and OBIA greenhouse classification was carried out by Wu et al. (2016) achieving that the OBIA scheme resulted in significant improvement.

The latest recent works connected with this chapter are described in Aguilar et al. (2015) and Aguilar et al. (2016c). In Aguilar et al. (2015) the authors addressed the identification of greenhouse horticultural crops that were growing under plastic coverings. To this

end, OBIA and a Decision Tree (DT) classifier were applied to a L8 OLI time series and a single WV2 satellite image. They used a sample of 694 individual greenhouses whose information such as the type of crop, date of planting and date of removal were known. They achieved an OA of 81.3% identifying four of the most popular crops cultivated under greenhouse in Almería (Spain). However, in this research two important issues remained outstanding. On the one hand, the segmentation process (i.e., in that paper the authors decided to conduct a manual digitizing over the WV2 image to obtain the best possible segmentation on their 694 greenhouses). On the other hand, the authors did not deal with the greenhouse and non-greenhouse pre-classification (i.e., all the 694 segments had already been pre-classified as greenhouse).

In Aguilar et al. (2016c) was tested the combined use of very high resolution satellite data and multitemporal L8 OLI imagery using an OBIA approach to map and detect individual greenhouses through decision tree classifier. Particularly this is the first research work coping with this topic using OBIA techniques and L8 time series. Subjects regarding this specific topic are: (1) the identification of the optimal segmentation focused on individual greenhouses by means of segmentation evaluation methods; (2) the evaluation of the most important and useful features for plastic greenhouse detection (basic spectral information, textural features, several spectral and vegetation indices, seasonal statistics and spectral metric); (3) the comparison between the classification accuracies achieved from single satellite imagery and through time series; and lastly (4) the determination of a simple decision tree temporally stable by using robust threshold values based on L8 time series for greenhouse classification.

1.3 Study areas

The analysed study areas belong to the Province of Taranto in the Apulia Region (Southern Italy) and the Province of Almería in the southern Spain (Andalucía). Particularly, the Italian study area was used for the PB approach whereas the Spanish one for the OBIA proposed method.

The Italian study area (Figure 1) western and the eastern bounds are respectively within the municipalities of Ginosa and Palagiano, close to the Ionian Sea.

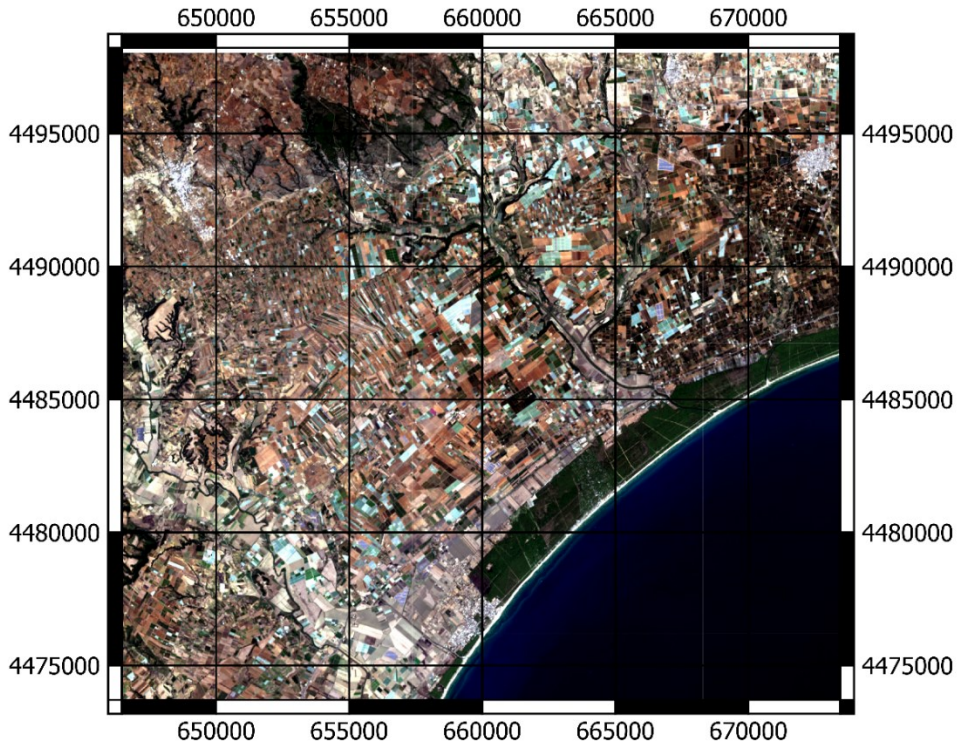


Figure 1. The Study area (RGB visualization) within the Province of Taranto in the Apulia Region (Southern Italy). Reference System: UTM WGS84 Zone 33N.

The dominant landscape in the northern part of the selected area is characterized by karst with moderate hills alternated with flat territory in the southern part of the area. The climate is semi-arid and typically Mediterranean: summers are hot and dry and winters are moderately cold and rainy (annual mean air temperature 16.28 °C, total annual precipitation 555mm). These conditions facilitate agriculture as the main productive activity. Common cultivations are vineyards, citruses, olives, stone fruits and summer vegetables. Particularly, vineyards grow using the traditional "tendone" technique (Picuno et al., 2011), a grape cultivation system with a supporting structure generally covered with plastic nets and plastic sheets. Plastic nets are fixed to the supporting structure to protect vineyards from adverse atmospheric conditions (such as wind and hail). Plastic sheets are placed above the nets

during the winter season to bring forward the harvest or during the summer season (August) to postpone the harvest. Since most of the Apulian grape cultivations implement plastic protections to postpone the harvest period, in this study only scenes of August or September were used.

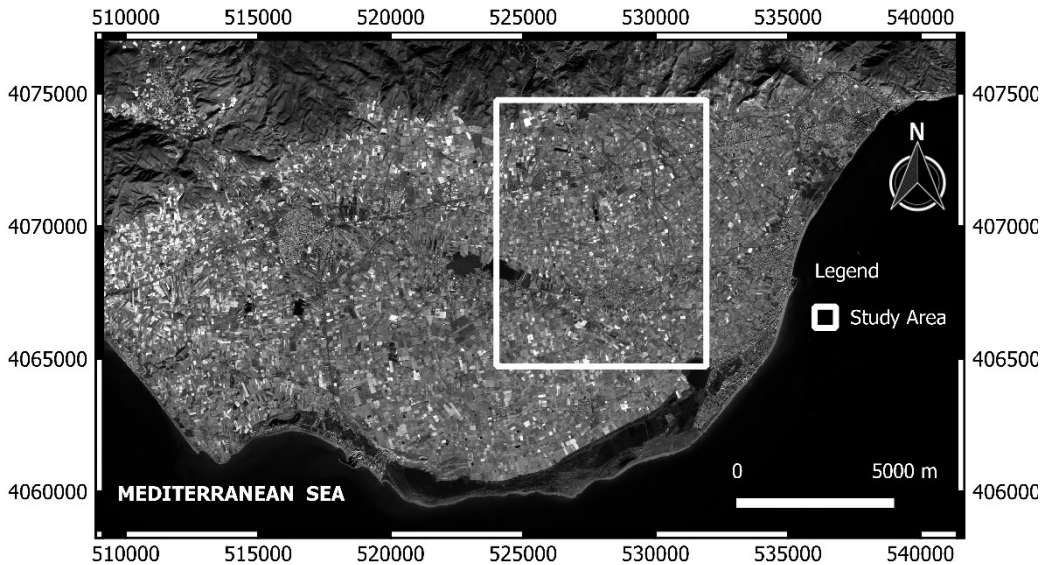


Figure 2. Location of the Spanish study area depicted by means of the Red band of the Sentinel-2 image. Coordinate system: ETRS89 UTM Zone 30N

The Spanish study area falls in Almería, southern Spain, which has become the site of the greatest concentration of greenhouses in the world, known as the “Sea of Plastic” or the “Poniente” region (Figure 2). The types of greenhouse plastic covers in the Spanish study area are very variable. The most common materials are polyethylene films (e.g., low density, long life, thermic, with or without additives) and ethylene-vinyl acetate copolymer, also known as EVA. Furthermore, both materials can present different thickness (180 μm or 200 μm) and colours (white, yellow or green). The intensive agriculture in Almería was mainly dedicated to tomato, pepper, zucchini, cucumber, aubergine, green bean, melon, watermelon and Chinese cabbage.

1.4 Satellite data bands

In this chapter were used three different satellite sensors data: L8, S2 and WV2.

The L8 satellite, launched in February 2013, carries a two-sensor payload, the OLI and the TIRS. The OLI sensor is able to capture eight multispectral (MS) bands with 30m Ground Sample Distance (GSD): coastal aerosol (CA, 430–450 nm), blue (B, 450–510 nm), green (G, 530–590 nm), red (R, 640–670 nm), near infrared (NIR, 850–880 nm), shortwave infrared-1 (SWIR1, 1570–1650 nm), shortwave infrared-2 (SWIR2, 2110–2290 nm) and cirrus (CI, 1360–1380 nm). In addition, L8 OLI presents one panchromatic band (P, 500–680 nm) with 15 m GSD and one QA band. The TIRS is able to capture two thermal infrared bands: TIRS1 (10600-11190 nm) and TIRS 2 (11500-12510 nm). The two bands are acquired at 100 m resolution and then resampled to 30 m in delivered data product. The L8 scenes were taken with a dynamic range of 12 bit and as level 1T data (for further details see Chapter 2).

WV2 is a very high resolution (VHR) satellite launched in October 2009. This sensor is capable of acquiring optical images with 0.46 m and 1.84 m GSD at nadir in panchromatic (PAN) and MS mode, respectively. Moreover, it was the first VHR commercially available 8-band MS satellite: coastal (C, 400–450 nm), blue (B, 450–510 nm), green (G, 510–580 nm), yellow (Y, 585–625 nm), red (R, 630–690 nm), red edge (RE, 705–745 nm), near infrared-1 (NIR1, 760–895 nm) and near infrared-2 (NIR2, 860–1040 nm). All delivered products were ordered with a dynamic range of 11-bit and without the application of the dynamic range adjustment pre-processing (for further details see OBIA sections).

The Sentinel-2A satellite was launched on 23 July 2015. MSI sensor collects up to thirteen bands with three different geometric resolutions: 60m, 20m and 10m. Coastal (C, 443 nm), water vapor (WV, 1375 nm) and cirrus (CI, 1376 nm) at 60 m resolution. Four red edge/NIR bands with central wavelength at 705 nm, 740 nm, 783 nm and 865 nm respectively, short wave infrared-1 (SWIR1, 1610 nm) and short wave infrared-2 (SWIR2, 2190 nm) at 20m resolution. Blue (B, 490 nm), Green (G, 560 nm), Red (R, 665 nm) and Near Infrared (NIR, 842 nm) at 10m resolution. The S2 MSI data was downloaded as Level 1C data and with a dynamic range of 12-bit (for further details see OBIA sections).

1.5 Pixel-based Approach

The proposed PB methodology was aimed at the fast extraction of agricultural plastic covered area under the hypothesis of lacking updated ancillary data (i.e. technical cartography) and using only free imagery. The method included the following steps: OLI and TIRS data pre-processing, the definition of normalized difference indices and surface extraction.

Acquisition date	Scene ID	Subset	Average Cloud Cover [%]
08 September 2013	LC81880322013251LGN00	A	1.56
07 August 2013	LC81880322013219LGN00	B	0.46
24 September 2014	LC81880322013267LGN00	C	0.31
10 August 2014	LC81880322014222LGN00	D	0.64

Table 1. Landsat 8 OLI and TIRS scenes used in the Pixel-Based approach proposed in this Chapter.

To this purpose four L8 scenes (OLI and TIRS data), along the same path-row, were processed (Table 1), considering the summer period in which the plastic cover density is the highest for the Italian study area. L8 OLI and TIRS sensors data can be freely selected through the USGS EROS website (<http://glovis.usgs.gov/>) and are nominally processed as Level 1 terrain corrected (L1T) (Roy et al., 2014b).

The OLI digital numbers of the four Landsat images were linearly converted to sensor Top Of Atmosphere (TOA) reflectance and then corrected for the sun angle using gains, offsets and local sun elevation values stored in each scene metadata (radiometric calibration). No atmospheric correction was performed to test the efficiency of the proposed PB approach apart from the local atmospheric noise and to reduce computation time.

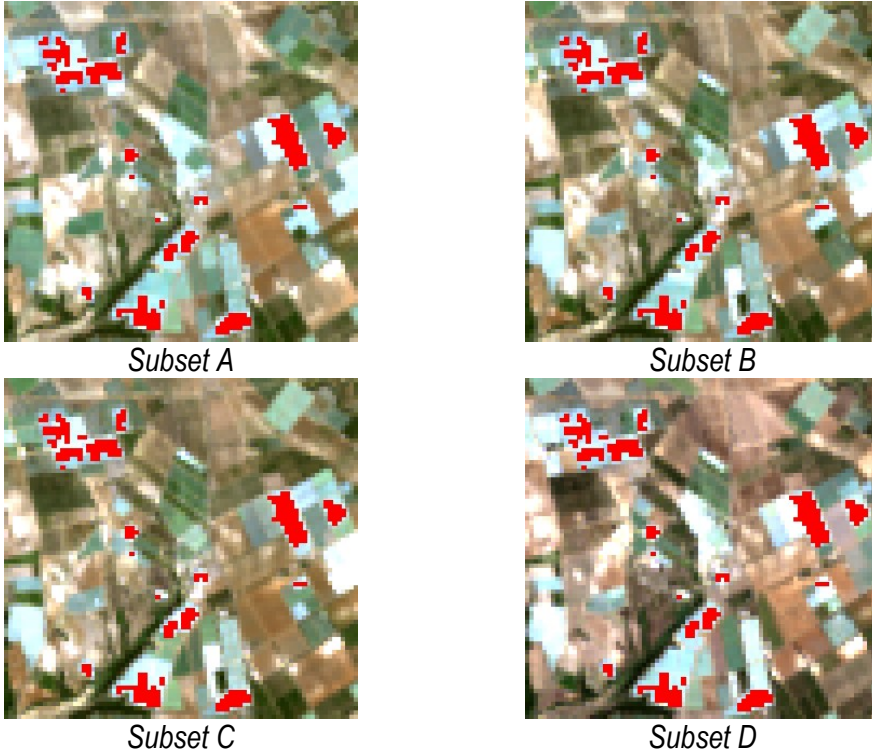


Figure 3. Examples of sampled pixels (in a RGB visualization) belonging to plastic covered areas collected for the four L8 scenes of the Apulian test area.

Landsat 8 OLI sensor data include a quality assessment (QA) band (Roy et al., 2014b). Each pixel in the QA band contains a decimal value that represents a bit-packed combination of surface, atmosphere and sensor conditions that can affect the overall usefulness of a given pixel. QA band's bits may improve the quality of scientific investigations and could be used to mask a raster file. Particularly, QA bands were used with that aim. Moreover, was tested their usefulness for possible contribution to the proposed approach. Nine different bands can be extracted for every QA band. Three of them are 1-bit bands (fill, dropped frame, terrain occlusion) and six of them are 2-bit bands (water, cloud shadow, vegetation, snow ice, cirrus, cloud). QA band data were unpacked through the L-LDOPE Toolbelt, a no-cost tool available from the USGS Landsat-8 website (Roy et al., 2002). In this case, all the nine bands were extracted at the default confidence level (34-66%) and only the Water and Cloud QA bands revealed a large occurrence in the study area.

The Water QA band showed a positive occurrence for luxuriant vegetation as well as for water. The Cloud QA band showed a positive occurrence not only for clouds but also for plastic covers and some urban areas. This last occurrence was found negligible if compared to the analogous agricultural plastic covered areas. The Cloud QA band misclassified pixels were exploited in the next phase of the procedure for time-saving in the sampling process of ground reference plastic covered areas. For this purpose, the pixels common in each scene were collected by intersecting the four Cloud QA bands. The results of this computation highlighted an evident connection between the Cloud quality band and agricultural plastic covered surfaces. Therefore, a slight manual input was required to sample more than 5000 pixels as ground reference for plastic covered areas starting from the pixels common to the four scenes (*Equation 1*).

$$\bigcap_{i=1}^4 \text{CQB}_i$$

Equation 1. Sampled plastic covered pixels by means of quality assessment band.

With CQB_i = i -th Cloud quality assessment band. *Figure 3* shows a subset of collected pixels by intersecting the four cloud QA bands (*Equation 1*).

With regards to L8 TIRS data, recent literature has shown the presence of some calibration problems related to Landsat 8 TIRS radiometric calibration for land surface temperature retrieval (Montanaro et al., 2014). This drawback was not considered because the first of the two TIRS channels was only used as ancillary information. Particularly, for each scene, TIRS data were converted to at-satellite brightness temperature using the constants and the logarithmic equation provided by the USGS EROS website.

1.5.1 Pixel-Based Approach: Defining ad hoc normalized difference indices to extract plastic cover surfaces

Four normalized difference indices were used to extract PCG areas. Normalized indices proved to be easy to compute and provided accurate results. Moreover, they performed better than a simple band ratio and, as dimensionless numbers, they were less

sensitive to local conditions within the scene. The general approach for such index typology is to find out the strongest and weakest bands for the interested LC type (Xu, 2010). Indeed, normalized difference bands combinations can maximize the contrast between the interested cover type and others areas (referred as noise). The four indices were used simultaneously to reduce the misclassification error between vegetation and bright plastic covered surfaces.

The first index (*Equation 2*) was created to rescale the brightness temperature domain by standardizing its values range with the OLI-TOA reflectance values which were defined into a closed interval [0;1].

$$T_{bres} = \frac{T_b - T_{bmin}}{T_{bmax} - T_{bmin}}$$

Equation 2. Rescaled brightness temperature .

where T_{bres} is the rescaled brightness temperature; T_b , T_{bmin} and T_{bmax} are respectively the brightness temperature, the maximum and the minimum brightness temperature values for each subset.

To better discriminate PCG areas from vegetation, the $NDVI_{green}$ (*Equation 3*) was implemented due to its better sensitivity to chlorophyll pigment (Gitelson et al., 2002, Rivero et al., 2009):

$$NDVI_{green} = \frac{\rho_{NIR} - \rho_{green}}{\rho_{NIR} + \rho_{green}}$$

Equation 3. Normalized green Difference Vegetation Index.

Where ρ_{NIR} and ρ_{green} are respectively the reflectances in the green and near infrared spectral bands.

The last two indices were created by using the information gained through sampled pixels with the aim to emphasize agricultural PCG areas and to highlight bright surfaces to be removed. A small group of pixels corresponding to sandy shore areas was manually collected as representative of high reflectance surfaces in the visible domain. *Figure 4* shows the mean values of the sampled pixels related to PCG areas and sandy areas for each considered channel.

For plastic covered areas, the strongest responses were in the NIR and in the Tbres channels while the weakest responses were in the red channel and in the SWIR2 (second shortwave infrared) band.

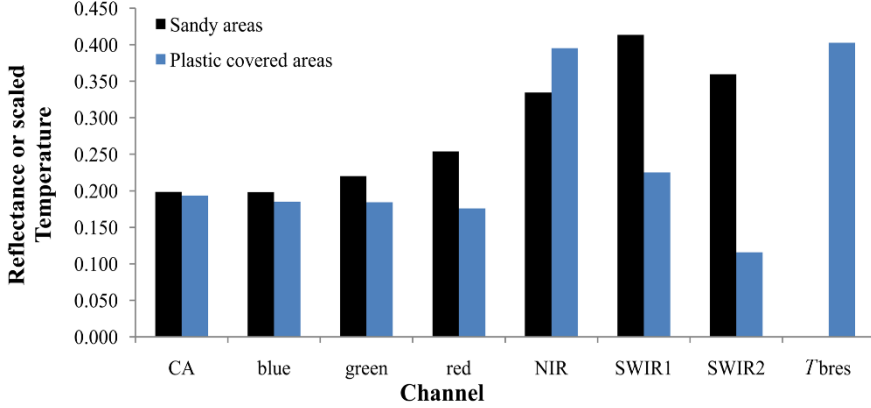


Figure 4. Mean values of sampled pixels over the four subsets for the Apulian test Area (Pixel-Based approach). The thermal channel was used only for plastic covered areas to enhance their detection.

High reflectance in the NIR band was not considered due to the high vegetation response in that channel. Based on the above assumptions, the most feasible channels for plastic covered areas were the Tbres, the Red and SWIR2 channels. The SWIR2 channel was combined with the Tbres channel through an arithmetic mean due to better results produced by this configuration. The formulation of Plastic Surface Index (PSI) (Novelli and Tarantino, 2015b) is shown in *Equation 4*.

$$PSI = \frac{\rho_{red} - \left(\frac{T_{bres} + \rho_{SWIR2}}{2} \right)}{\rho_{red} + \left(\frac{T_{bres} + \rho_{SWIR2}}{2} \right)}$$

Equation 4. Plastic Surface Index (PSI) equation.

The last created index involved the strongest response of the SWIR1 band and the weakest response of the Costal Aerosol (CA) band for the sandy areas. It was named Normalized Difference Sandy Index (NDSI) (Novelli and Tarantino, 2015a) and it assumed the following formulation (*Equation 5*):

$$NDSI = \frac{\rho_{SWIR1} - \rho_{CA}}{\rho_{SWIR1} + \rho_{CA}}$$

Equation 5. Normalized Difference Sandy Index (NDSI) equation.

1.5.2 Pixel-Based Approach: Using binary confusion matrixes for extracting plastic covered areas.

The above-mentioned indices were used to generate four binary raster masks (Equation 6). Then, the plastic cover extraction was carried out by simply intersecting the masks (Equation 7).

$$Mask_i = index_i < (or >) threshold$$

Equation 6. I-th Mask definition for the Pixel-Based approach.

$$Plastic\ Surfaces = \bigcap_{i=1}^4 Mask_i$$

Equation 7. Plastic Surface Extraction equation for the Pixel-Based approach.

where for each i-th normalized difference index (i.e. T_{bres} , $NDVI_{green}$, PSI , $NDSI$) the threshold is a value extracted from an investigated range of the i-th index values (see Table 2).

Index	T_{bres}	$NDVI_{green}$	PSI	$NDSI$
Inequality	Greater than	Less than	Greater than	Less than
Value range	[0.00; 0.29]	[-0.40; -0.11]	[-0.40; -0.11]	[0.00; 0.29]

Table 2. Ranges of the investigated thresholds for each proposed index implemented in the Pixel-Based approach.

The final extraction was considered as a binary classification of the examined scenes into the “plastic surfaces” class and the general “other” class. Lastly, the performance of the method was evaluated through the OA computed through the error matrix.

The classical accuracy assessment proposed after a classification is generally provided by means of a confusion matrix. The confusion matrix is a cross-tabulation matrix that compares reference and classified data (Congalton and Green, 2008). If reference data are available for all pixels (as occurred in section 1.6), then the confusion matrix provides a real information concerning the relationship between the reference and classified data otherwise, in all the other cases, the confusion matrix provides an estimate of the accuracy of the classification. Indeed, this is the most common occurrence because of time and financial constraints. In these occurrences, a sampling strategy is followed in order to collect reference data for the computation of the confusion matrix whereas an unbiased summary statistics would require the computation of a population matrix (Pontius Jr and Millones, 2011) or the statistical validation of the achieved results (Foody, 2004).

This PB approach was not focused, for computation time purposes, in the above validations (or unbiased estimations) since the evaluated confusion matrices were used only as a benchmark for the performed computations. The objective was the identification of the best confusion matrix. The i -th error matrix was evaluated using a similar number of ground reference for the two classes (more than 5000 pixels per class). References related to the “other” class were chosen within the most problematic areas: mixed classes and urban areas near the sampled pixels retrieved through the Cloud QA bands. The thresholds of each index were then evaluated by means of an IDL procedure (written ad hoc for this purpose) seeking the combinations of the four thresholds which maximize the OA: the appropriate thresholds were searched within ranges of the index values associated with the sampled pixels of plastic covered areas. *Table 2* shows the range of values investigated (810000 iterations) for each index and the inequality typology between the i -th index and its associated threshold.

For each combination of indices, the *Equation 6* and the *Equation 7* were applied, the related error matrix was evaluated and then the OA of the extraction computed. The values of the index thresholds corresponding to the highest OA achieved for each subset where, at the end, inserted in the *Equation 6* carrying out the final extraction by means of *Equation 7*.

1.5.3 Pixel-Based Approach: Results

The best results, representative of the extractions performed for each scene, are shown in Table 3 whereas Figure 5 and Figure 6 show the capability of the performed method and examples of misclassification errors respectively.

From the computations, the method performs well for plastic sheet placed above plastic net, generally bright in a true colour visualization.

The method revealed some commission errors within urban areas (*Figure 6*). These errors are a consequence of the use of the QA band for sampling purposes'.

Lastly, a manually drawn binary mask was used for a further countercheck of the maximum OA found (89%).

The binary mask covered built-up areas and by intersecting the extracted pixels with the mask it was possible to isolate and count commission pixels. The ratio between the number of commission pixels and the number of all extracted pixels showed that 11% of the extracted pixels are part of built-up areas. It is possible to conclude that the evaluated OA, in the IDL procedure, is a good estimate of the real achieved accuracy. Despite plastic nets can be very difficult to detect through Landsat data, due to their high transmittance, the proposed method also extracts plastic nets with dense mesh.

Id (scene)	T _{bres}	NDVI _{green}	PSI	NDSA	OA acc [%]
A	0.25	-0.21	-0.38	0.27	86
B	0.29	-0.21	-0.39	0.27	89
C	0.12	-0.18	-0.35	0.29	84
D	0.25	-0.11	-0.4	0.28	82

Table 3. Combination of the index thresholds with the highest OA achieved for the PB Method

This method was able to produce accuracy above 80% for the four scenes by using information gained from L8 QA band. However, this method required many iterations to obtain mean OA values below the ones achievable through OBIA. For these reasons, the subsequent sections will be focused on testing the OBIA approach.

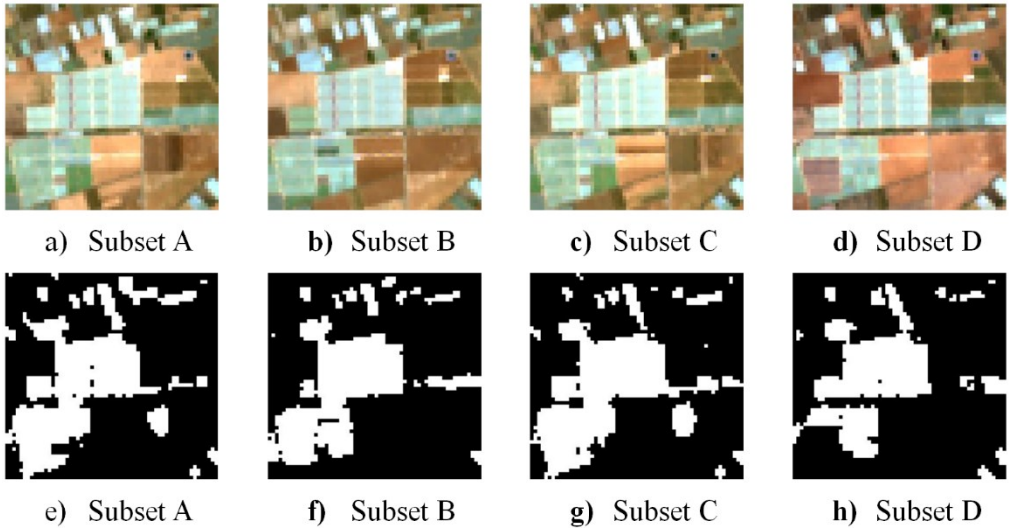


Figure 5. Pixel-Based method: Results for a small sample area related to the A, B, C, D subsets visualized in RGB to enhance the presence of plastic covers and in white to show the final detected areas.

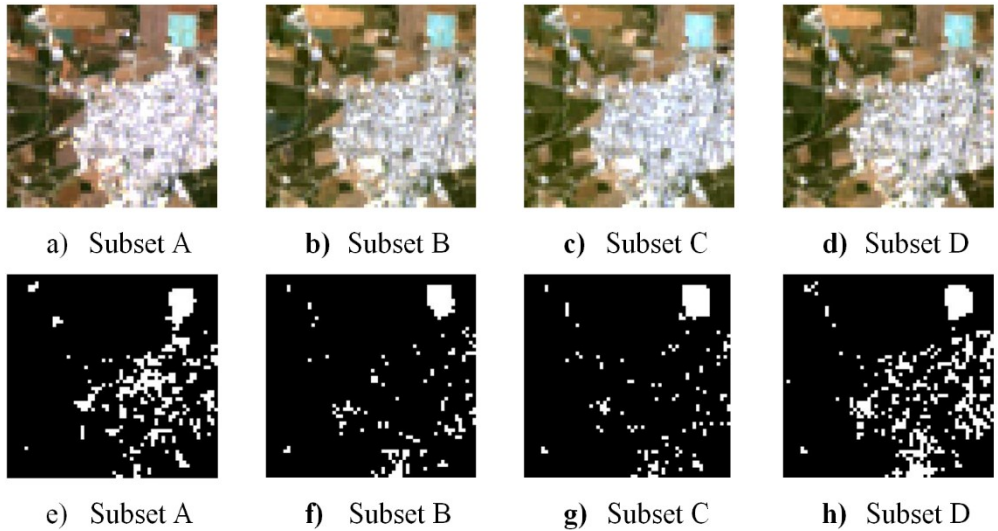


Figure 6. Pixel-Based method: Results for a small urban/rural sample area related to the A, B, C, D subsets visualized in RGB to enhance the presence of plastic covers and in white to show the final detected objects mixed with false positive areas.

1.6 OBIA approach: dataset

As stated in the introduction, the OBIA approach was characterized by the use of L8, S2 and WV2 data. In each scene, the study area was not affected by clouds presence. The WV2 scene was used to test differences, only due to the spectral informative content, between the S2 and the L8 PCG extractions.

For this study, a WV2 bundle images (PAN + MS, Panchromatic + Multi Spectral) in Ortho Ready Standard Level-2A (ORS2A) format was acquired. The image over the study area was taken on 5 July 2015 and presented a 0.5 m PAN GSD and 2.0 m MS GSD. All delivered products were ordered with a dynamic range of 11-bit and without the application of the dynamic range adjustment pre-processing. From the WV2 ORS2A bundle image, a pan-sharpened image with 0.5 m GSD was attained by means of the PANSHARP module included in Geomatica v. 2014 (PCI Geomatics, Richmond Hill, ON, Canada). The coordinates of seven ground control points (GCPs) and 32 independent check points (ICPs) obtained by differential global positioning system were used to perform the sensor orientation stage. The seven GCPs were used to compute the sensor model based on rational functions refined by a zero order transformation in the image space (RPC0). A medium resolution 10 m grid spacing DEM was used to carry out the orthorectification process. The DEM was characterized by a vertical accuracy of 1.34 m (root mean square error; RMSE) and was provided by the Andalusian Government. The planimetric accuracy (RMSE_{2D}) attained on the orthorectified pan-sharpened image was of around 0.5 m.

Moreover, from the MS data was produced an orthoimage of 2 m GSD and containing the full 8-band spectral information. The same seven GCPs, RPC0 model and DEM were used to attain the MS orthoimage. It is worth noting that atmospheric correction is especially important in those cases where multitemporal or multi-sensor images are analysed (Canty and Nielsen, 2008, Pacifici et al., 2014, Schroeder et al., 2006, Wulder et al., 2009). Thus, in this case and as a prior step to the orthorectification process, the original

WV2 MS image was atmospherically corrected by using the ATCOR (atmospheric correction) module included in Geomatica v. 2014. This absolute atmospheric correction algorithm involves the conversion of the original raw digital numbers to ground reflectance values, and it is based on the MODTRAN (MODerate resolution atmospheric TRANsmission) radiative transfer code (Berk et al., 1998). Particularly, in this chapter was used the atmospheric corrected WV2 MS orthoimage data only as reference for the L8 and S2 sensors data whereas the orthorectified pan-sharpened WV2 data was used only for co-registration purposes.

The L8 OLI scene (8 January 2016), Path 200 and Row 34, was downloaded at no cost from the USGS EROS website as Level 1 Terrain Corrected (L1T) product with 30m of geometric resolution (Roy et al., 2014b). The OLI PAN band and the TIRS bands were not used in the OBIA test. The extracted subset was atmospherically corrected by applying the ATCOR algorithm and co-registered with the WV2 pan-sharpened orthoimage through Geomatica v. 2014. It is important to note that a very accurate spatial matching is required to perform multi-sensor comparisons (Townshend et al., 1992, Zhang et al., 2014).

The S2 MSI image (12 January 2016, orbit R051) was downloaded at no cost from the Copernicus Scientific Data Hub website as a Level 1C product. S2 MSI L1C product is characterized by Top Of Atmosphere (TOA) reflectance values, cartographic projection, 12-bit dynamic range and tiles/granules consisting of 100 km² ortho-images in UTM/WGS84 projection. The Sen2Cor algorithm (Muller-Wilm et al., 2013) was used to obtain a Level 2A SE2 MSI product characterized by atmospherically corrected Bottom Of Atmosphere (BOA) reflectance values. Finally, the S2 study area was extracted from the selected granule and co-registered with the WV2 pan-sharpened orthoimage by using Geomatica v. 2014. In this study the 60m bands were not used since their contribution was considered negligible in an OBIA approach.

1.6.1 OBIA approach: segmentation stage

In this chapter, the MRS algorithm provided by eCognition v. 8.8 was used. MRS is a bottom-up region merging object algorithm starting with one-pixel objects (see Baatz and Schäpe (2000) and Tian and Chen (2007)) for a complete mathematical description). It takes into account each pixel as a separate object and subsequently pairs of image objects are merged to form bigger segments (Darwish et al., 2003). But this task is not easy, and it highly depends on the desired objects to be segmented (Tian and Chen, 2007). The outcome of the MRS algorithm requires user driven parameters. A tuning phase is required to obtain a satisfactory segmentation for the required objects (Tian and Chen, 2007). Indeed, the MRS algorithm output depends on three main factors or parameters: (i) the homogeneity criteria or scale parameter (SP) that determines the maximum allowed heterogeneity for the resulting segments, (ii) the weight of colour and shape criteria in the segmentation process (Shape), and (iii) the weight of the compactness and smoothness criteria (Compactness). The SP or heterogeneity criteria is the most influent since it controls the size of segments and thus the over-segmentation and under-segmentation error (Frauman and Wolff, 2005). Moreover, other input information such as the considered band combination (or band weight) has to be fixed into MRS algorithm.

Hundreds of segmentation test files were produced, for the three satellite data, by means of a looping algorithm created in eCognition (see section 1.7). It is worth noting that the initial pixel grid size of the corrected L8 image (30m GSD) was increased to 1.875 m by simply halving four times the original pixel size. The same procedure was applied to the corrected S2 image, being the 10 m and 20 m GSD bands split, without any resampling with subsequent interpolation, in 2m GSD bands. This was necessary to enhance the fit between the S2-L8 image segmentations and WV2 image segmentation. Lastly, using the chessboard segmentation algorithm included in eCognition v.8.8., the higher resolution WV2-based segmentation was applied to test the classification results attained from a common and accurately segmented dataset.

1.6.2 OBIA approach: Segmentation quality assessment

The selection of the best three MRS parameters (scale, shape and compactness) was carried out with a modified version of the supervised discrepancy measure named ED2 (Liu et al., 2012). As a supervised segmentation quality metric, the modified ED2 works with a set of reference objects used to evaluate the goodness of the segmentation. Moreover, it can be assessed through the capabilities of GIS software.

For this thesis 400 reference plastic covered greenhouse objects, manually delimited on the pan-sharpened WV2 orthoimage, were taken as reference objects. The 400 reference geometries were manually digitized considering only the plastic covered greenhouses common to the three satellite images. Although the ED2 can be evaluated in GIS software, in this thesis work the segmentation quality assessment computations were carried out thanks to a command line tool created for this purpose (AssesSeg.exe). The command line tool capabilities will be explained and shown in section 1.7.

ED2, in its original formulation, starts the computations with the definition of the corresponding segment dataset. For each considered image segmentation output the corresponding segment dataset owns the segments that spatially overlap the reference polygons. A further constraint is imposed over the corresponding segment dataset (Clinton et al., 2010): a considered segment can be labelled as a corresponding segment if the area of intersection between a reference polygon and the candidate segment is more than half the area of either the reference polygon or the candidate segment (overlapping criteria).

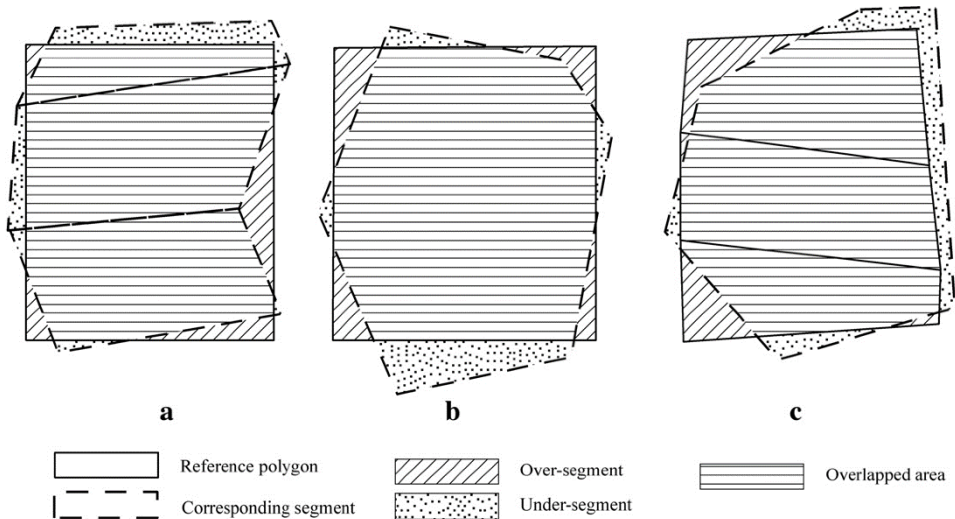


Figure 7. Discrepancies examples between reference polygon and corresponding segments: (a) one reference polygon vs. many corresponding segments; (b) one reference polygon vs. one corresponding segments; (c) many reference polygon vs. many corresponding segments. Source (Liu et al. (2012)).

According to Liu et al. (2012) the relationship between reference polygon and corresponding segments can be divided in three basic types (*Figure 7*):

- Overlapped area: the area shared between the reference polygon and the corresponding segment;
- Over-segmentation area (occurs in the case of less than optimal match): when a reference polygon is split by the boundary of a corresponding segment into at least two parts. The parts of the reference polygon that fall inside the area of the corresponding segment (which is the overlapped area) and the other parts that fall outside. The areas, of the reference polygon, that fall outside are called over-segments;
- Under-segmentation area (occurs in the case of less than optimal match): where the boundary of reference polygons splits a corresponding segment into at least two parts. The parts of the corresponding segment that fall inside the area of the reference polygon (overlapped area) and the other parts fall outside. The areas that fall outside are called under-segments and are the areas committed to the corresponding segment.

According to the overlapping criteria, over-segments and under-segments must be smaller than their associated overlapped areas.

After defining the corresponding segments dataset, the ED2 index (*Equation 8*) evaluates the segmentation quality in a two-dimensional Euclidean space by means of the Potential Segmentation Error (PSE) and the Number-of-Segments Ratio (NSR). The PSE (*Equation 9*) metric measures the geometric discrepancy as the ratio between the total area of under-segments and the total area of reference polygons (PSE = 0 means no under-segmentation). The NRS (*Equation 10*) measures the arithmetic discrepancy between the reference geometries and the candidate segments, being defined as the absolute difference between the number of reference polygons (m) and the number of corresponding segments (v) divided by the number of reference polygons. A NRS value of zero indicates

the optimal condition of a one to one correspondence between the reference and corresponding polygons.

$$ED2 = \sqrt{(PSE)^2 + (NSR)^2}$$

Equation 8. Euclidean Distance 2 Equation.

$$PSE = \frac{\sum |s_i - r_k|}{\sum |r_k|}$$

Equation 9. Potential Segmentation Error Equation.

$$NSR = \frac{|m - v|}{m}$$

Equation 10. Number-of-Segment Ratio Equation.

In which r_k is the k-th reference polygon and s_i is the i-th corresponding segment. A high ED2 value indicates a significant geometric discrepancy, otherwise a significant arithmetic discrepancy, or both.

The implemented modification of the ED2 index was introduced to consider the side effects of the overlapping criteria that act as a filter both on candidate corresponding segments and on reference geometries. When both the number of reference geometries and segmented polygons rise, there are often reference geometries without any corresponding segments. In those cases, the true number of employed reference geometries will be lower than the original one. Therefore, the ED2 index should take this into account to avoid bias when computing both PSE and NSR.

In this thesis, the overlapping criteria side effect was corrected by increasing both the PSE and NSR values when not all reference geometries are considered in the ED2 computations. Being n the number of excluded reference geometries, the new computed PSE (Equation 11) and NSR (Equation 12) will be:

$$PSE_{new} = \frac{\sum |s_i - r_k| + n \times \max(|s_i - r_k|)}{\sum |r_k|}$$

Equation 11. New Potential Segmentation Error Equation.

$$NSR_{new} = \frac{|m - v - n \times v_{max}|}{m - n}$$

Equation 12. New Number-of-Segment Ratio Equation

Where $\max(|s_i - r_k|)$ is the maximum under-segmented area found for a single reference geometry, v_{\max} represents the maximum number of corresponding segments found for one single reference geometry and $\sum |r_k|$ computes the total area of the $m - n$ reference geometries.

The best input segmentations were computed by using the MRS algorithm and the modified ED2 index firstly by varying only the SP value and fixing shape and compactness to 0.5. Then, when a local optimum SP was found, the research continued considering: SP values within an interval of the local optimum, shape values from 0.1 to 0.9 and compactness fixed to 0.5. For each calculation, SP and shape parameters were incremented in steps of 1.0 and 0.1 respectively (further details about the performed segmentation can be found in section 1.7).

1.6.3 OBIA approach: Training set and Features extraction

Three training sets of 60, 90 and 120 segments were created from the three best-estimated segmentations for L8, S2 and WV2. For each training set, one half of the geometries was related to the “Greenhouse” class and the other half to the class labelled as “Other”. Special attention was given to the selection of each single training segment. They were manually selected and considered as “pseudo-invariant” objects (similar geometry and same LC class) for the two classes and the three segmented satellite images. It is worth nothing that “pseudo-invariant” objects have to be considered different from Pseudo Invariant Features (PIF) that will be properly described in Chapter 2.

S2 and L8 comparisons were obtained from the following classification schemes: L8 with L8-based segmentation (L8_SEG_L8), L8 with WV2-based segmentation (L8_SEG_WV2), S2 with S2-based segmentation (S2_SEG_S2) and S2 with WV2-based segmentation (S2_SEG_WV2). Notice that the geometric information provided by the WV2 segmentation (i.e., common input segmentation) was used to test differences only due to S2 and L8 informative content (i.e. to test the presence of a difference only due to spectral

properties of the S2 MSI and L8 OLI sensor data). The comparisons were repeated for the three different training sets.

Features included in the classification process were computed at object level, compiling for each considered object a vector containing spectral information, texture data and spectral indices. Texture data were obtained from the Haralick Grey Level Co-occurrence Matrix (GLCM) (Haralick et al., 1973).

The best achieved segmentation, for each classification scheme, provided the geometric attributes for the classification input features computed by using eCognition v8.8. *Table 4* summarizes the content of each *i*-th vector composed by 126 features for the S2 image and 87 features in the case of the L8 image. The larger number of S2 object features was mainly due to the iteration of 20m red edge/NIR bands in the place of 10m S2 NIR band (i.e., was also tested the 20m red edge/NIR bands instead of the 10m NIR one to compute some indices in *Table 4*). This was made to test the enhanced spectral resolution of the novel S2 MSI sensor.

1.6.4 OBIA approach: Random Forest classifier design and classification accuracy assessment

In this chapter the RF classifier was used as a tool to perform comparisons between S2 MSI and L8 OLI scene in PCG detection. RF performed good classification results in several remote sensing studies demonstrating its robustness against a high number of variables (Breiman, 2001, Rodriguez-Galiano et al., 2012, Smith, 2010) proving to be relatively robust in spite of training size reduction and noise. A detailed review of the RF classifier algorithm is beyond the scope of this thesis work. More information about the mathematical formulation and its parameters can be found in the literature (e.g. Breiman (2001) and Dietterich (2000)).

Typology	Tested feat.	L8 No. of feat.	S2 No. of feat.	Description	Reference
----------	--------------	-----------------	-----------------	-------------	-----------

Spectral information	Mean and Standard deviation (SD)	16	20	Mean and SD of each band	(Definiens, 2009)
Indices	NDVI (Normalized Vegetation Index)	1	5	(NIR-R) / (NIR+R)	(Rouse Jr et al., 1974)
	GNDVI (Green NDVI)	1	5	(NIR-G) / (NIR+G)	(Gitelson et al., 2002)
	PMLI (Plastic-mulched land-cover index)	1	1	(SWIR1-R) / (SWIR1+R)	(Lu et al., 2014)
	SWIR1_NIR	1	5	(SWIR1-NIR) / (SWIR1+NIR)	(Aguilar et al., 2016c)
	SWIR2_NIR	1	5	(SWIR2-NIR) / (SWIR2+NIR)	(Aguilar et al., 2016c)
	SW1_SW2_NIR	1	5	(((SWIR1+SWIR2)/2)-NIR)/ (((SWIR1+SWIR2)/2)+NIR)	(Aguilar et al., 2016c)
	CIRRUS_NIR	1	-	(CIRRUS-NIR) / (CIRRUS+NIR)	(Aguilar et al., 2016c)
Texture	GLCM_h	8	10	GLCM homogeneity all directions	(Haralick et al., 1973)
	GLCM_d	8	10	GLCM dissimilarity all directions	(Haralick et al., 1973)
	GLCM_e	8	10	GLCM entropy all directions	(Haralick et al., 1973)
	GLCM_c	8	10	GLCM contrast all directions	(Haralick et al., 1973)
	GLCM_a	8	10	GLCM angular 2nd moment all directions	(Haralick et al., 1973)
	GLCM_cor	8	10	GLCM correlation all directions	(Haralick et al., 1973)
	GLCM_sd	8	10	GLCM standard deviation all directions	(Haralick et al., 1973)
	GLCM_m	8	10	GLCM mean all directions	(Haralick et al., 1973)

Table 4. Sentinel-2 (S2) and Landsat 8 (L8) object based features (feat.).

RF is an ensemble, supervised and non-parametric classifier in which a majority vote over several bootstrapped decision trees is carried out (Aguilar et al., 2016a). Particularly the dataset (training data) is sampled with replacement to form a training set. For this reason, a n records dataset is sampled n times. In this thesis around 2/3 of the available data were used to train the classifier and the remaining 1/3 as the test or validation dataset, which is also known as out-of-bag data (OOB). Furthermore, the algorithm can estimate

the importance of implemented features both for classification and non-parametric regressions by means of the Gini Index and OOB estimation (Rodriguez-Galiano et al., 2012). The Gini index measures also the impurity of a given element with respect the rest of the classes and was calculated as the sum of the products of all pairs of class proportions for classes present at the node. It reaches its maximum value when the class sizes at the node are equal whereas it is equal to zero if all cases in a node belong to the same class (Breiman et al., 1984).

The RF algorithm was applied by means of STATISTICA v10® (StatSoft Inc., Tulsa, OK, United States) and need two essential input to work: the number of classification tree and the number of predictor variables. The number of predictors affects both the correlations between the trees and the strength of the individual trees. A small number of predictors reduces correlation and strength and vice versa. Taking this into account, it is preferable to use a large number of trees and a small number of split variables to reduce the generalization error and the correlation between trees (Rodriguez-Galiano et al., 2012).

With regard to STATISTICA v10®, if the number of input trees is large enough, by default the software will determine the best final model as the one (i.e., as the specific number of trees) that yields the smallest error estimate for the testing sample.

In this thesis, a precautionary value of 500 trees (always above the best solution found by the software) was chosen and the number of random predictive variables was computed from the expression $p = \log_2(M + 1)$, being M the total number of predictor variables (features) (Hill and Lewicki, 2007).

Although the OOB accuracy is an unbiased estimator of the classification OA achieved at the classification stage, in this thesis a different accuracy assessment approach was used. Indeed, OOB accuracy estimation would be based on objects more than pixels and thus the error due to an erroneous segmentation would not be considered.

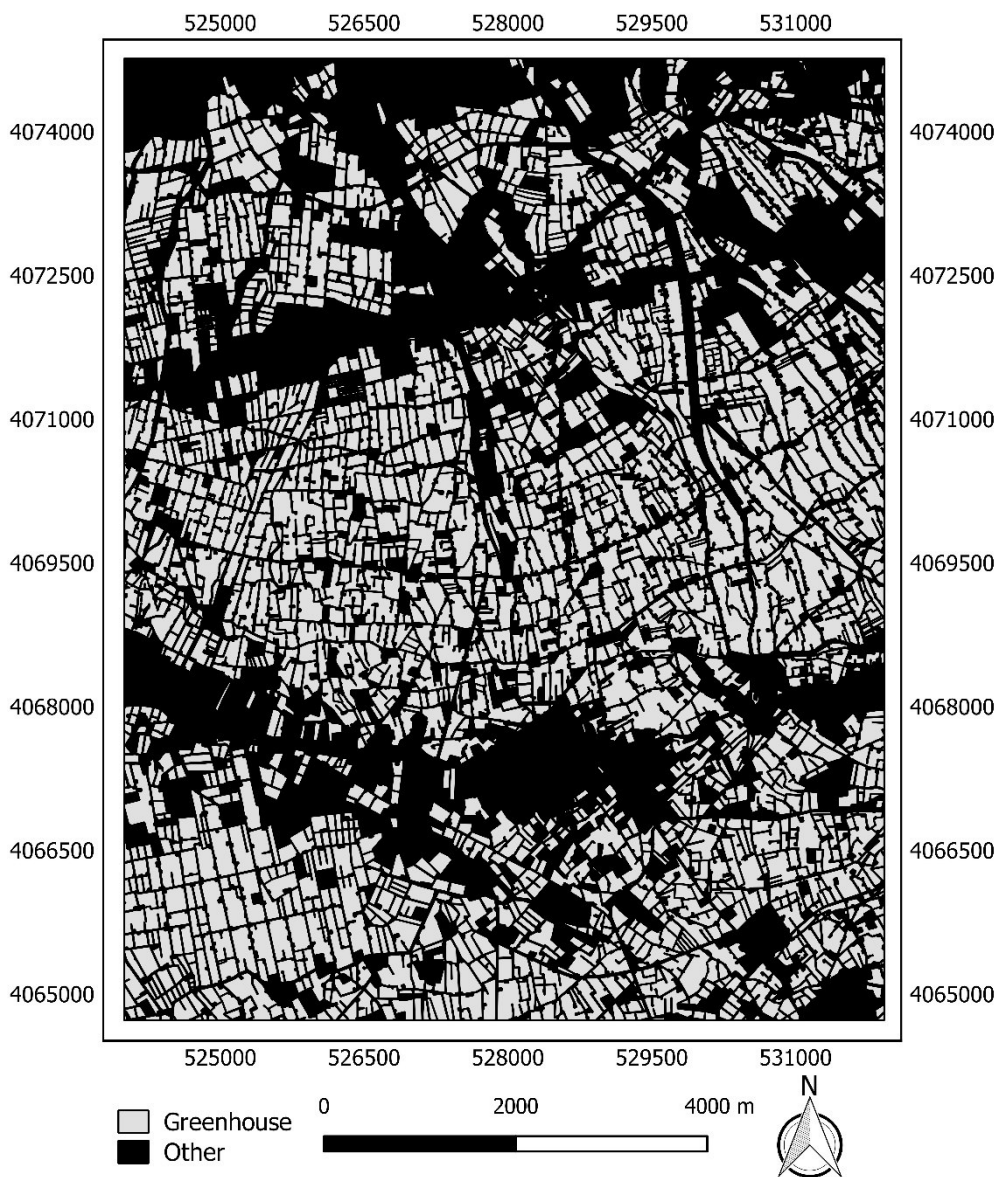


Figure 8. OBIA Approach: Manually digitized ground truth of the whole study area. Coordinate system: ETRS89 UTM Zone 30N.

In this way, and to provide a more reliable and complete accuracy indicator, pixel-based confusion matrices based on ground truths manually digitized were computed.

To obtain an unbiased and real accuracy estimator, the whole study area was manually digitized to provide ground truth data for confusion matrices computations (*Figure 8*).

Figure 8 shows the digitized ground truth of the whole study area thus divided in the “Greenhouse” and the general “Other” classes. Figure 8 was built up over the geometric base of the pan-sharpened WV2 orthoimage, considering the LC of the S2 and L8 images. Hence, the accuracy measures computed were user’s accuracy (UA), producer’s accuracy (PA), OA and kappa Index of Agreement (KIA) (Congalton, 1991).

1.6.5 OBIA approach: Segmentation procedure result

Several band combinations were tested for the three satellite data. The visible and near infrared bands turned out to be the most important regarding the final quality of the segmentations. Table 5 summarizes the characteristics of the best estimated segmentations performed over the three atmospherically and geometrically corrected images. During the computations, the compactness parameter was always fixed to 0.5 since in literature there are evidence of its negligible weight in the final output of the MRS algorithm (if compared to shape and, above all, SP parameter) (Drăguț et al., 2014, Liu and Xia, 2010). Finally, for the S2 data the 10 m GSD bands were considered the most valuable to produce a high quality segmentation results.

Satellite data	Band combination	No. objects	Scale	Shape	Compactness	Modified ED2
Landsat 8	Blue-Green-NIR	9596	43.0	0.3	0.5	0.424
Sentinel 2	Blue-Green-NIR	10561	39.0	0.2	0.5	0.319
WorldView2	Blue-Green-NIR2	10990	37.0	0.4	0.5	0.198

Table 5. OBIA Approach: Best estimate ED2 values and their associated input bands and Scale, Shape and Compactness parameters.

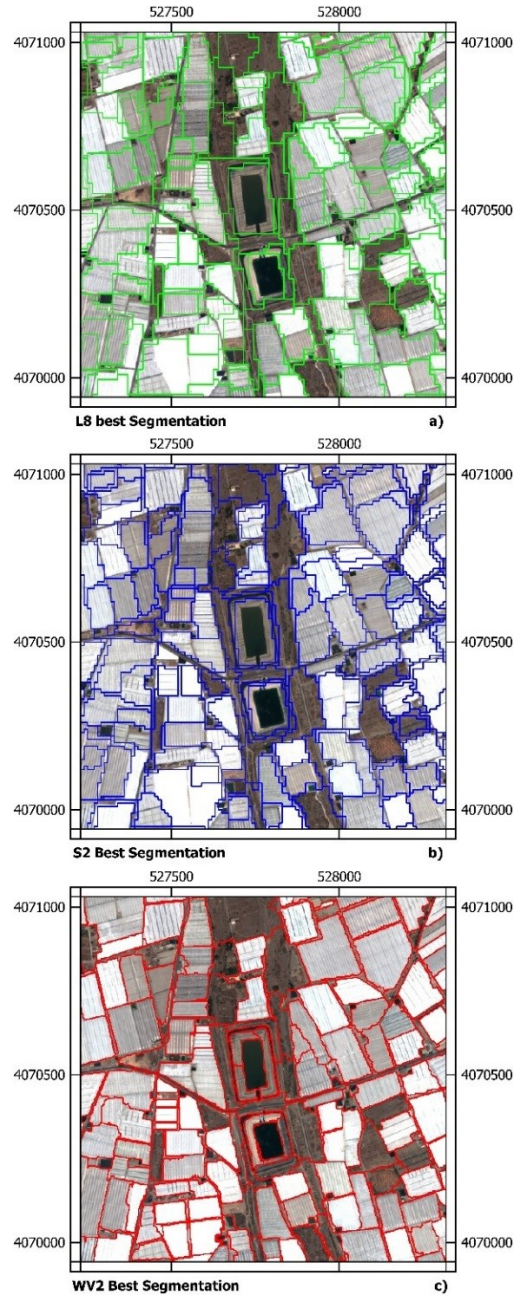


Figure 9. OBIA Approach: Visual comparison over the WV2 orthoimage (RGB visualization) of different best segmentations depending on the image data: a) best estimate L8-based segmentation; b) best estimate S2-based segmentation; c) best estimate WV2-based segmentation. Coordinate system: ETRS89 UTM Zone 30N.

Table 5 shows that the best greenhouse segmentation results in the case of L8 and S2 satellite images were obtained from using the same bands combination. Moreover, a very similar ED2 result (0.199) was calculated with the Blue-Green-NIR1 band combination for the WV2 data. This turned out to be a very important finding since it was proved the stability of the best bands combination to retrieve the best segmentation on greenhouses. It is important to highlight that this result was obtained from atmospherically corrected images and using the same 400 reference geometries. Figure 9 shows a comparison of the three selected best segmentation (L8, S2 and WV2) over the same area. Figure 9 depicts a very high visual quality for the selected WV2 segmentation based on PCG reference geometries. Figure 9 also shows that the segmentation based on L8 features performed the worst, while the S2-based segmentation still provided a good visual segmentation quality.

Lastly, this figure allows to appreciate the capability of the modified ED2 index to represent the segmentation quality of both VHR and medium resolution images (further details in section 1.7).

1.6.6 OBIA approach: Random Forest classifier results

The aim of the classification stage was to test differences in S2 and L8 PCG detection results. For this purpose, their spectral content was coupled both with their respective geometric information (i.e. best L8 and S2 based segmentations respectively) and with the more accurate WV2-based best segmentation. The four combinations (L8_SEG_L8, L8_SEG_WV2, S2_SEG_S2, S2_SEG_WV2) were applied to the three extracted training sets. For each classification, the input geometries for the training set were the ones corresponding to the chosen segmentation. Figure 10 shows a subset of the best classifications results (see Table 6) according to each one of the considered four combinations.

S2 classification featured a better visual quality than L8 classification for both S2 and WV2 based segmentations. In particular, S2 classification proved to be more adequate to discriminate narrow objects (as streets between greenhouses) than L8 classification by using both segmentation approaches.

This is certainly due to the enhanced GSD implemented with the MSI sensor. However, both S2 and L8 classifications show the presence of mixed pixels. This is a common drawback of medium resolution satellite imagery and occurs as a result of the heterogeneity of the landscape and the limitations imposed by the spatial resolution of the images. This fact was already reported by Wu et al. (2016) using an OBIA approach on a pan-sharpened Landsat 8 OLI image. In this regard, the reader should bear in mind the important difference between the best resolution for S2 (10m) and for L8 (30m). *Table 6* presents the achieved OA, KIA, PA UA for the two considered classes. It is worth nothing that these are real accuracies and not accuracy estimates since the whole study area was used as ground truth reference (*Figure 8*). The obtained OA values, ranging from 87.9% (L8_SEG_L8 with 60 training geometries) to 93.4% (S2_SEG_WV2 with 120 training geometries), can be considered satisfactory taking into account the minimum value of 85% proposed by Congalton and Green (2008).

Scene-Segments combination	training set	OA (%)	KIA	PA Green-house (%)	PA Other (%)	UA Green-house (%)	UA Other (%)
L8_SEG_L8	120	89.0	0.769	94.7	81.0	87.6	91.4
	90	89.1	0.773	93.1	83.4	88.8	89.6
	60	87.9	0.744	96.2	76.2	85.1	93.3
L8_SEG_WV2	120	89.8	0.791	90.6	88.8	92.0	86.9
	90	91.3	0.818	95.4	85.5	90.3	92.9
	60	90.8	0.806	95.1	84.8	89.9	92.5
S2_SEG_S2	120	90.9	0.864	95.1	84.8	89.9	92.5
	90	89.7	0.784	94.4	83.0	88.8	91.2
	60	89.8	0.786	94.9	82.4	88.5	92.0
S2_SEG_WV2	120	93.4	0.810	96.9	88.5	92.3	95.3
	90	92.6	0.844	97.0	86.2	90.9	95.3
	60	92.7	0.848	96.6	87.3	91.5	94.7

Table 6. OBIA Approach: Achieved OA, KIA, PA and OA for the considered classifications. These results should be understood as true accuracies, and not as estimated ones, since they were computed using a ground truth comprising the whole working area.

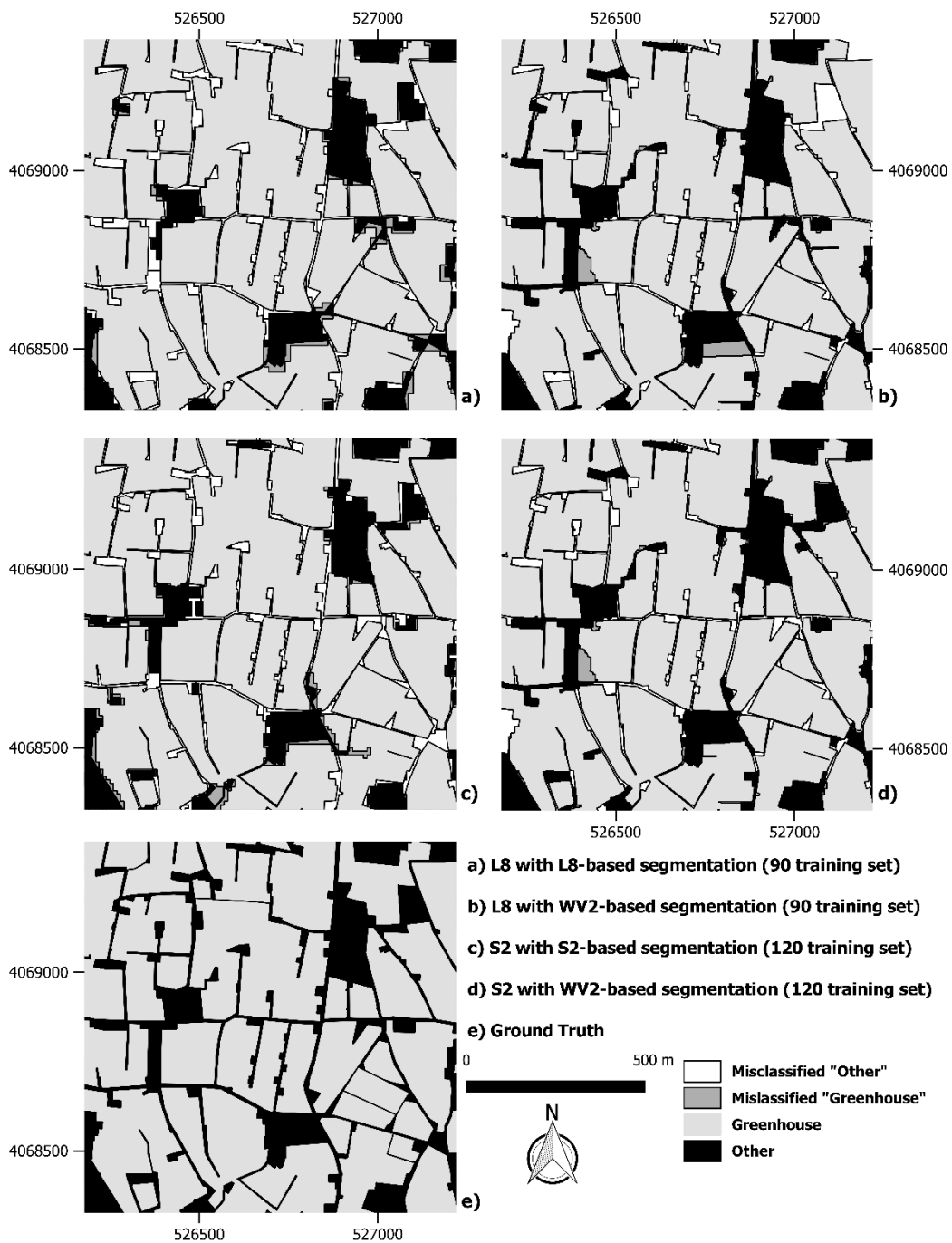


Figure 10. OBIA Approach: Comparisons of the best classification results for the four considered combinations. Coordinate system: ETRS89 UTM Zone 30N.

The obtained OA values, ranging from 87.9% (L8_SEG_L8 with 60 training geometries) to 93.4% (S2_SEG_WV2 with 120 training geometries), can be considered satisfactory taking into account the minimum value of 85% proposed by Congalton and Green (2008). Also KIA values showed a substantial and an almost perfect agreement (Landis and Koch, 1977). Both KIA and OA confirmed that S2 classifications performed always better than the corresponding L8 classifications. In particular, the difference in accuracy between S2 and L8 increased when the common WV2-based best segmentation was used. Since this result was achieved from the same segmentation, the attained differences can be attributed to the better performance of S2 features when undertaking the RF classification training process.

The PA reports about the number of pixels correctly classified in a particular category as a percentage of the total number of pixels belonging to that category in the image, being related to omission error. The PA for the “Greenhouse” class was always better than the PA of the “Other” class. These results confirmed the high classification quality achieved from the RF classifier for the “Greenhouse” class.

Moreover, the lower “Other” class PA accuracy can be explained considering its high heterogeneity. In fact, only one class was used to address all the spectral variability of the totality of LCs (i.e. water, vegetation, soil and build-up areas) different from the “Greenhouse” class. The UA is related to the probability that a pixel classified in a map actually represents that category on the ground. It is also related to commission error (error in field). UA values show that the reliability of the classification was very high for both classes, although the “Other” class featured slightly better UA values. Only in the case of the L8 with WV2-based segmentation (60 training segments), the UA of the “Greenhouse” class was greater than the corresponding UA for the “Other” class.

Although the training datasets were constituted of a very little number of geometries, the results were not very sensitive to the number of geometries. This was especially true with S2 data in which the best accuracies were always coupled with the 120 training geometries, whereas for the L8 data the best results were achieved from the training sets composed of 90 geometries.

Best L8_SEG_L8	Importance [%]	Best L8_SEG_WV2	Importance [%]
SWIR2_NIR	100	SWIR2_NIR	100
CIRR_NIR	76	SWIR1_NIR	97
SW1_SW2_NIR	63	SW1_SW2_NIR	81
SWIR1_NIR	53	PMLI	72
Mean green	46	Mean green	70
GLCM Mean costal	46	CIRR_NIR	65
GLCM Mean cirrus	45	GLCM Ang. 2nd moment green	60
GLCM Mean green	44	GLCM Entropy swir2	53
GLCM Dissimilarity cirrus	44	Mean blue	51
PMLI	43	GLCM Ang. 2nd moment blue	51

Table 7. OBIA Approach: Importance of the best ten features achieved for the best L8 classifications.

Best S2_SEG_S2	Importance [%]	Best S2_SEG_WV2	Importance [%]
SWIR1_NIR_10	100	SW1_SW2_NIR_B06	100
SWIR1_NIR_B08A	79	SWIR1_NIR_B08A	94
SWIR1_NIR_B05	74	PMLI	86
PMLI	71	SWIR1_NIR_B06	83
SW1_SW2_NIR_B06	67	SW1_SW2_NIR_10	81
SW1_SW2_NIR_B07	65	NDVI_G_B08A	78
SWIR2_NIR_B08A	63	SWIR1_NIR_B07	76
NDVI_G_B08A	62	Mean SWIR1	66
SWIR1_NIR_B06	59	Mean red	61
SWIR1_NIR_B07	51	GLCM Entropy SWIR1	56

Table 8. OBIA Approach: Importance of the best ten features achieved for the best S2 classifications.

RF classifier is also capable of estimating the importance of the features in the training process by means of the Gini index and the OOB estimation (Rodriguez-Galiano et al., 2012). *Table 7* and *Table 8* show that normalized features or ratios were always among the most important 10 features for both L8 and S2. However, the consistency of normalized features in S2 classifications was stronger if compared to L8 outputs. In fact, among the top ten L8 most significant features, it was frequent to find mean-value spectral features

and textural features. This result seems to point out a better S2 stability in order to efficiently extract plastic-covered greenhouses regardless atmospheric conditions.

1.7 OBIA approach: AssesSeg, a command line tool to assess the quality of segmentations

The results presented in this section are aimed at the enhancement of Object based Image Analysis (OBIA) products and will show how the results showed in *Table 5* were achieved.

In remote sensing OBIA applications, the segmentation stage is commonly part of the pre-processing phase. Scientific literature proposes different methods to assess the segmentation quality both from unsupervised and supervised approaches (e.g. Drăguț et al. (2014)). However, the proposed methods are not always coupled with tools able to automatically compute the described metrics. Because of this, researchers are forced to trial and error attempts (e.g. Tarantino and Figorito (2012)) or to perform computations by means of GIS software (e.g. Aguilar et al. (2016b)) for segmentation accuracy assessment. Although the above methods could be coupled with quite good results, their time cost is not negligible.

To overcome the limited availability of software dealing with assessing segmentation accuracy, in this section are showed the capabilities of a free of charge command line tool (AssesSeg.exe) that implements a modified version of the supervised discrepancy measure named Euclidean Distance 2 (ED2) proposed by Liu et al. (2012). The command line tool was created during this thesis work.

Particularly, AssesSeg was created to deal with a huge amount of segmentations carried out to detect the best band combinations (BCs) and MRS algorithm parameters for PCG detection from three multispectral satellite data used in the previous section (S2, L8 and WV2). The mathematics behind the tool is shown in section 1.6.2 and considers a set of reference objects (ROs), corresponding segment (CS) dataset and the overlapping criteria. *Figure 11* shows the procedure implemented for each geometry (that respect the overlapping criteria) within an output segmentation file.

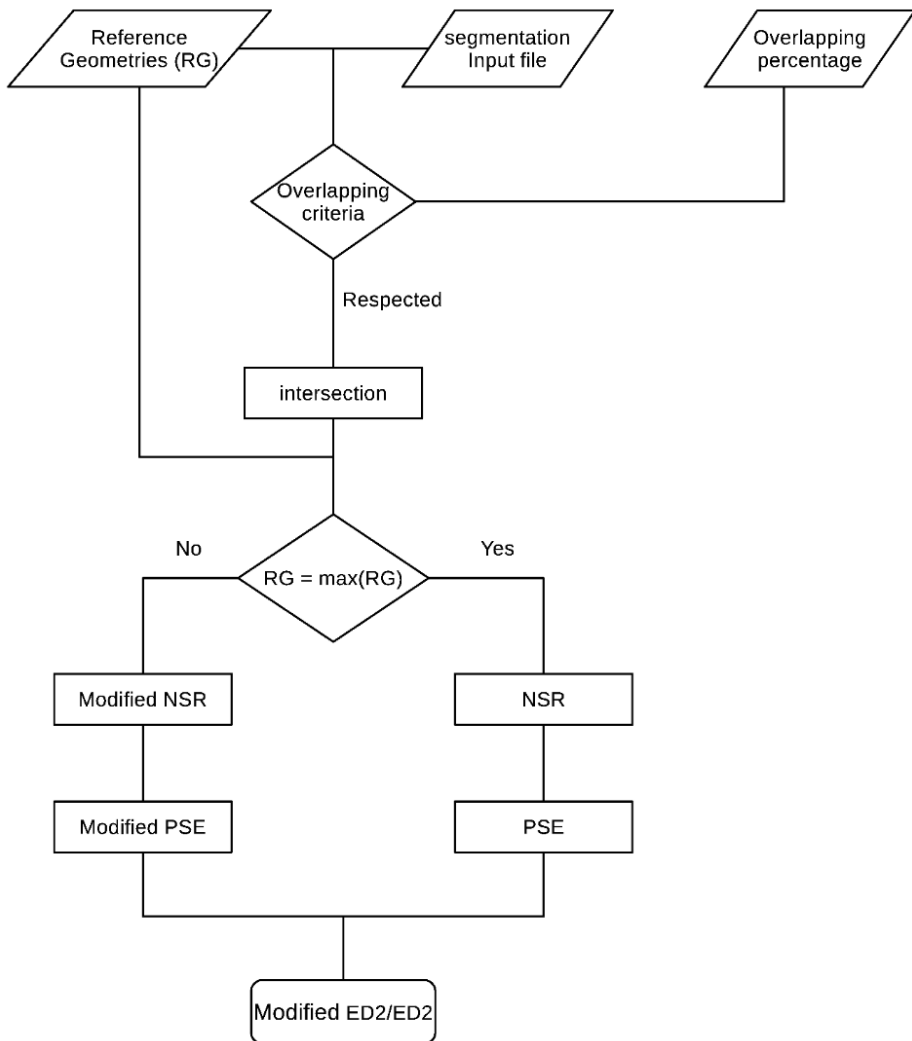
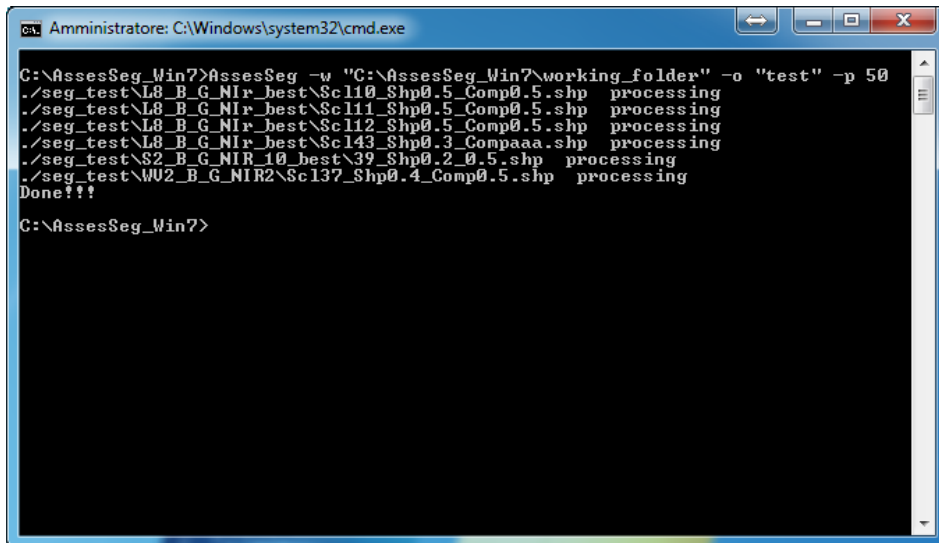


Figure 11. AssesSeg procedure implemented for each geometry (that respects the overlapping criteria) within an output segmentation file.

1.7.1 OBIA approach: AssesSeg

AssesSeg is a standalone command line tool as showed in Figure 12 (.exe extension downloadable at https://www.ual.es/Proyectos/GreenhouseSat/index_archivos/links.htm). It deals only with ESRI polygon shapefile (it does not depend on the segmentation software) and its source code was written in Python given the great availability of open source optimization, data analysis, control and numerical analysis libraries (e.g., NumPy, SciPy, etc.)(Riaño-Briceño et al., 2016). It requires two different typologies of input: a ROs shapefile and a set of output segmentation shapefiles (at least composed of one single file).

The output of AssSeg.exe is an Excel file (.xlsx) characterized by n spreadsheets, one for each folder containing a group of output segmentation files. Particularly the n-th spreadsheet will be named as the n-th considered folder, containing a group of output segmentation files, and will show the following columns (one for each single output segmenta-



```

C:\AssesSeg_Win7>AssesSeg -w "C:\AssesSeg_Win7\working_folder" -o "test" -p 50
./seg_test\L8_B_G_NIR_best\Sc110_Shp0.5_Comp0.5.shp processing
./seg_test\L8_B_G_NIR_best\Sc111_Shp0.5_Comp0.5.shp processing
./seg_test\L8_B_G_NIR_best\Sc112_Shp0.5_Comp0.5.shp processing
./seg_test\L8_B_G_NIR_best\Sc143_Shp0.3_Compaaa.shp processing
./seg_test\S2_B_G_NIR_10_best\39_Shp0.2_0.5.shp processing
./seg_test\WU2_B_G_NIR2_Sc137_Shp0.4_Comp0.5.shp processing
Done!!!
C:\AssesSeg_Win7>

```

Figure 12. AssesSeg command line output.

tion file):

- name: name of the i-th output segmentation shapefile in the n-th output segmentation folder;
- Scale, shape, compactness: if the i-th output segmentation shapefile comes from a MRS algorithm and has a specific name these three columns will record the input

scale, the shape and the compactness values of the i -th output shapefile. Particularly, AssesSeg recognize scale, shape and compactness If the shapefiles within the n -th folder are named ScIXX_ShpY.Y_CompZ.Z.shp or ScIXXX_ShpY.Y_CompZ.Z.shp. If the name of the selected output segmentation shapefile does not respect the required syntax rule then the scale, the shape and the compactness values will be set to 0.

- Number of ground truth geometries: number of selected ROs that respect the selection criteria (i.e. overlapping condition);
- Number of segmented geometries: number of selected output segmentation shapefile geometries that respect the selection criteria (e.g. overlapping condition);
- Area of ground truth geometries: total area of selected ground truth geometries expressed in square of the same unit of the internal reference system of the reference shapefile (if reference system is UTM the unit is expressed in meters).
- Under-segmented area (see Liu et al. (2012));
- NSR, PSE and ED2 or the new formulated ones as described in section 1.6.5.

AssesSeg can also deal with different prefixed overlapping percentages between ROs and input segments but this option was not explored in this thesis work.

Lastly, AssesSeg is a very powerful tool if coupled with automatic or semi-automatic algorithms able to produce many segmentation files following a certain criterion. In this thesis, this was accomplished by means of a semi-automatic procedure created through the eCognition commercial software and characterized by a looping process among prefixed MRS algorithm parameters (Figure 13).

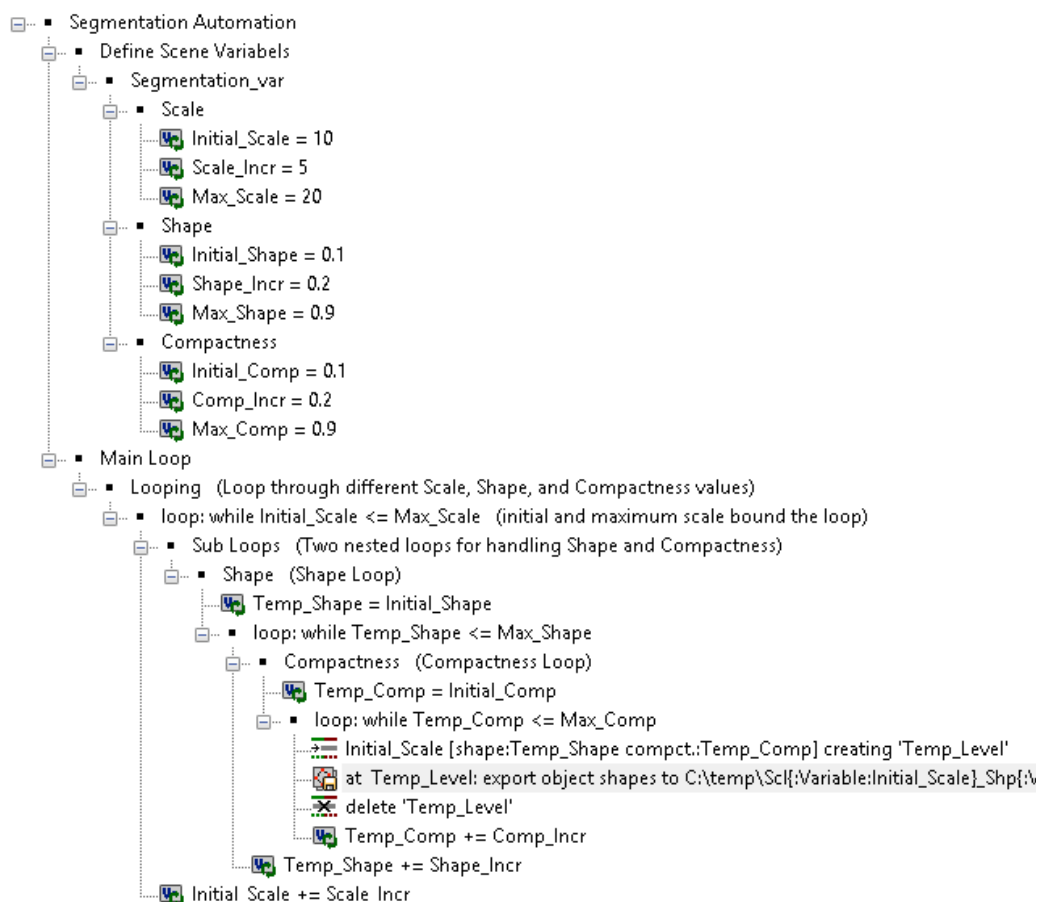


Figure 13. Looping process tree designed with eCognition in order to obtain input segmentation files for AssesSeg computations.

Figure 13 depicts the rule set implemented in eCognition. Particularly, the rule set:

- Accepts as input the initial and maximum scale, shape and compactness parameters and their increments;
- implements the above input parameters in nested loops:
- saves each produced segmentation file in a specific directory.

1.7.2 OBIA approach: AssesSeg output results

The MRS algorithm provided by eCognition v. 8.8 was used to produce the different segmentation datasets. As stated in the above sections, MRS requires user driven parameters (scale, shape, compactness and band weight) to obtain satisfactory results. Particularly, in this thesis work, the MRS band weight parameter was used to exclude specific bands from the computation. This was made to investigate the best BCs to PCG extractions.

For this purpose 400 reference PCG ROs (the same ROs for all three satellite images), manually delimited on the pan-sharpened WV2 PAN orthoimage (see section 1.6), were selected to find the best modified ED2 index for the three satellite data. To deal with SPs of the same order of magnitude among the three satellite data, the S2 and L8 initial geometric resolutions (10m and 20m GSD for S2, and 30m GSD for L8) were increased to 1.875 m and 2 m respectively by simply splitting pixels in equal parts without any resampling. Then AssesSeg was used for every modified ED2 index computation.

The test for S2 and L8 started by only varying the SP values (from 10 to 120 with a step of 1) and fixing shape and compactness to 0.5. In the case of S2 both the 10m GSD bands (Blue, Green, Red, NIR) and the 20m GSD bands were used. For the three satellite data, combinations including the SWIR bands were also tested in consideration of their high sensitivity to plastic coverings (Lu et al., 2015). However, for the S2 scene BCs involving 20 m GSD bands featured results characterized by higher ED2.

Table 9 depicts the best ED2 results achieved and the corresponding SP values for the tested L8 and S2 BCs. Note that the best S2 and L8 common BCs are Blue-Green-NIR and Blue-Green-Red-NIR. These BCs were subsequently applied to extend and refine the search of an optimal segmentation for S2 and L8 images by varying the SP values within an interval of the local optimum and the shape values from 0.1 to 0.9 (with a step of 0.1). The compactness parameter was always set to 0.5 since literature has evidenced its minor contribution as compared to shape and, above all, SP parameters (Drăguț et al., 2014).

Band combination	S2 ED2/SP	L8 ED2/SP
------------------	-----------	-----------

All bands	0.427/36	0.451/39
Blue-Green-NIR	0.406/37	0.448/43
Blue-Green-Red-NIR	0.373/36	0.438/40
Costal-Blue-SWIR1-SWIR2	---	0.512/39
Blue-Green-Red	0.413/41	---
Red-NIR	0.378/37	0.461/43
Red-NIR-SWIR1	---	0.465/40

Table 9. OBIA Approach: Modified ED2 and its associated scale parameter (shape and compactness were fixed to 0.5) for the tested Sentinel-2 (S2) and Landsat 8 (L8) equal-weighted band combinations. Computation executed with AssesSeg.exe

Table 10 summarizes the best achieved results for the two BCs and the two tested satellite images. It is worth noting that the S2 image always performed better segmentation, in terms of ED2 metric, than the L8 one.

The range of the tested SP values was reduced in the case of the WV2 image. In fact, the SP values ranged from 25 to 45 (Aguilar et al., 2016b), whereas the tested shape parameters varied from 0.1 to 0.9. The SP, shape parameter and compactness parameter followed the same rules defined for the S2 and L8 images. *Table 11* reports the best results achieved under the performed WV2 tests.

Band combination	S2 ED2/SP/shape	L8 ED2/SP/shape
Blue-Green-NIR	0.319/39/0.2	0.424/43/0.3
Blue-Green-Red-NIR	0.333/38/0.4	0.429/43/0.3

Table 10. OBIA Approach: Modified ED2 and its associated scale and shape parameters (compactness was fixed to 0.5) for the tested Sentinel-2 (S2) and Landsat 8 (L8) equal-weighted band combinations. In grey, the best results achieved. Computation executed with AssesSeg.exe

Table 10 and *Table 11* proved the stability of the resulting best band combinations for PCG segmentations regardless the tested satellite image. Indeed, all the best ED2 values are related to almost equal, and atmospherically corrected, band combinations.

Band combination	WV2 ED2/SP/shape
------------------	------------------

Blue-Green-NIR2	0.198/37/0.4
Blue-Green-NIR1	0.200/38/0.3
Blue-Green-NIR1-NIR2	0.216/42/0.2
Blue-Green-Red-NIR1-NIR2	0.221/38/0.2
Blue-Green-Red-NIR1	0.204/39/0.2
Blue-Green-Red-NIR2	0.203/38/0.3
Red-NIR2	0.231/39/0.2
Red-NIR1	0.238/40/0.3
Red-NIR1-NIR2	0.233/35/0.4
All	0.222/38/0.3

Table 11. OBIA Approach: Modified ED2 and its associated scale and shape parameters (compactness was fixed to 0.5) for the tested WorldView2 (WV2) equal-weighted band combinations. In grey, the best results achieved. Computation executed with AssesSeg.exe

As shown in *Figure 9* (section 1.6.5), the segmentation features a high visual quality for the WV2 image and an acceptable visual quality for S2 image, with L8 segmentation performing the worst. This visual comparison allows readers to fully appreciate the capability of the modified ED2 index and AssesSeg software to extract the best potential segmentation from both VHR and medium resolution satellite images.

Finally, 50 independent sets of ROs were randomly extracted (with replacement) from the initial population of 400 ROs in groups of variable sample size ranging from 25 up to 200 ROs with a step of five (see *Figure 14*).

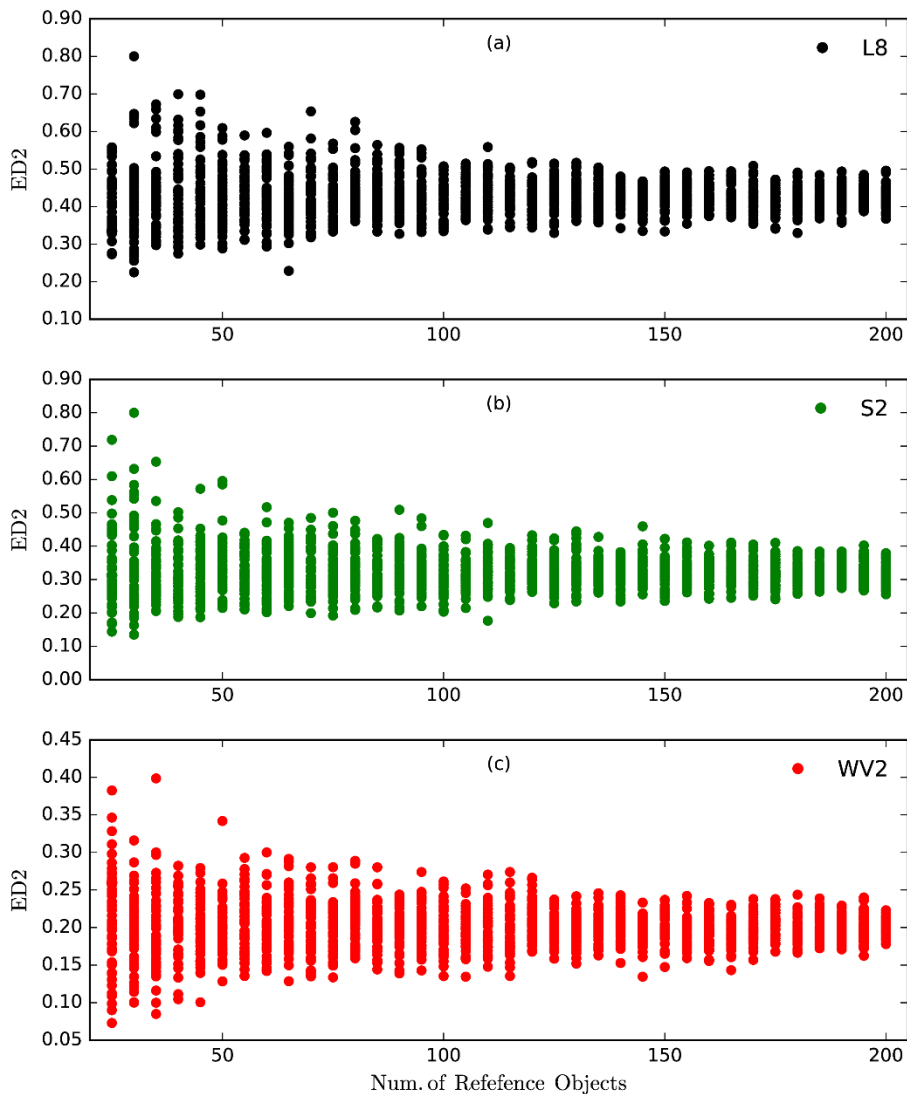


Figure 14. OBIA Approach: Scatter plots ED2- Number of Reference Objects. Computation executed with AssesSeg.exe.

Each single independent set was extracted without replacement. Particularly the extractions were performed by means of a Python script implementing the ogr library capabilities.

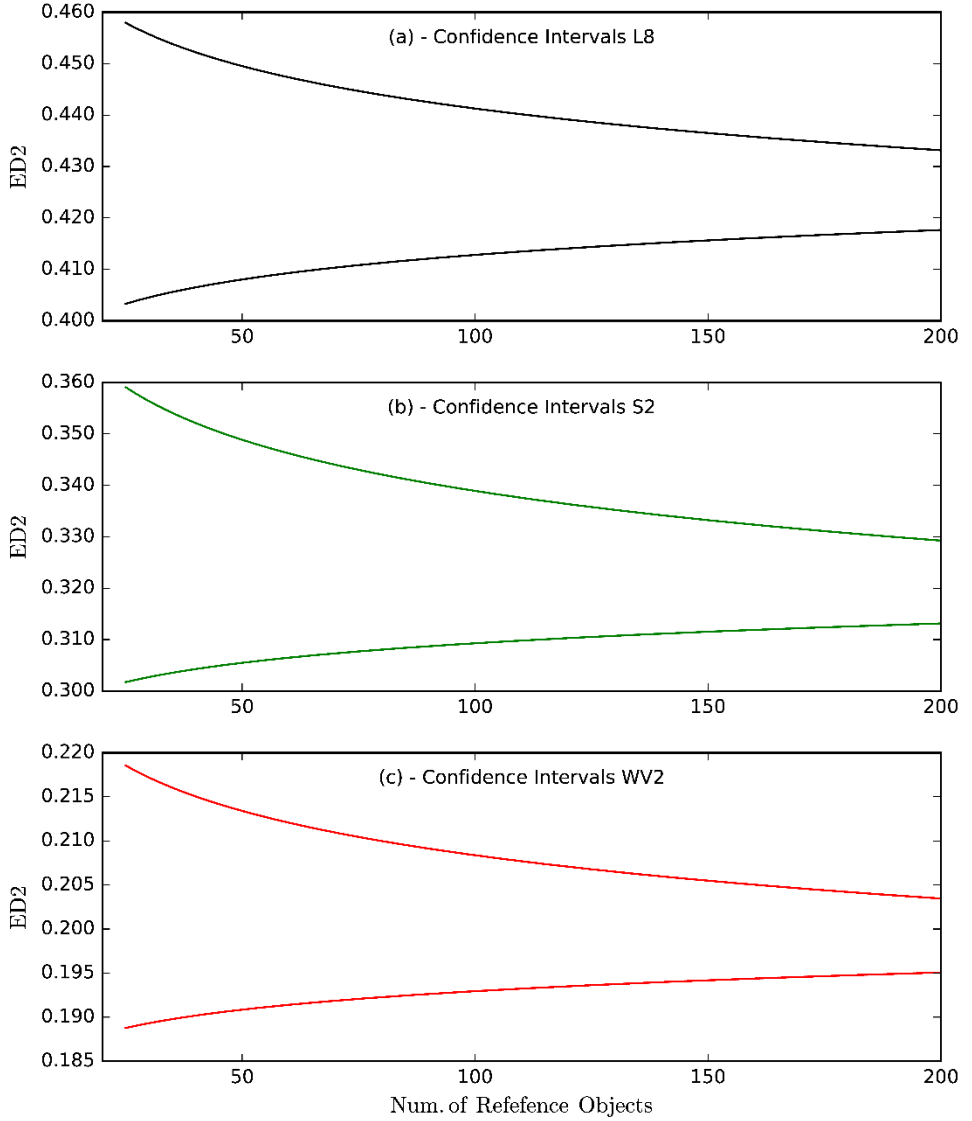


Figure 15. OBIA Approach: 95 % Confidence intervals computed from the scatterplots depicted in Figure 14.

This experiment highlighted the clear relationship between the uncertainty linked to the computation of the modified ED2 index and the number of ROs employed. *Figure 14* and *Figure 15* respectively show the scatter plots and the corresponding 95% confidence intervals (CIs) for the modified ED2 index according to the number of ROs sample size.

In this sense, both figures demonstrate that the uncertainty in computing the modified ED2 index turns out to be excessively high when working with a low number of ROs. In fact, based on the results obtained in this work, a good segmentation would require more than 100 ROs. It is relevant to underline that only around 30 ROs per class were used in previous segmentation quality studies (Witharana and Civco, 2014, Liu et al., 2012). In particular, a higher number of ROs are not a problem for AssesSeg.

ACKNOWLEDGEMENTS Chapter 1

For the use of the WorldView-2 scene, the use of the software eCognition V 8.8, the use of the software Statistica and for the precious suggestions the Ph.D. candidate is thankful to the UAL (Universidad de Almeria) research group: Prof. M.A. Aguilar, Prof. F.J. Aguilar and Doc. Abderrahim Nemmaoui. The Ph.D. candidate is also thankful to Prof. E. Tarantino for her suggestions. Part of the data used in this chapter was funded by the Spanish Ministry of Economy and Competitiveness (Spain) and the European Union FEDER funds (Grant Reference AGL2014-56017-R). It takes part of the general research line promoted by the Agrifood Campus of International Excellence ceiA3 (<http://www.ceia3.es/>).

REFERENCES of Chapter 1

- AGÜERA, F., AGUILAR, F. J. & AGUILAR, M. A. 2008. Using texture analysis to improve per-pixel classification of very high resolution images for mapping plastic greenhouses. *ISPRS Journal of Photogrammetry and Remote Sensing*, 63, 635-646.
- AGÜERA, F., AGUILAR, M. & AGUILAR, F. 2006. Detecting greenhouse changes from QB imagery on the Mediterranean Coast. *Int. J. Remote Sens*, 27, 47514767.
- AGÜERA, F. & LIU, J. 2009. Automatic greenhouse delineation from QuickBird and Ikonos satellite images. *Computers and Electronics in Agriculture*, 66, 191-200.
- AGUILAR, F. J., NEMMAOUI, A., AGUILAR, M. A., CHOURAK, M., ZARHLOULE, Y. & GARCÍA LORCA, A. M. 2016a. A Quantitative Assessment of Forest Cover Change in the Moulouya River Watershed (Morocco) by the Integration of a Subpixel-Based and Object-Based Analysis of Landsat Data. *Forests*, 7, 23.
- AGUILAR, M., AGUILAR, F., GARCÍA LORCA, A., GUIRADO, E., BETLEJ, M., CICHON, P., NEMMAOUI, A., VALLARIO, A. & PARENTE, C. 2016b. Assessment of Multiresolution Segmentation for Extracting Greenhouses from WORLDVIEW-2 Imagery. *ISPRS-International Archives of the Photogrammetry, Remote Sensing and Spatial Information Sciences*, 145-152.
- AGUILAR, M., BIANCONI, F., AGUILAR, F. & FERNÁNDEZ, I. 2014. Object-Based Greenhouse Classification from GeoEye-1 and WorldView-2 Stereo Imagery. *Remote Sensing*, 6, 3554.
- AGUILAR, M., NEMMAOUI, A., NOVELLI, A., AGUILAR, F. & GARCÍA LORCA, A. 2016c. Object-Based Greenhouse Mapping Using Very High Resolution Satellite Data and Landsat 8 Time Series. *Remote Sensing*, 8, 513.
- AGUILAR, M. A., VALLARIO, A., AGUILAR, F. J., LORCA, A. G. & PARENTE, C. 2015. Object-Based greenhouse horticultural crop identification from multi-temporal satellite imagery: A case study in Almeria, Spain. *Remote Sensing*, 7, 7378-7401.
- ARCIDIACONO, C. & PORTO, S. Image processing for the classification of crop shelters. International Symposium on High Technology for Greenhouse System Management: Greensys2007 801, 2007. 309-316.
- ARCIDIACONO, C. & PORTO, S. Pixel-based classification of high-resolution satellite images for crop-shelter coverage recognition. XXVIII International Horticultural

- Congress on Science and Horticulture for People (IHC2010): International Symposium on 937, 2010. 1003-1010.
- ARCIDIACONO, C. & PORTO, S. M. 2012. Improving per-pixel classification of crop-shelter coverage by texture analyses of high-resolution satellite panchromatic images. *Journal of Agricultural Engineering*, 42, 9-16.
- BAATZ, M. & SCHÄPE, A. 2000. Multiresolution segmentation: an optimization approach for high quality multi-scale image segmentation. Herbert Wichmann Verlag: Berlin, Germany.
- BAI, Y., WONG, M. S., SHI, W.-Z., WU, L.-X. & QIN, K. 2015. Advancing of land surface temperature retrieval using extreme learning machine and spatio-temporal adaptive data fusion algorithm. *Remote Sensing*, 7, 4424-4441.
- BERK, A., BERNSTEIN, L., ANDERSON, G., ACHARYA, P., ROBERTSON, D., CHETWYND, J. & ADLER-GOLDEN, S. 1998. MODTRAN cloud and multiple scattering upgrades with application to AVIRIS. *Remote Sensing of Environment*, 65, 367-375.
- BLASCHKE, T. 2010. Object based image analysis for remote sensing. *ISPRS journal of photogrammetry and remote sensing*, 65, 2-16.
- BLASCHKE, T., HAY, G. J., KELLY, M., LANG, S., HOFMANN, P., ADDINK, E., QUEIROZ FEITOSA, R., VAN DER MEER, F., VAN DER WERFF, H., VAN COILLIE, F. & TIEDE, D. 2014. Geographic Object-Based Image Analysis – Towards a new paradigm. *ISPRS Journal of Photogrammetry and Remote Sensing*, 87, 180-191.
- BREIMAN, L. 2001. Random forests. *Machine learning*, 45, 5-32.
- BREIMAN, L., FRIEDMAN, J., STONE, C. J. & OLSHEN, R. A. 1984. *Classification and regression trees*, CRC press.
- BRIASSOULIS, D., BABOU, E., HISKAKIS, M., SCARASCIA, G., PICUNO, P., GUARDE, D. & DEJEAN, C. 2013. Review, mapping and analysis of the agricultural plastic waste generation and consolidation in Europe. *Waste Management & Research*, 31, 1262-1278.
- CANTY, M. J. & NIELSEN, A. A. 2008. Automatic radiometric normalization of multitemporal satellite imagery with the iteratively re-weighted MAD transformation. *Remote Sensing of Environment*, 112, 1025-1036.
- CAPOBIANCO, R. & PICUNO, P. Remote sensing and thematic mapping of protected cultivation in Southern Italy agricultural landscapes. Agricultural and biosystems engineering for a sustainable world. International Conference on Agricultural Engineering, Hersonissos, Crete, Greece, 23-25 June, 2008, 2008. European Society of Agricultural Engineers (AgEng), OP-1160.
- CARVAJAL, F., AGÜERA, F., AGUILAR, F. & AGUILAR, M. 2010. Relationship between atmospheric corrections and training-site strategy with respect to accuracy of greenhouse detection process from very high resolution imagery. *International Journal of Remote Sensing*, 31, 2977-2994.

- CARVAJAL, F., CRISANTO, E., AGUILAR, F., AGUERA, F. & AGUILAR, M. Greenhouses detection using an artificial neural network with a very high resolution satellite image. ISPRS Technical Commission II Symposium, Vienna, 2006. 37-42.
- CLINTON, N., HOLT, A., SCARBOROUGH, J., YAN, L. & GONG, P. 2010. Accuracy assessment measures for object-based image segmentation goodness. *Photogrammetric Engineering and remote sensing*, 76, 289-299.
- COLBY, J. D. & KEATING, P. 1998. Land cover classification using Landsat TM imagery in the tropical highlands: the influence of anisotropic reflectance. *International Journal of Remote Sensing*, 19, 1479-1500.
- CONGALTON, R. G. 1991. A review of assessing the accuracy of classifications of remotely sensed data. *Remote sensing of environment*, 37, 35-46.
- CONGALTON, R. G. & GREEN, K. 2008. *Assessing the accuracy of remotely sensed data: principles and practices*, CRC press.
- CROCETTO, N. & TARANTINO, E. 2009. A class-oriented strategy for features extraction from multirate ASTER imagery. *Remote Sensing*, 1, 1171-1189.
- DARWISH, A., LEUKERT, K. & REINHARDT, W. Image segmentation for the purpose of object-based classification. International Geoscience and Remote Sensing Symposium, 2003. III: 2039-2041.
- DEFINIENS, A. 2009. Definiens eCognition Developer 8 Reference Book. *Definiens AG, München*.
- DRÄGUJ, L., CSILLIK, O., EISANK, C. & TIEDE, D. 2014. Automated parameterisation for multi-scale image segmentation on multiple layers. *ISPRS Journal of Photogrammetry and Remote Sensing*, 88, 119-127.
- DU, Y., ZHANG, Y., LING, F., WANG, Q., LI, W. & LI, X. 2016. Water Bodies' Mapping from Sentinel-2 Imagery with Modified Normalized Difference Water Index at 10-m Spatial Resolution Produced by Sharpening the SWIR Band. *Remote Sensing*, 8, 354.
- ESPI, E., SALMERON, A., FONTECHA, A., GARCÍA, Y. & REAL, A. 2006. Plastic films for agricultural applications. *Journal of Plastic Film and Sheeting*, 22, 85-102.
- FERNÁNDEZ-MANSO, A., FERNÁNDEZ-MANSO, O. & QUINTANO, C. 2016. SENTINEL-2A red-edge spectral indices suitability for discriminating burn severity. *International Journal of Applied Earth Observation and Geoinformation*, 50, 170-175.
- FOODY, G. M. 2004. Thematic map comparison. *Photogrammetric Engineering & Remote Sensing*, 70, 627-633.
- FRAUMAN, E. & WOLFF, E. Segmentation of very high spatial resolution satellite images in urban areas for segments-based classification. Proceedings for 3rd International Symposium Remote Sensing and Data Fusion Over Urban Areas. Tempe, Arizona, 2005.

- GITELSON, A. A., KAUFMAN, Y. J., STARK, R. & RUNDQUIST, D. 2002. Novel algorithms for remote estimation of vegetation fraction. *Remote sensing of Environment*, 80, 76-87.
- HARALICK, R. M., SHANMUGAM, K. & DINSTEN, I. H. 1973. Textural features for image classification. *Systems, Man and Cybernetics, IEEE Transactions on*, 610-621.
- HASITUYA, CHEN, Z., WANG, L., WU, W., JIANG, Z. & LI, H. 2016. Monitoring Plastic-Mulched Farmland by Landsat-8 OLI Imagery Using Spectral and Textural Features. *Remote Sensing*, 8, 353.
- HILL, T. & LEWICKI, P. 2007. STATISTICS Methods and Applications. StatSoft, Tulsa, USA.
- IMMITZER, M., VUOLO, F. & ATZBERGER, C. 2016. First experience with sentinel-2 data for crop and tree species classifications in Central Europe. *Remote Sensing*, 8, 166.
- KOC-SAN, D. 2013. Evaluation of different classification techniques for the detection of glass and plastic greenhouses from WorldView-2 satellite imagery. *Journal of Applied Remote Sensing*, 7, 073553-073553.
- LAMONT, W. J. 1996. What are the components of a plasticulture vegetable system? *HortTechnology*, 6, 150-154.
- LANDIS, J. R. & KOCH, G. G. 1977. The measurement of observer agreement for categorical data. *biometrics*, 159-174.
- LEVIN, N., LUGASSI, R., RAMON, U., BRAUN, O. & BEN-DOR, E. 2007. Remote sensing as a tool for monitoring plasticulture in agricultural landscapes. *International Journal of Remote Sensing*, 28, 183-202.
- LIU, D. & XIA, F. 2010. Assessing object-based classification: advantages and limitations. *Remote Sensing Letters*, 1, 187-194.
- LIU, Y., BIAN, L., MENG, Y., WANG, H., ZHANG, S., YANG, Y., SHAO, X. & WANG, B. 2012. Discrepancy measures for selecting optimal combination of parameter values in object-based image analysis. *ISPRS Journal of Photogrammetry and Remote Sensing*, 68, 144-156.
- LU, L., DI, L. & YE, Y. 2014. A Decision-tree classifier for extracting transparent plastic-mulched landcover from Landsat-5 TM images. *Selected Topics in Applied Earth Observations and Remote Sensing, IEEE Journal of*, 7, 4548-4558.
- LU, L., HANG, D. & DI, L. 2015. Threshold model for detecting transparent plastic-mulched landcover using moderate-resolution imaging spectroradiometer time series data: a case study in southern Xinjiang, China. *Journal of Applied Remote Sensing*, 9, 097094-097094.
- MESEV, V., GORTE, B. & LONGLEY, P. A. 2000. Modified maximum-likelihood classification algorithms and their application to urban remote sensing. *Remote Sensing and Urban Analysis; Donnay, J.-P., Barnsley, MJ, Longley, PA, Eds*, 62-83.

- MONTANARO, M., GERACE, A., LUNSFORD, A. & REUTER, D. 2014. Stray light artifacts in imagery from the Landsat 8 Thermal Infrared Sensor. *Remote Sensing*, 6, 10435-10456.
- MULLER-WILM, U., LOUIS, J., RICHTER, R., GASCON, F. & NIEZETTE, M. Sentinel-2 Level 2A Prototype Processor: Architecture, Algorithms And First Results. ESA Special Publication, 2013. 98.
- NOVELLI, A., AGUILAR, M. A., NEMMAOUI, A., AGUILAR, F. J. & TARANTINO, E. 2016. Performance evaluation of object based greenhouse detection from Sentinel-2 MSI and Landsat 8 OLI data: A case study from Almeria (Spain). *International Journal of Applied Earth Observation and Geoinformation*, 52, 403-411.
- NOVELLI, A. & TARANTINO, E. 2015a. Combining ad hoc spectral indices based on LANDSAT-8 OLI/TIRS sensor data for the detection of plastic cover vineyard. *Remote Sensing Letters*, 6, 933-941.
- NOVELLI, A. & TARANTINO, E. The contribution of Landsat 8 TIRS sensor data to the identification of plastic covered vineyards. Third International Conference on Remote Sensing and Geoinformation of the Environment, 2015b. International Society for Optics and Photonics, 95351E-95351E-9.
- PACIFICI, F., LONGBOTHAM, N. & EMERY, W. J. 2014. The Importance of physical quantities for the analysis of multitemporal and multiangular optical very high spatial resolution images. *IEEE Transactions on Geoscience and Remote Sensing*, 52, 6241-6256.
- PALA, E., TASDEMIR, K. & KOC-SAN, D. Unsupervised extraction of greenhouses using approximate spectral clustering ensemble. Geoscience and Remote Sensing Symposium (IGARSS), 2015 IEEE International, 2015. IEEE, 4668-4671.
- PESARESI, M., CORBANE, C., JULEA, A., FLORCZYK, A. J., SYRRIS, V. & SOILLE, P. 2016. Assessment of the Added-Value of Sentinel-2 for Detecting Built-up Areas. *Remote Sensing*, 8, 299.
- PICUNO, P., TORTORA, A. & CAPOBIANCO, R. L. 2011. Analysis of plasticulture landscapes in Southern Italy through remote sensing and solid modelling techniques. *Landscape and urban planning*, 100, 45-56.
- PONTIUS JR, R. G. & MILLONES, M. 2011. Death to Kappa: birth of quantity disagreement and allocation disagreement for accuracy assessment. *International Journal of Remote Sensing*, 32, 4407-4429.
- REDDY, M. A. 2008. *Textbook of remote sensing and geographical information systems*, BS publications Hyderabad.
- RIAÑO-BRICEÑO, G., BARREIRO-GOMEZ, J., RAMIREZ-JAIME, A., QUIJANO, N. & OCAMPO-MARTINEZ, C. 2016. MatSWMM—An open-source toolbox for designing real-time control of urban drainage systems. *Environmental Modelling & Software*, 83, 143-154.

- RIVERO, R., GRUNWALD, S., BINFORD, M. & OSBORNE, T. 2009. Integrating spectral indices into prediction models of soil phosphorus in a subtropical wetland. *Remote Sensing of Environment*, 113, 2389-2402.
- RODRIGUEZ-GALIANO, V. F., GHIMIRE, B., ROGAN, J., CHICA-OLMO, M. & RIGOL-SANCHEZ, J. P. 2012. An assessment of the effectiveness of a random forest classifier for land-cover classification. *ISPRS Journal of Photogrammetry and Remote Sensing*, 67, 93-104.
- ROUSE JR, J. W., HAAS, R., SCHELL, J. & DEERING, D. 1974. Monitoring vegetation systems in the Great Plains with ERTS. *NASA special publication*, 351, 309.
- ROY, D. P., BORAK, J. S., DEVADIGA, S., WOLFE, R. E., ZHENG, M. & DESCLOITRES, J. 2002. The MODIS land product quality assessment approach. *Remote Sensing of Environment*, 83, 62-76.
- ROY, D. P., WULDER, M., LOVELAND, T., WOODCOCK, C., ALLEN, R., ANDERSON, M., HELDER, D., IRONS, J., JOHNSON, D. & KENNEDY, R. 2014. Landsat-8: Science and product vision for terrestrial global change research. *Remote Sensing of Environment*, 145, 154-172.
- SCHROEDER, T. A., COHEN, W. B., SONG, C., CANTY, M. J. & YANG, Z. 2006. Radiometric correction of multi-temporal Landsat data for characterization of early successional forest patterns in western Oregon. *Remote sensing of environment*, 103, 16-26.
- SÖNMEZ, N. K. & SARI, M. 2006. Use of remote sensing and geographic information system technologies for developing greenhouse databases. *Turkish journal of agriculture and forestry*, 30, 413-420.
- TARANTINO, E. 2012. Monitoring spatial and temporal distribution of Sea Surface Temperature with TIR sensor data. *Italian Journal of Remote Sensing*, 44, 97-107.
- TARANTINO, E. & FIGORITO, B. 2012. Mapping rural areas with widespread plastic covered vineyards using true color aerial data. *Remote Sensing*, 4, 1913-1928.
- TASDEMIR, K. & KOC-SAN, D. Unsupervised extraction of greenhouses using WorldView-2 images. 2014 IEEE Geoscience and Remote Sensing Symposium, 13-18 July 2014 2014. 4914-4917.
- THUNNISSEN, H. & DE WIT, A. 2000. The national land cover database of the Netherlands. *ISPRS Journal of Photogrammetry & Remote Sensing*, 33, 223-230.
- TIAN, J. & CHEN, D. M. 2007. Optimization in multi-scale segmentation of high-resolution satellite images for artificial feature recognition. *International Journal of Remote Sensing*, 28, 4625-4644.
- TOWNSHEND, J. R., JUSTICE, C. O., GURNEY, C. & MCMANUS, J. 1992. The impact of misregistration on change detection. *IEEE Transactions on Geoscience and Remote Sensing*, 30, 1054-1060.
- VILLARREAL-GUERRERO, F., KACIRA, M., FITZ-RODRÍGUEZ, E., KUBOTA, C., GIACOMELLI, G. A., LINKER, R. & ARBEL, A. 2012. Comparison of three

- evapotranspiration models for a greenhouse cooling strategy with natural ventilation and variable high pressure fogging. *Scientia Horticulturae*, 134, 210-221.
- WITHARANA, C. & CIVCO, D. L. 2014. Optimizing multi-resolution segmentation scale using empirical methods: Exploring the sensitivity of the supervised discrepancy measure Euclidean distance 2 (ED2). *ISPRS Journal of Photogrammetry and Remote Sensing*, 87, 108-121.
- WU, C. F., DENG, J. S., WANG, K., MA, L. G. & TAHMASSEBI, A. R. S. 2016. Object-based classification approach for greenhouse mapping using Landsat-8 imagery. *International Journal of Agricultural and Biological Engineering*, 9, 79.
- WULDER, M., WHITE, J., ALVAREZ, F., HAN, T., ROGAN, J. & HAWKES, B. 2009. Characterizing boreal forest wildfire with multi-temporal Landsat and LIDAR data. *Remote Sensing of Environment*, 113, 1540-1555.
- XU, H. 2010. Analysis of impervious surface and its impact on urban heat environment using the normalized difference impervious surface index (NDISI). *Photogrammetric Engineering & Remote Sensing*, 76, 557-565.
- YANG, J., HE, Y., CASPERSEN, J. & JONES, T. 2015. A discrepancy measure for segmentation evaluation from the perspective of object recognition. *ISPRS Journal of Photogrammetry and Remote Sensing*, 101, 186-192.
- ZHANG, J., PU, R., YUAN, L., WANG, J., HUANG, W. & YANG, G. 2014. Monitoring powdery mildew of winter wheat by using moderate resolution multi-temporal satellite imagery. *PloS one*, 9, e93107.
- Zhao, G. X., Li, J., Li, T., Yue, Y. D. & Warner, T. 2004. Utilizing landsat TM imagery to map greenhouses in Qingzhou, Shandong Province, China. *Pedosphere*. 14(3): 363-369.

CHAPTER 2: A new Threshold Relative Radiometric Correction Algorithm (TRRCA) of Multiband Satellite Data.

In the previous chapter, the attention was focused on a single Land Cover (LC) class. In this one, the topic is beyond the improvement of the detection of a single LC and is related to the enhancement of passive satellite images for multitemporal studies. Indeed, it is well known that remotely sensed scenes could be affected by many factors (such as atmospheric conditions, topographic effects, sun angle and so on) and, for radiometric consistency among temporal images, these unwanted effects must be removed for optimum change detection. The goal of radiometric corrections is to reduce the above effects.

In this chapter, a new algorithm is proposed for PIF (Pseudo Invariant Features) extraction and relative radiometric normalization. The new Threshold Relative Radiometric Correction Algorithm (TRRCA) can be labelled as a supervised one and combines three methods for the detection of PIF: Moment distance index (MDI), Normalized Difference Vegetation Index (NDVI) masks, morphological erosion and dilate operators.

To prove its effectiveness, the algorithm was tested by using Landsat 8 scenes in different environments over the world. Particularly the chosen test areas are the heterogeneous landscape of the Italian Apulia Region, the “Mar de Plástico” landscape of Almeria, the Himalayan mountain chain (Nepal) and Sahara Desert (Egypt).

Since the dependence from user driven parameters, many tests were performed to provide a set of valid input thresholds for the chosen environments. Lastly, the results

achieved with the proposed algorithm were compared with the well-known IR-MAD (Iteratively Reweighted Multivariate Alteration Detection). The comparisons were assessed through the use of statistical tests and showed very good and stable results in the four different study areas. The IR-MAD showed its best result on the Egyptian test area whereas in other test areas featured some localized errors.

The achieved results showed that the proposed algorithm can be a valid, and in some cases better, alternative to the existing approaches.

2.1 *Introduction*

In the last decades, satellite image analysis has provided invaluable data for environment monitoring and change detection (CD) analysis (Janzen et al., 2006). However, remote sensing observations are instantaneous and are affected by many factors, such as atmospheric conditions, topographic effects, sun angle, viewing angle, dynamic changes of environment and changes in the sensor calibration over time (Du et al., 2002). These unwanted effects must be removed for radiometric consistency among temporal images, remaining only land-leaving radiances, for optimum change detection. To detect measurable landscape changes, as revealed by changes in surface reflectance from multi-date satellite images, it is necessary to carry out a radiometric correction. Two approaches to radiometric correction are possible: absolute and relative (Yang and Lo, 2000).

In absolute radiometric correction, atmospheric radiative-transfer codes (e.g. 6Sv, MODTRAN) are used to obtain the reflectance at the Earth's surface from the measured spectral radiances. The absolute method corrects for the following factors: changes in satellite sensor calibration over time, differences among in-band solar spectral irradiance, solar angle, variability in Earth-Sun distance, and atmospheric interferences. These techniques depend on in situ data and sensor parameters as inputs into atmospheric radiative transfer algorithms. For most historically remote scenes, these data are not available, and for planned acquisitions, the data (containing ozone, surface pressure or water vapor) may

be difficult to obtain. Consequently, absolute surface reflectance retrieval may not always be practical (Du et al., 2002).

An alternative to absolute radiometric correction is the relative correction, which is commonly used in one of two ways; adjusting bands of data within a single image and normalizing bands in images of multiple dates relative to a Reference (R) image (Jensen, 1996). Relative methods work with at least two scenes, the reference and one or more target (T). The target scene is corrected by simulating atmospheric and illumination conditions occurred during the acquisition of the reference image (Biday and Bhosle, 2010). Common image based methods are the Dark-object subtraction (DOS) (Chavez Jr, 1988, Hadjimitsis et al., 2003, Mandanici et al., 2015) and the histogram matching (HM) (Gonzalez and Woods, 2008). In the former, the basic idea is finding a surface whose reflectance is so low that its contribution to the signal recorded by a sensor is negligible if compared with the radiance diffused by the atmosphere; in the latter, HM transforms the subject image histogram into the specified histogram of a given reference image so that the radiometric appearance of the image to be transformed and the R image become similar (Novelli et al., 2016b, Yang and Lo, 2000). Coppin and Bauer (1996) suggested using histogram matching before differencing TM data to reduce the radiometric difference impact. Yang and Lo (2000) empirically compared the performance of histogram matching (HM) method with other linear methods on Landsat MSS data such as pseudo-invariant feature set (PIF) method.

Many researchers opt for a linear radiometric normalization method for multi temporal analysis (e.g. Du et al. (2002), Canty and Nielsen (2008)). The common form for linear radiometric image normalization is (Equation 13):

$$Y_k^N = g_k * X_k + o_k$$

Equation 13. Linear equation between reference and target.

Here X_k is the reflectance from the k-th band of the target scene X, Y_k^N is the normalized reflectance of the k-th band of the reference scene Y, g_k and o_k are respectively the evaluated gain and offset implemented for the k-th band of the target scene.

Several methods have been proposed for the radiometric normalization of multitemporal images (Canty and Nielsen, 2008, Canty et al., 2004, de Carvalho et al., 2013, Hussain et al., 2013). The linear regression method is the most widely used approach for relative correction. The first attempts were based on simple regression considering all pixels of multitemporal images (Jensen, 1996, Tokola et al., 1999). Subsequently, normalization was performed considering landscape elements with reflectance values that are nearly constant over time. These areas belong to the so called pseudo-invariant features (PIF) (Caselles and Lopez Garcia, 1989, Schott, 1989).

This chapter shows a new PIF selecting algorithm combining Moment Distance Index (MDI) thresholding, Normalized Difference Vegetation Index (NDVI) masks and morphological erosion and dilation operators. The proposed method was called Threshold Relative Radiometric Correction Algorithm (TRRCA) and was tested in different environments over the world to verify its robustness against different conditions.

The chosen areas are the heterogeneous landscape of the Italian Apulia Region, the “Mar de Plástico” landscape of Almeria (Spain), the Himalayan mountain chain (Nepal) and the Sahara Desert (Egypt). For each test area, has been defined a set of optimal input parameters to statistically compare the TRRCA with the well-known IR-MAD (Iteratively Reweighted Multivariate Alteration Detection) outputs. To the Ph.D. candidate knowledge, this is the first proposed method that takes into account both the MDI (Salas et al., 2016, Salas and Henebry, 2013, Salas and Henebry, 2012, Aguilar et al., 2016c) and morphological operators. Moreover, the simple conceptual formulation and the good results achieved in comparison with the IR-MAD, over the same test areas, showed that the TRRCA can be considered a valid alternative to existing approaches.

In the next sections a state of the art regarding PIF extraction is proposed to show the novelty of the proposed work; then the test areas, the input data, the mathematics behind the TRRCA and the selection of the optimal parameters will be described; lastly will be shown the comparison between the proposed algorithm and the IR-MAD.

2.2 Pseudo-Invariant Features Extraction

Efficient PIF detection plays a key role within the image regression process. According to (Eckhardt et al., 1990) PIF should:

- be located at the same elevation for a better representation of the atmospheric conditions across the scene;
- contain only minimal amounts of vegetation to reduce change in spectral reflectance over time;
- be located in relatively flat areas to minimize the effects of solar azimuth differences and shadows;
- not exhibit changes in their spatial pattern;
- have a wide range of brightness values for the regression model to be reliable.

Generally, PIF are built features such as flat roofs, roads, other non-natural surfaces, and deep man-made water bodies. By definition, PIF should remain spectrally constant and unaffected by seasonal or biological cycles (Bao et al., 2012). They could be selected by visual inspection of multitemporal images. However, manually PIF selection is time-consuming and affected by the analyst subjectivity (Schroeder et al., 2006). In the last two decades, and especially in recent years, many authors have been studying semi-automatic/automatic methods for selecting pixels that can be considered invariant over time.

Schott (1989) proposed the usage of the band ratios between near infrared and red bands to select non-vegetated elements and non-water elements in different acquisition. Caselles and Lopez Garcia (1989) developed a relative correction based on the idea that the atmospheric effects, over two or more dates, can be studied in a relative way simply using the apparent reflectance of selected targets. This reflectance is supposed unchanged over time. Hall et al. (1991) performed a tasseled cap transformation to identify potential no-change pixels a priori. Elvidge et al. (1995) implemented the automatic scattergram controlled regression method which evaluates no-change buffer zones within scattergrams of the same multitemporal bands and then performs a linear regression between the temporal image pairs. Heo and FitzHugh (2000) studied a standardized radiometric normalization method for detecting and deleting outliers from selected targets in order to perform an optimal regression. Furby and Campbell (2001) proposed an extension of the method proposed by Caselles and Lopez Garcia (1989) designed to be robust against targets that

cannot be considered truly invariant over time. Du et al. (2002) selected PIF using principal component analysis (PCA) and a no-change buffer zone. Canty and Nielsen (2008) and Canty and Nielsen (2012), Canty et al. (2004), and Nielsen et al. (1998) developed a new approach adopting canonical variates, calculated from Canonical Correlation Analysis (CCA), instead of original images. The detection of invariant features was carried out by using the differences between the pairs of CCA components called by authors Multivariate Alteration Detection (MAD). Chen et al. (2005) recommended a new method to identify temporally invariant cluster in which a point density map, based on vegetation indices scatter plots, was used to evaluate the normalization regression function. Polemio and Lonigro (2013) showed an algorithm for PIF selection focused on the improvement of the normalization results. Although the authors followed the theoretical framework developed by Du et al. (2002) they extended their studies in order to find common PIF by using scenes belonging to different sensors (Landsat TM and Landsat ETM+). El Hajj et al. (2008) developed a new method for automatic identification of invariant targets within one reference scene and different multitemporal scenes. Their method implemented the use of different raster masks to isolate targets used for the calculation of the linear regression. Biday and Bhosle (2010) performed radiometric correction using Fourier transform. Kim et al. (2012) developed a new relative approach for PIF detection based on the spectral profile shape of hyperspectral data, particularly they used the spectral angle mapping algorithm output and the application of the cumulative moving average concept to extract PIF. O'Connell et al. (2013) developed a revised version of the temporal invariant clusters method. de Carvalho et al. (2013) proposed an algorithm for radiometric normalization by using PIF selected through similarity and spectral distance measures, density scatter plot method and robust linear regression. Sadeghi et al. (2013) used an artificial neural network to perform a relative radiometric normalization on remotely sensed data. In particular, they showed an automatic method for selecting invariant pixels using change vector analysis, PCA and k-means clustering algorithm. Philpot and Ansty (2013) instead of statistic procedures derived an analytical expression that relates PIF to radiometric properties of the scenes. Sykas et al. (2013) proposed two spectral metrics for the selection of invariant pixels, the absolute normalized difference and the absolute normalized ratio. Garcia-Torres et al. (2014) showed a procedure for semi-automatic normalization of multitemporal scenes based on vegetated PIF. The procedure was called ARIN and its input data and the image correction factor were evaluated from

manually selected vegetated areas assumed invariant over time. Lin et al. (2015) proposed a method for detecting invariant pixels bases on weighted PCA. The authors modified the procedure explained in Du et al. (2002) adding weights within the estimations by using density information of scatterplots and spectral similarities of pixels.

Many works were focused on the comparison of different relative radiometric normalization (RRN) techniques (Eivazi et al., 2015, Fernandes and Leblanc, 2005, Henebry and Su, 1993, Hong and Zhang, 2008, Koukal et al., 2007, Michener and Houhoulis, 1997, Song et al., 2001). In particular, Yuan and Elvidge (1996) compared different RRN techniques on Landsat Multispectral scanner. They also showed the result of the application of the Schott (1989) method and of the automatic scattergram controlled regression method (Elvidge et al., 1995). Yang and Lo (2000) compared five RRN techniques showing that all five methods were able to reduce radiometric differences between two Landsat MSS images. Olthof et al. (2005) carried out the comparison of two normalization methods by using the Theil-Sen robust regression technique. Janzen et al. (2006) tested the differences between absolute and relative correction techniques with Landsat TM and ETM+ scenes. Caprioli et al. (2006) compared the MAD algorithm and the empirical line calibration for three Landsat ETM + scenes. Schroeder et al. (2006) tested the application of two absolute correction techniques and three relative correction techniques with the aim of producing consistent temporal reflectance trajectories of forest areas. Bao et al. (2012) compared automatic PIF selection by PCA with manual selection over rural and urban areas. Xu et al. (2012) carried out the comparison of three relative radiometric correction techniques (MAD, PCA and local radiometric correction) for ALOS AVNIR-2 scenes.

Relative Radiometric correction through selection of invariant targets is an active topic for thermal infrared scenes too (Mustafizur Rahman et al., 2014, Nielsen et al., 2002, Rahman et al., 2015, Scheidt et al., 2008, Tan et al., 2012).

2.3 Study Areas and Dataset

The TRRCA has been applied in four different test areas: the heterogeneous landscape of the Italian Apulia Region, in a portion of the Himalayan mountain chain (Nepal), in a portion of the Sahara Desert (Egypt) and in the “Mar de Plástico” landscape of Almería (Spain). For each test two Landsat 8 scenes were used respectively as reference and target (Table 12 and Figure 16, Figure 17, Figure 18 and Figure 19).

The Apulia Region is the most Eastern Italian (I) region. The climate of the selected area is typically Mediterranean and characterized by moderately rainy winters and hot and dry summers (Novelli et al., 2016a). The landscape changes considerably from season to season and this is mainly due to the extensive agricultural activities (Giordano et al., 2015). In fact, a marked differentiation exists between seasonal and permanent vegetation. The chosen Apulian area was selected to assure a great heterogeneity (small number of natural/artificial common reflectors) between the reference scene and target to test the method within the fragmented agricultural landscape of the Apulia region.

The Nepalese (N) area was chosen for the presence of high topographic gradient and permanent ice. Specifically, within the test area fall some of the highest peaks over the world (Singu Chuli 6501 m, Gangapurna 7455 m, Annapurna III 7555 m, Hiunchuli 6441 m, Machhapuchhare 6993 m) and the northern part of the Modi river catchment. No topographic correction was performed.

The Spanish (S) test area is located in the so-called “Sea of Plastic” (Mar de Plástico), in the province of Almería (Southern Spain). The main economic activity is agriculture under plastic covered greenhouses (Novelli et al., 2016a). Different typologies of plastic materials are used to cover greenhouse structures. The “Sea of Plastic” test area was chosen to test the TRRCA with homogenous artificial areas (high number of common artificial reflectors).

The Sahara test area falls within the Egyptian (E) national confines and was chosen to test the TRRCA over homogenous natural areas (high number of common natural reflectors).

Landsat 8 satellite takes images covering the entire Earth every 16 days and carries a two-sensor payload, the Operational Land Imager (OLI, described in Table 13) and the Thermal Infrared Sensor (TIRS). The OLI and TIRS spectral bands remain broadly comparable to the Landsat 7 Enhanced Thematic Mapper plus (ETM+) bands.

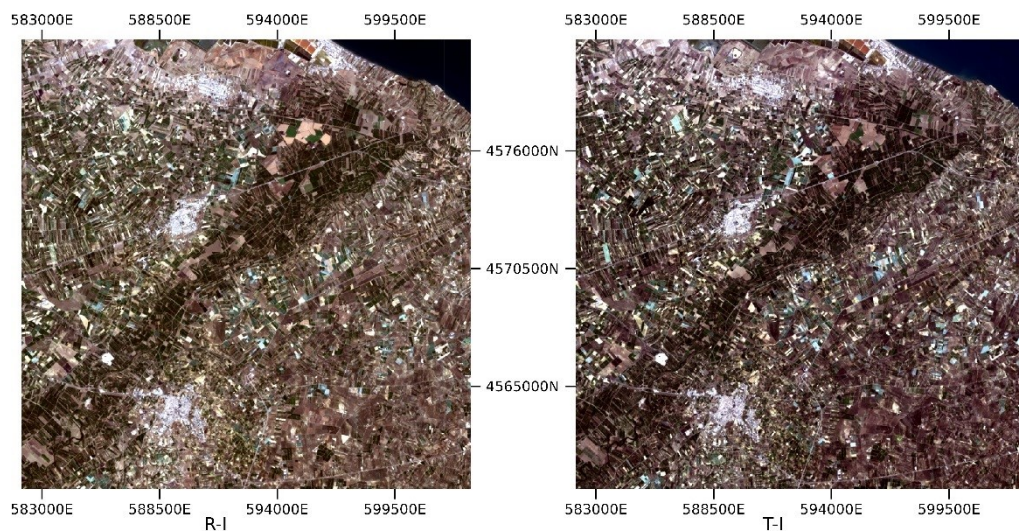


Figure 16. Reference-Italian (R-I) and Target-Italian (T-I) scenes used in this study. Coordinate System UTM WGS 84 zone 33N.

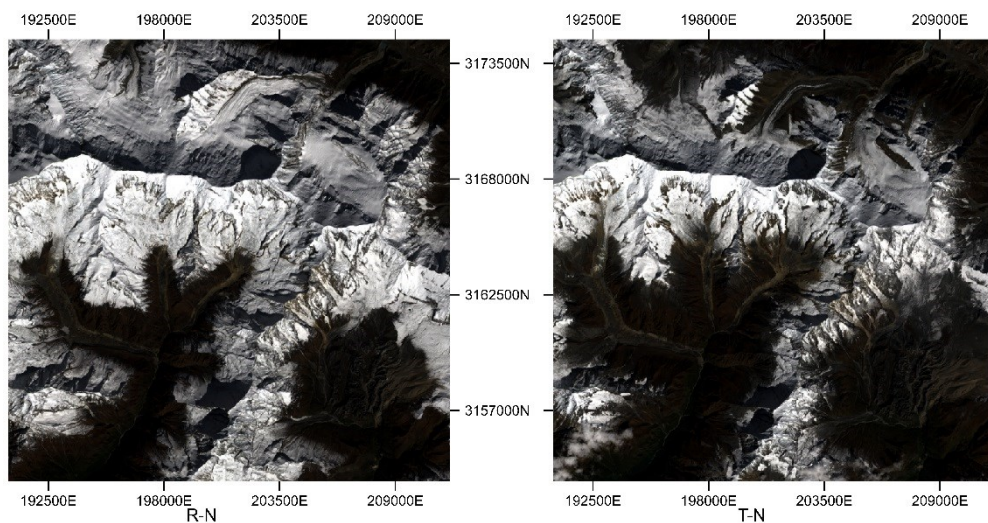


Figure 17. Reference-Nepalese (R-N) and Target-Nepalese (T-N) scenes used in this study. Coordinate System UTM WGS 84 zone 45N.

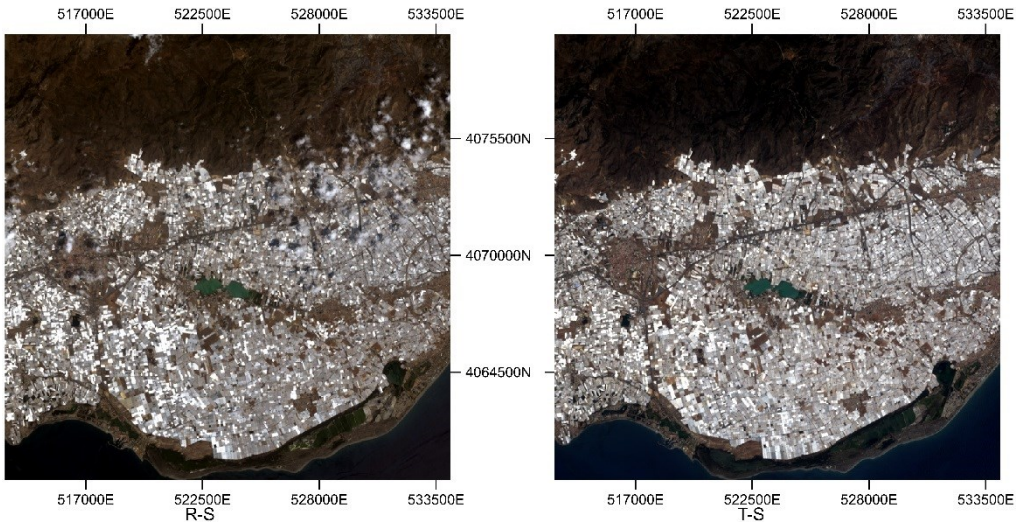


Figure 18. Reference-Spanish (R-S) and Target-Spanish (T-S) scenes used in this study. Coordinate System UTM WGS 84 zone 30N.

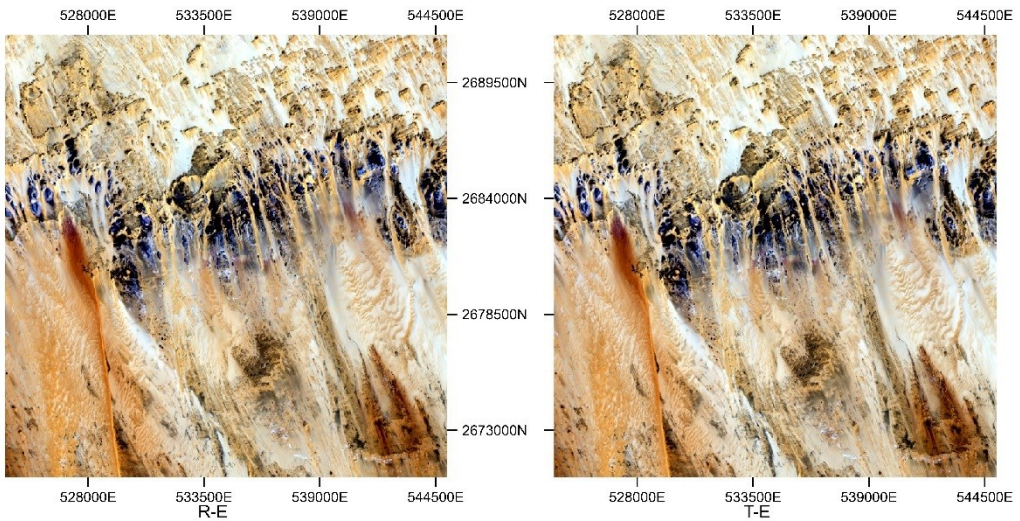


Figure 19. Reference- Egyptian (R-E) and Target- Egyptian (T-E) scenes used in this study. Coordinate System UTM WGS 84 zone 35N.

In detail the OLI sensor has two additional reflective wavelength bands: a new shorter wavelength blue band (0.43–0.45 μm) and a new shortwave infrared band (1.36–1.39 μm) for cirrus cloud detection (Wulder et al., 2015). All the OLI and TIRS spectral bands are stored as geolocated 16-bit digital numbers. The 100 m TIRS bands are

resampled by cubic convolution to 30 m and co-registered with the 30 m OLI spectral bands (Roy et al., 2014a).

The OLI digital numbers of the eight Landsat 8 images were linearly converted to sensor Top of Atmosphere (TOA) reflectance and then corrected for the sun angle using gains, offsets and local sun elevation values stored in each scene metadata.

The following *Equation 14* is used to convert DN values to TOA reflectance, correcting for the sun angle:

$$\rho\lambda' = M_{\rho} * Qcal + A_{\rho}$$

Equation 14. TOA reflectance Equation.

Acquisition date	Scene ID	Subset
7 August 2013	LC81880312013219LGN00	R-I
10 August 2014	LC81880312014222LGN00	T-I
24 October 2013	LC81420402013297LGN00	R-N
11 October 2014	LC81420402014284LGN00	T-N
13 July 2014	LC82000342014194LGN00	R-S
30 June 2016	LC82000342015181LGN00	T-S
01 August 2013	LC81780432013213LGN00	R-E
04 August 2014	LC81780432014216LGN00	T-E

Table 12. Reference (R) and Target (T) scenes used in this study for the Italian (I), Nepalese (N), Spanish (S) and Egyptian (E) test areas.

Where $\rho\lambda'$ is TOA reflectance, without correction for the solar angle; M_{ρ} is the band-specific multiplicative rescaling factor from the metadata; A_{ρ} is the band-specific additive rescaling factor from the metadata and $Qcal$ is the quantized and calibrated standard product pixel values (DN).

The TOA reflectance was corrected with the *Equation 15*.

$$\rho\lambda = \frac{\rho\lambda'}{\cos(\theta_{SZ})} = \frac{\rho\lambda'}{\sin(\theta_{SE})}$$

Equation 15. TOA reflectance equation corrected with the sun elevation angle.

Where $\rho\lambda$ and θ_{SE} are respectively the TOA reflectance and the local sun elevation angle (as defined in the Landsat 8 (L8) Data User Handbook).

The integrity of the subsets extracted from the eighth scenes was checked through the Landsat 8 Quality Assessment (QA) Band. QA band was unpacked by using the L-DOPE Toolbelt, a no-cost tool available from the USGS Landsat-8 website (Roy et al., 2002).

Band Number	Band description	Wavelength (μm)	Geometric resolution
Band 1	coastal blue	0.43–0.45	30 m
Band 2	blue	0.45–0.51	30 m
Band 3	green	0.53–0.59	30 m
Band 4	red	0.64–0.67	30 m
Band 5	near infrared	0.85–0.88	30 m
Band 6	shortwave infrared	1.57–1.65	30 m
Band 7	shortwave infrared	2.11–2.29	30 m

Table 13. Landsat 8 Operational Land Imager (OLI) bands.

2.4 *Proposed algorithm*

A flowchart of the proposed radiometric normalization method is shown in Figure 20. The method was not designed to deal with the panchromatic, the cirrus and the two TIRS bands.

The PIF selection algorithm combines the extraction of dark (local minimum) and bright targets (local maximum) through morphological operators, NDVI masks and MDI measures (Equation 16). Only the pixels positive to all the imposed conditions are selected as PIF. Lastly, all the computation for the proposed algorithm were performed by using the capability of the Numpy/Scipy libraries (Van Der Walt et al., 2011).

$$PIFs = M_{morph} \cap M_{NDVI} \cap M_{MDI}$$

Equation 16. TRRCA equation.

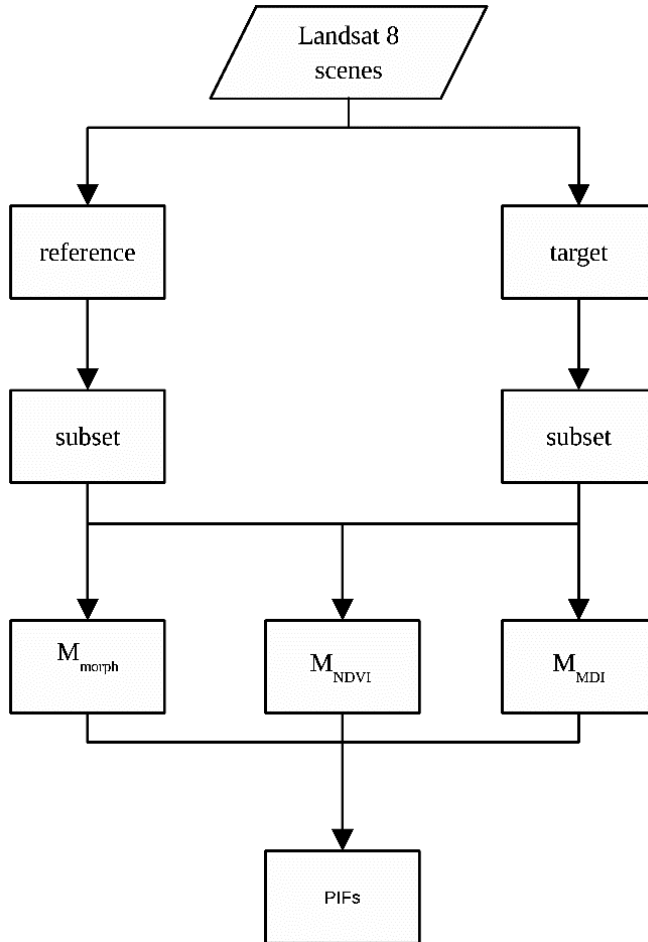


Figure 20. Flowchart of the proposed PIF extraction method.

2.4.1 Morphological operators

According to Hall et al. (1991), the attention should be focused on bright and dark areas respectively characterized by local maximum and minimum reflectance values within specific bands. Indeed, it is assumed that if the location of local maximum (minimum) reflectance values are common for both images, then the considered locations can be considered as candidate PIF.

The blue band was used to locate local minimum often corresponding to water bodies, with calm waters, while bare soil or man-made objects (large roofs, parking lots, etc.) were located based on the red band. Local minimum and maximum were respectively found by using the morphological erosion and dilation.

$$M_{\max} = B_{\max}^R \cap B_{\max}^T$$

Equation 17. Candidate Bright PIF.

$$M_{\min} = B_{\min}^R \cap B_{\min}^T$$

Equation 18. Candidate Dark PIF.

$$B_{\max}^R = \{(Band_4^R \oplus S) \cap Band_4^R\} > 0$$

Equation 19. Morphological Dilation for the reference scene.

$$B_{\max}^T = \{(Band_4^T \oplus S) \cap Band_4^T\} > 0$$

Equation 20. Morphological Dilation for the target scene.

$$B_{\min}^R = \{(Band_2^R \ominus S) \cap Band_2^R\} > 0$$

Equation 21. Morphological Erosion for the reference scene.

$$B_{\min}^T = \{(Band_2^T \ominus S) \cap Band_2^T\} > 0$$

Equation 22. Morphological Erosion for the target scene.

The erosion (dilation) of a digital greyscale image A by a flat structuring element S at any location is defined as the minimum (maximum) value of the image within the region coincident with S . In the subsequent equations, S is defined by a square $n \times n$ matrix with all pixels equal to 1. The coordinates of the origin of S are incremented through all values required so that the structuring element S visits every pixel in A (Gonzalez and Woods,

2008). Lastly, the influence of the structuring element size over the achieved PIF extraction was tested considering seven “n” in the closed interval [3;15] with $n \in 2\mathbb{N} + 1$.

Candidate bright PIF were found by using *Equation 17* on Landsat 8 band 4. *Equation 17* outputs consider only common pixels to the dilated reference and target band 4. Candidate dark PIF were found by using *Equation 18* on Landsat-8 band 2. *Equation 18* outputs consider only pixels common to the eroded reference and target band 2.

Where B_{\max}^R and B_{\max}^T are binary arrays obtained with the application of the dilation operator denoted by the symbol \oplus in *Equation 19* and *Equation 20*; B_{\min}^R and B_{\min}^T are binary arrays obtained with the application of the erosion operator denoted by the symbol \ominus in *Equation 21* and *Equation 22*.

Pixels selected through *Equation 17* and *Equation 18* were used to create a first raster mask (M_{morph}) including the set of candidate PIF (*Equation 23*):

$$M_{\text{morph}} = M_{\max} \cup M_{\min}$$

Equation 23. Morphological mask.

2.4.2 Vegetation Mask

PIF selected through *Equation 23* could fall on vegetated areas. Moreover, they could not be invariant pixel for other bands. To increase the quality of selected PIF, the TRRCA introduces a vegetation mask derived from the very well-known NDVI (Tucker, 1979) showed in *Equation 24* and computed from both reference and target scenes. Although the sensitivity of the NDVI against different atmospheric conditions was already demonstrated (Huete and Liu, 1994), in this case the vegetation index was used only to select PIF over areas with poor vegetation covering and belonging to humid surfaces.

$$\text{NDVI} = \frac{\rho_{\text{NIR}} - \rho_{\text{RED}}}{\rho_{\text{NIR}} + \rho_{\text{RED}}}$$

Equation 24. NDVI equation.

Where ρ_{NIR} and ρ_{RED} are respectively TOA reflectance for band 5 and band 4.

The selection of these areas was achieved fixing three NDVI thresholds by creating a further NDVI mask with *Equation 25*.

$$M_{NDVI} = \{[(NDVI^R < NDVI_{max}) \cap (NDVI^T < NDVI_{max})] \cap [(NDVI^R > NDVI_{mid}) \cap (NDVI^T > NDVI_{mid})]\} \\ \cup [(NDVI^R < NDVI_{min}) \cap (NDVI^T < NDVI_{min})]$$

Equation 25. Mask NDVI equation.

Where $NDVI^R$ and $NDVI^T$ are respectively the NDVI evaluated for the reference and the target scenes. $NDVI_{max}$, $NDVI_{mid}$, $NDVI_{min}$ (with $NDVI_{max} > NDVI_{mid} > NDVI_{min}$) are the three thresholds used to compute M_{NDVI} . To test the influence of these thresholds over the four different environments, several computations were performed (*Table 14*).

Threshold	Interval of values	Step
$NDVI_{max}$	[0.00;0.26[0.05
$NDVI_{mid}$	[-0.10;0.16[0.05
$NDVI_{min}$	[-0.60; -0.09[0.05

Table 14. Thresholds used to test the influence of M_{NDVI} in different environment. The showed Interval of values are open intervals with a step of 0.05.

2.4.3 Moment Distance Index mask

In addition to the aforementioned masks, the TRRCA takes advantage of the Moment Distance Index (MDI) (Salas et al., 2016, Salas and Henebry, 2013, Salas and Henebry, 2012, Aguilar et al., 2016c). To the best knowledge of the Ph.D. candidate, it is the first time that this index is tested in RRN problems.

The MDI is designed to describe the distribution of reflectance values associated with a pixel by calculating the moment distances among the bands and for this reason its contribution was added in the proposed algorithm.

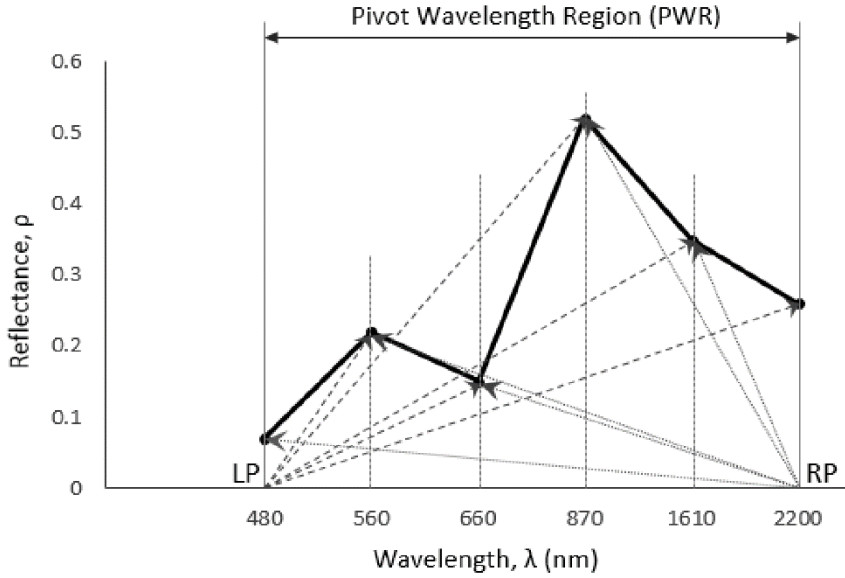


Figure 21. Schematic diagram of MDI applied on a sample spectral reflectance curve of a green vegetation. Note that the number of points between LP and RP pivots can vary depending on the number of bands analyzed or the width of the pivot wavelength region (source Salas et al., 2016).

Considering the pixel spectral signature in a Cartesian plane in which wavelength (λ) and reflectance (ρ) are respectively the abscissa and the ordinate, the index is calculated starting from two pivot locations defined as shorter pivot and longer pivot wavelength. Particularly the left pivot (LP) is related to the shorter wavelength and the right pivot (RP) is related to the longer wavelength. λ_{LP} and λ_{RP} are the wavelengths respectively located at the left and right pivots (Figure 21).

The moment distance from the left pivot (MD_{LP}) to the right one (MD_{RP}) is the sum of the hypotenuses constructed from the left pivot to the reflectance values at i -th successively longer wavelengths (with i from λ_{LP} to λ_{RP}); one base of the triangle is the difference from the left pivot ($i - \lambda_{LP}$) along the abscissa and the other is simply the value at i -th wavelength (Equation 26). Similarly, the moment distance from the right pivot (MD_{RP}) is the sum of the hypotenuses constructed from the right pivot to the reflectance values at successively shorter wavelengths (with i from λ_{RP} to λ_{LP}); one base of the triangle is the

difference from the left pivot ($\lambda_{RP} - i$) along the abscissa and the other is the value at i (Equation 27). The MDI equation is showed in Equation 28.

$$MD_{LP} = \sum_{i=\lambda_{LP}}^{\lambda_{RP}} \sqrt{(\rho_i^2 + (i - \lambda_{LP})^2)}$$

Equation 26. Moment distance from the left pivot.

$$MD_{RP} = \sum_{i=\lambda_{RP}}^{\lambda_{LP}} \sqrt{(\rho_i^2 + (\lambda_{RP} - i)^2)}$$

Equation 27. Moment distance from the right pivot.

$$MDI = MD_{RP} - MD_{LP}$$

Equation 28. Moment distance index.

In the Equation 26 and Equation 27 the wavelengths considered are the central wavelength of the processed bands. The wavelengths are expressed in μm and the reflectances are ranging from 0 to 1. The MDI was computed for each pixel of the reference and target subset. The MDI mask (M_{MDI}) was composed only by the pixels in which the absolute value of the difference between the two MDI (Equation 29), computed for the reference scene (MDI^R) and for the target scene (MDI^T), is less than a specific threshold. These selected pixels were considered as potentials PIF.

$$M_{MDI} = |MDI^R - MDI^T| < 1 \Rightarrow MDI_{diff} < 1$$

Equation 29. Mask MDI equation.

In order to understand the influence of the threshold l on the M_{MDI} (and in the final results) several values within the semi-opened interval $[0.01; 0.31[$, with a step of 0.03 were tested. Considering the implemented values, a MDI_{diff} equal to 0.30 corresponds to 9-12% of difference between MDI^R and MDI^T .

2.4.4 Radiometric Normalization coefficients estimation and selection of potentials high quality PIF extraction

The radiometric normalization coefficients were evaluated for each band by means of the Orthogonal Distance Regression (ODR) algorithm. ODR is the name given to the computational problem associated with finding the maximum likelihood estimator of parameters in measurement error models (Boggs et al., 1987). The ODR algorithm considers both the dependent Y and independent X variables as casual variables (*Equation 30*).

$$\begin{cases} X_i = x_i - \delta_i \\ Y_i = y_i - \varepsilon_i \end{cases}$$

Equation 30. ODR variables definition.

In which X_i and Y_i are the observed random variables with true values x_i and y_i and random errors δ_i and ε_i . In the general formulation, it is assumed that $x_i \in \mathbb{R}^m$ and $y_i \in \mathbb{R}$ and the relationship between true and observed values is given by *Equation 31*.

$$y_i = f(x_i; \boldsymbol{\beta}) \Rightarrow Y_i = f(X_i + \delta_i; \boldsymbol{\beta}) - \varepsilon_i$$

Equation 31. Relationship between true and observed values equations.

In which $\boldsymbol{\beta}$ is a vector of parameters to be estimated. The ODR algorithm does not introduce assumptions over the distribution of the variable x_i and the function f could be either linear or nonlinear. Indeed, the only important assumptions are that f must be a smooth function of its arguments and the normality of the random errors δ_i and ε_i .

Since both X_i and Y_i are affected by random errors, the procedure that estimates the $\boldsymbol{\beta}$ parameter should take this into account. Particularly, this is accomplished considering the orthogonal distance t_i (*Equation 32*) between the i -th observed point (X_i, Y_i) and the estimated curve $f(\tilde{x}, \tilde{\boldsymbol{\beta}})$.

$$t_i^2 = \{\tilde{\varepsilon}_i^2 + \tilde{\delta}_i^2\}$$

Equation 32. Orthogonal distance equation of residual.

The solution to this problem is the one that minimizes the sum of the squares of t_i and is the maximum likelihood estimate of the parameter $\boldsymbol{\beta}$.

In this work the function f , that explains the relationship between PIF belonging to the reference and the target scenes, is linear and the ODR algorithm outputs are the gains and the offsets for each band (as shown in *Equation 13*). Despite for straight line models, there are not strong evidence of the better performance of the ODR method against the

ordinary least square method, in this chapter it was still preferred the ODR method due to its lower bias (Brown and Fuller, 1990, Hurtado et al., 2006).

Each ODR estimation was coupled with the evaluation of the root mean square error (RMSE), correlation coefficient (r) and coefficient of determination (R^2) between PIF TOA reflectance values belonging to the reference and the target scenes. Operationally, in this work was used the Scipy-ODR library that implements the ODRPACK code (Brown and Fuller, 1990). This specific ODR algorithm solves the estimation problem with a Levenberg-Marquardt trust-region strategy. A detailed explanation of the ODR theory and of the solution implemented in the ODRPACK library is beyond the scope of this thesis (further details can be found in the Boggs et al. (1987) paper).

For each test area, almost twenty thousand combinations were considered by varying the structuring element S size (Equation 19 - Equation 22), l (Equation 29), $NDVI_{max}$, $NDVI_{mid}$, $NDVI_{min}$ (Equation 25). For computational time purposes, only tests characterized by an elevated number of retrieved PIF, with high reference-target band by band ODR R^2 and low ODR RMSE were selected as potentials High Quality PIF (HQ-PIF) extraction. This selection was made by introducing a “potential quality parameter” that considers for each test the mean R^2 and the mean RMSE, achieved for the seven considered bands, and the number of PIF normalized (PIF_{norm}) to the total number of pixels within a single considered scene (number of PIF divided by the total number of pixels). The “potential quality parameter” was designed considering an ideal condition of no-change between reference and target. The ideal condition should be characterized by a total number of PIF equivalent to the total number of pixels within the considered area and from a band by band perfect correspondence. An ideally performed regression should feature the parameters showed in Table 15 in which the mean values are calculated considering all the bands at the same time.

Parameter	value
Mean Gain	1
Mean Offset	0
Mean R^2	1
Mean Correlation	1
Mean RMSE	0

PIF _{norm}	1
---------------------	---

Table 15. Results over an ideal no-change condition in which all the pixels in Reference and Target scenes are PIF.

If we imagine an abstract three-dimensional orthonormal space whose axis respectively are the Mean RMSE, the Mean R2 and the PIF_{norm}; then this ideal condition should be represented by a vector with the following components in the abstract space: Mean RMSE = 0, Mean R2 = 1 and PIF_{norm} = 1. Particularly, this vector should be coincident with the bisector of the Mean R2 - PIF_{norm} plane and characterized by a projection on the Mean R2 - Mean RMSE plane overlapping the Mean R2 axis. If α is the angle, expressed in radians, between the projection of the vector in the Mean R2 - Mean RMSE plane and the Mean RMSE axis, and β is the angle, expressed in radians, between the projection of the vector in the Mean R2 - PIF_{norm} plane and the Mean R2 axis (*Equation 33*); then in this ideal no-change case $\alpha = \pi/2$ and $\beta = \pi/4$.

$$\begin{cases} \alpha = \arctan\left(\frac{\text{mean}(R^2)}{\text{mean}(\text{RMSE})}\right) \\ \beta = \arctan\left(\frac{\text{PIF}_{\text{norm}}}{\text{mean}(R^2)}\right) \end{cases}$$

Equation 33. α and β equations: potential quality parameter terms.

The “potential quality parameter” implemented was the sum $\alpha + \beta$. In the ideal condition this parameter is the maximum and equal to $3\pi/4$ whereas in the performed test, due to values of PIF_{norm} near to zero (so β was also close to zero) the computed parameters were always close to $\pi/2$.

For each test area, only the combinations with the “potential quality parameter” above the 98th percentile of all the observed ones were considered as potential good quality PIF extraction.

2.4.5 The IR-MAD correction algorithm

In this chapter, IR-MAD RRN results were compared with the results of the proposed algorithm.

The IR-MAD is an evolution of the previous MAD image-based correction algorithm. The IR-MAD formulation considers two multiband scenes X and Y of k bands. X and Y are supposed to be random vectors: $\mathbf{X} = (X_1, \dots, X_k)^T$ and $\mathbf{Y} = (Y_1, \dots, Y_k)^T$. The IR-MAD algorithm evaluates change (and no-change) information from the difference of two linear combinations of the two considered multiband images (*Equation 34*).

$$\begin{cases} \mathbf{A} = \mathbf{c}^T \mathbf{X} = (c_1 X_1 + \dots + c_k X_k) \\ \mathbf{B} = \mathbf{d}^T \mathbf{Y} = (d_1 Y_1 + \dots + d_k Y_k) \end{cases}$$

Equation 34. linear band combinations of two considered images.

Since X and Y are random vectors then also A and B are random vectors. The random variable $A - B$ is a measure of the change that occurs between the images. With this notation the problem of detecting non-change areas becomes the problem of the definition of the vectors c and d . IR-MAD chose these vector in order to minimize the correlation between A and B which is equivalent to maximizing the variance of $A - B$ (Marpu et al., 2011). A variance equal to one is a further constraint for A and B . This problem can be solved using the Canonical Correlation Analysis (CCA). CCA investigates the relationship between two groups of several variables, finding a linear combination of the original ones. Vectors \mathbf{c} and \mathbf{d} are calculated solving two generalized eigenvalue problems showed in *Equation 35*.

$$\begin{cases} \Sigma_{XY} \Sigma_{YY}^{-1} \Sigma_{XY}^T \mathbf{c} = \rho^2 \Sigma_{XX} \mathbf{c} \\ \Sigma_{XY} \Sigma_{XX}^{-1} \Sigma_{XY}^T \mathbf{d} = \rho^2 \Sigma_{YY} \mathbf{d} \end{cases}$$

Equation 35. Two generalized eigenvalue problems.

Where Σ_{XX} , Σ_{YY} and Σ_{XY} are respectively the covariance matrices of the two images and their cross-covariance. The MAD variates are defined in *Equation 36*.

$$\mathbf{M}_i = \mathbf{A}_i - \mathbf{B}_i = \mathbf{c}_i^T \mathbf{X} - \mathbf{d}_i^T \mathbf{Y}$$

Equation 36. MAD Variates.

Where \mathbf{c}_i and \mathbf{d}_i are the i -th eigenvectors corresponding to the canonical variates, \mathbf{A}_i and \mathbf{B}_i , and to the canonical correlation ρ_i . The MAD transformation is defined in such a way that the canonical variates and the MAD variates are mutually uncorrelated.

Now if we call the variance of the i -th MAD variates $var(MAD_i) = \sigma_{MAD_i}^2$ and we consider the properties of the MAD variates (ideally normally distributed, mutually uncorrelated), is possible to define a new random variable trough *Equation 37*

$$Z = \sum_{i=1}^k \left(\frac{MAD_i}{\sigma_{MAD_i}} \right)^2$$

Equation 37. Sum of squares of uncorrelated and normally distributes random variables.

The random variable Z can be considered as the sum of k squares of uncorrelated and normally distributes random variables and thus is distributed as χ^2 with k degree of freedom. Using the Z variable is possible to define a no-change probability as $Pr(no - change) = 1 - P_{\chi^2, k}(z)$. The no-change probability weights the observations over the iterations of the MAD algorithm until a stop criterion is met. The criterion can be simply a fixed number of iterations or when the change between two consecutive iterations is no more significant. When the stopping criteria is reached the pixels with no-change probability greater than a fixed threshold are selected. They are the input for the orthogonal regression necessary to compute the gain and the offset correction parameters for each band. In this chapter a ready to use MATLAB® IR-MAD source code was downloaded from the web page <http://www.imm.dtu.dk/~alan/>.

Lastly, a detailed explanation of the IR-MAD algorithm is beyond the scope of this manuscript, further details can be found in the Nielsen (2007) paper.

2.5 *TRRCA application and comparisons with IR-MAD algorithm*

The proposed method was tested on eight Landsat 8 scenes (*Table 13*). The first part of the results will be focused on the description of the outputs from the performed tests. Particularly, will be described what in this chapter is supposed to be a HQ-PIF extraction, the influence of the proposed masks over HQ-PIF extractions and of the thresholds related to HQ-PIF extractions.

The second part will be focused on the comparison of the result of the TRRCA (achieved with a random selection of a set of thresholds related to HQ-PIF extractions) and the IR-MAD algorithm.

2.5.1 TRRCA tests results

In section 2.4.4 was explained the criteria used to select potentials HQ-PIF extractions by means of a defined “potential quality parameter”. In this chapter the potentials HQ-PIF extractions are considered good ones if the two-sample t-test, two-sample F-test and two-sample Wilcoxon rank sum test between reference PIF and corrected target PIF were contemporary satisfied at 5% confidence level. Particularly:

- The parametric two sample t test returns a test decision for the null hypothesis that the two considered sampled data comes from normal distributions with equal means and equal but unknown variances (Montgomery and Runger, 2010).
- The parametric two sample F test returns a test decision for the null hypothesis that the two considered sampled data comes from normal distributions with the same variance (Montgomery and Runger, 2010).
- The non-parametric Wilcoxon rank sum test returns a test decision for the null hypothesis that the two considered sampled data comes from distributions with equal medians (Montgomery and Runger, 2010).

The use of parametric tests was already implemented in other studies as confirmation of the quality of the extracted PIF (e.g. Canty and Nielsen (2008)). In this chapter a non-parametric test is proposed as further constrain for the selection of HQ-PIF. As shown in the subsequent section the Wilcoxon rank sum test will be the most restrictive one (especially for the IR-MAD). Lastly, a PIF extraction was considered a HQ-PIF one only if the number of found PIF was at least equal to 100. Otherwise, the considered extraction was not considered since a low number of PIF cannot guarantee an adequate correction over the whole considered test area.

Test area	Number of HQ-PIF extractions	Mean Number of PIF
I	40	752
N	375	789
S	1503	984
E	10504	2246

Table 16. Number of High Quality PIF (HQ-PIF) extractions for the selected Italian (I), Nepalese (N), Spanish (S) and Egyptian (E) test areas.

Table 16 shows the number HQ-PIF extractions for each selected test area obtained following the aforementioned selection method and the mean number of retrieved PIF. Table 16 clearly shows the sensitivity of the proposed algorithm to the abundance of natural/artificial reflectors. Indeed, this was an expected result since a desert area is characterized by a high probability to features PIF properties (e.g. Eckhardt et al. (1990)).

The same can be said for the Spanish area dominated by a high percentage of plastic covered greenhouses and from an arid environment. As regards the Nepalese and the Italian areas, it is little wonder the archived result. The two Nepalese scenes feature permanent glaciers with different extensions and areas with low vegetation cover as probable candidate PIF whereas the Apulian area, characterized by a heterogeneous agricultural landscape, seems to be the most problematic one.

Figure 22 shows the scatter plots of the implemented NDVI thresholds, morphological Kernel and MDI_{diff} versus the number of HQ-PIF for the Italian test area. Both the $NDVI_{max}$ and the Kernel parameters are constant for each HQ-PIF extractions. They are respectively fixed to the highest $NDVI_{max}$ value and the lowest Kernel size. Suitable $NDVI_{min}$ and MDI_{diff} values are respectively concentrated over the higher and lower tested values. Particularly, MDI_{diff} frequency peak is around 0.04. Lastly, all the tested $NDVI_{mid}$ are shown in the HQ-PIF extractions. However, 0.10 and 0.15 are the most common $NDVI_{mid}$ values for the Italian test area.

Figure 23 shows the scatter plots of the implemented NDVI thresholds, Kernel and MDI_{diff} versus the number of HQ-PIF for the Nepalese test area. All the tested $NDVI_{max}$, $NDVI_{mid}$, $NDVI_{min}$ and MDI_{diff} thresholds are present in HQ-PIF extractions. However, only $NDVI_{min}$ shows a more uniform distribution for almost all the tested values.

NDVI_{max}, NDVI_{mid} and MDI_{diff} have their respectively most common values fixed to 0.25, 0.00 and 0.04. Although the most common kernel size is 3×3 , there are also many HQ-PIF extractions with a 5×5 kernel size. Lastly, *Figure 23* depicts that the most common number of extracted HQ-PIF is among 600 and 800 and that are feasible combinations with almost twice as much as the previous HQ-PIF number.

Figure 24 depicts the scatter plots of the implemented NDVI thresholds, Kernel and MDI_{diff} versus the number of HQ-PIF for the Spanish test area. All the tested NDVI_{mid}, NDVI_{min}, MDI_{diff} values and all the tested Kernel size are present in HQ-PIF extractions. NDVI_{min} and MDI_{diff} show a more uniform distribution for almost all the tested values characterized by more extractions with 500-1500 PIF and only a few extractions above 1500 PIF. The most common values of NDVI_{mid} are between 0.05 and 0.10 with the maximum number of extracted HQ-PIF achieved with an NDVI_{mid} equal to 0.05. The most common Kernel sizes are again 3×3 and 5×5 . Particularly lower Kernels sizes are coupled with a greater number of extracted PIF. Lastly, 0.15, 0.20 and 0.25 NDVI_{max} values show a similar behaviour, with the highest frequency on 0.25 and the maximum number of extracted PIF on 0.15.

Figure 25 shows the scatter plots of the implemented NDVI thresholds, Kernel and MDI_{diff} versus the number of HQ-PIF for the Egyptian test area. All the tested NDVI_{mid}, NDVI_{min}, MDI_{diff} values and all the tested Kernel size are present in HQ-PIF extractions. NDVI_{min} shows a more uniform distribution of all the tested values characterized by more extractions with 500-3000 PIF and only a few extractions above 3000 PIF. MDI_{diff} shows again an almost uniform distribution with the maximum number of extracted PIF related to 0.04. The most common Kernel sizes are 7×7 and 9×9 . Particularly lower Kernels sizes are coupled with a greater number of extracted HQ-PIF although the 3×3 Kernel exhibits a more stable number of extracted PIF. Lastly, all the NDVI_{max} values show a similar behaviour with regards to HQ-PIF extractions characterized by 500-3000 extracted PIF whereas greater numbers of extracted PIF were achieved only with higher NDVI_{max} values.

Figure 22, Figure 23, Figure 24 and Figure 25 have shown that there are differences over heterogeneous and homogeneous test areas. For the Nepalese, the Egyptian, and the Spanish test areas all the performed tests have shown that NDVI_{min} and MDI_{diff} are the

parameters that exhibit the major variability. $NDVI_{min}$ exhibits less variability in the Italian test area. According to *Equation 25*, this shows how fragmented agricultural landscapes need a very large number of pixels as candidates PIF in order to increase the potentials HQ-PIF. Indeed, a high $NDVI_{min}$ value considers as candidate PIF all the pixels with an NDVI less than $NDVI_{min}$. *Equation 25* shows also that the $NDVI_{max}$ values near or equal the maximum feasible one are characterized by a higher probability to obtain a great number of HQ-PIF. The $NDVI_{mid}$ values are characterized by a heterogeneous behaviour strongly dependent on the test area. Particularly the Italian and Spanish HQ-PIF extractions are characterized by the occurrence of all the tested $NDVI_{mid}$ values. Probably this occurs since these are the areas with a more heterogeneous vegetation, although in the case of the Spanish data, the effect on NDVI is masked by the presence of plastic coverings. This shows that the M_{NDVI} performs as a coarse PIF filter for a subsequent and improved PIF selection through M_{MDI} and M_{morph} .

For all the test areas, the greatest concentrations of a high number of HQ-PIF extractions occur always with a MDI_{diff} between 0.04 and 0.10. Considering the formulation of the MDI, this is quite interesting since small differences are correlated with very similar spectral signatures (Salas et al., 2016). The MDI filter is still useful with MDI_{diff} greater than 0.10. Indeed, with greater MDI_{diff} , the M_{MDI} performs again as a coarse filter before the application of the morphological operators.

Lastly, *Figure 22*, *Figure 23*, *Figure 24* and *Figure 25* show that feasible Kernel sizes are dependent from the heterogeneity of the test area. Particularly small kernel sizes are always feasible in all the test areas whereas greater ones are feasible only for areas characterized by high homogeneity. Indeed, this is also an expected result since morphological operators consider the local minimum and local maximum over the Kernel area. Because of this, the probability to find a corresponding singular value over the same Kernel areas is higher in smaller areas than in greater ones. This explains why for heterogeneous areas occur only small Kernel sizes whereas for homogeneous areas bigger Kernels perform good results during the RRN process.

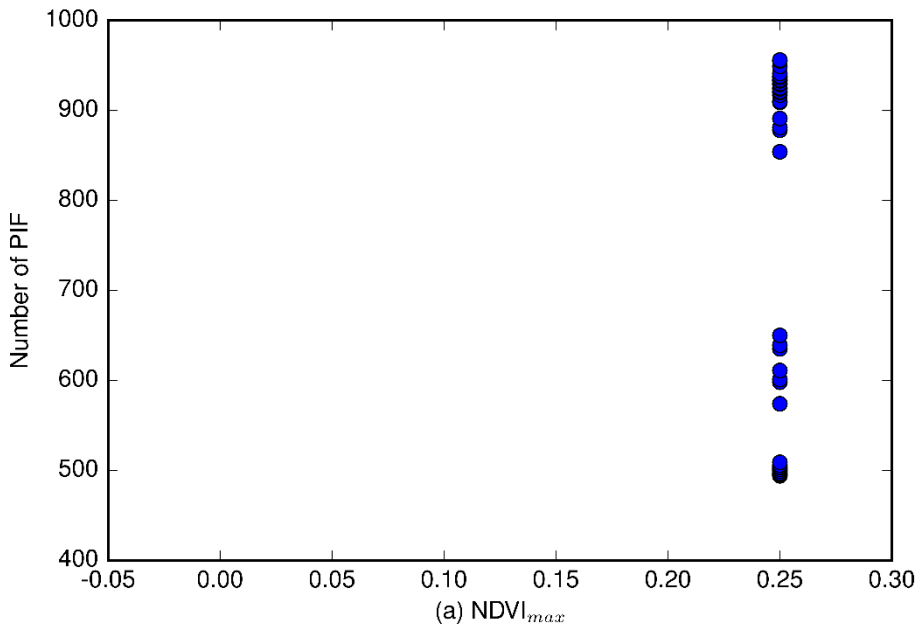


Figure 22 (a) Scatter plot $NDVI_{max}$ - number of PIF for the Italian study area.

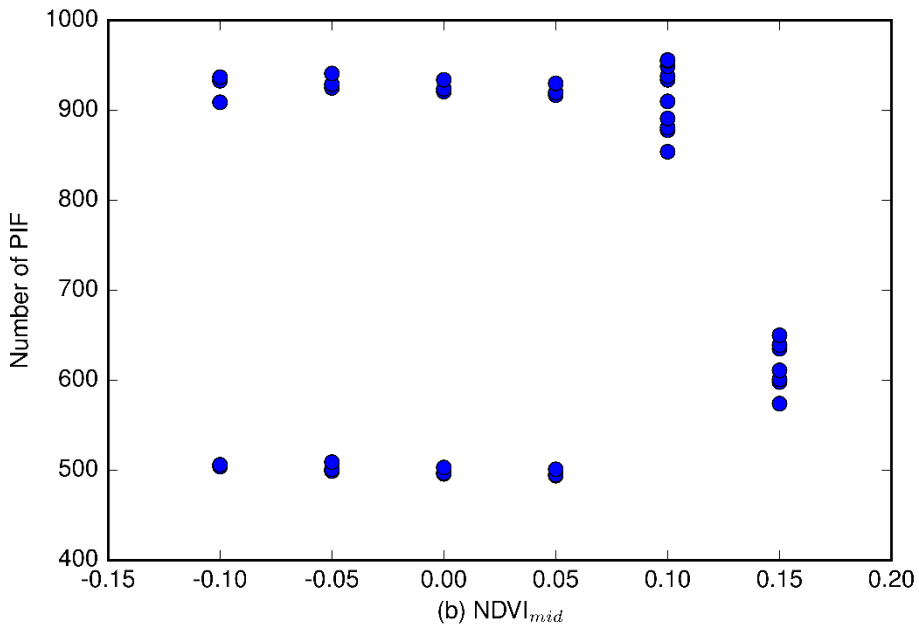


Figure 22 (b) Scatter plot $NDVI_{mid}$ - number of PIF for the Italian study area.

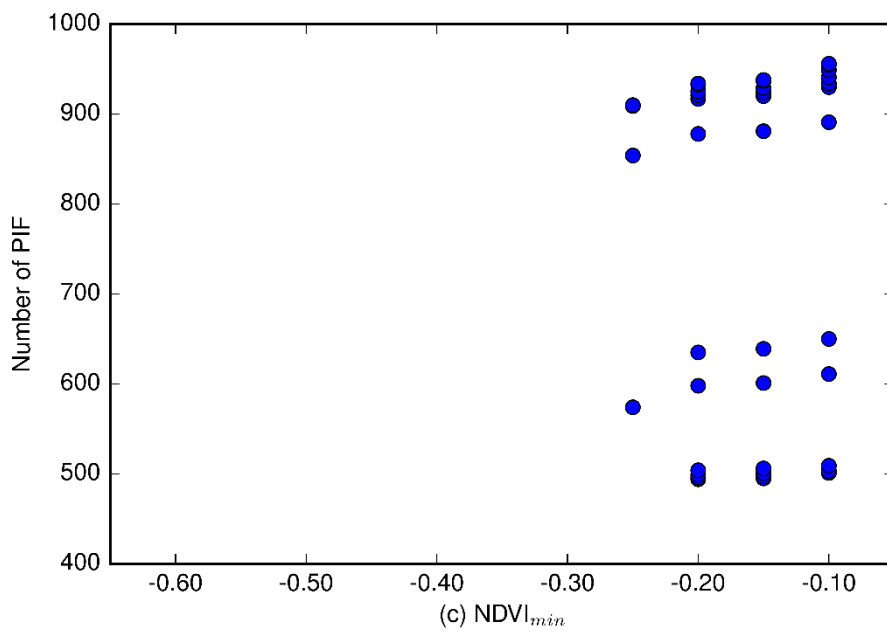


Figure 22 (c) Scatter plot $NDVI_{min}$ - number of PIF for the Italian study area.

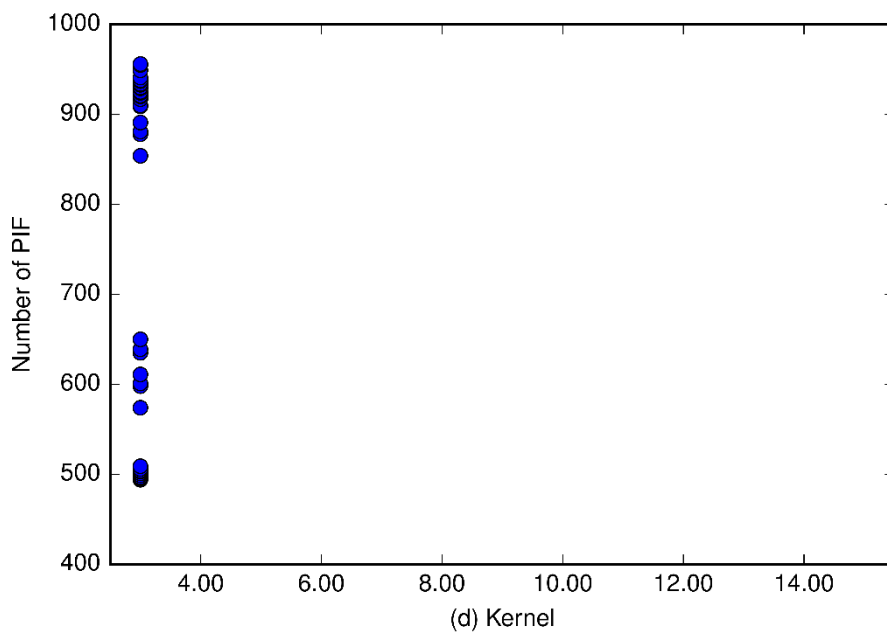


Figure 22 (d) Scatter plot Kernel - number of PIF for the Italian study area.

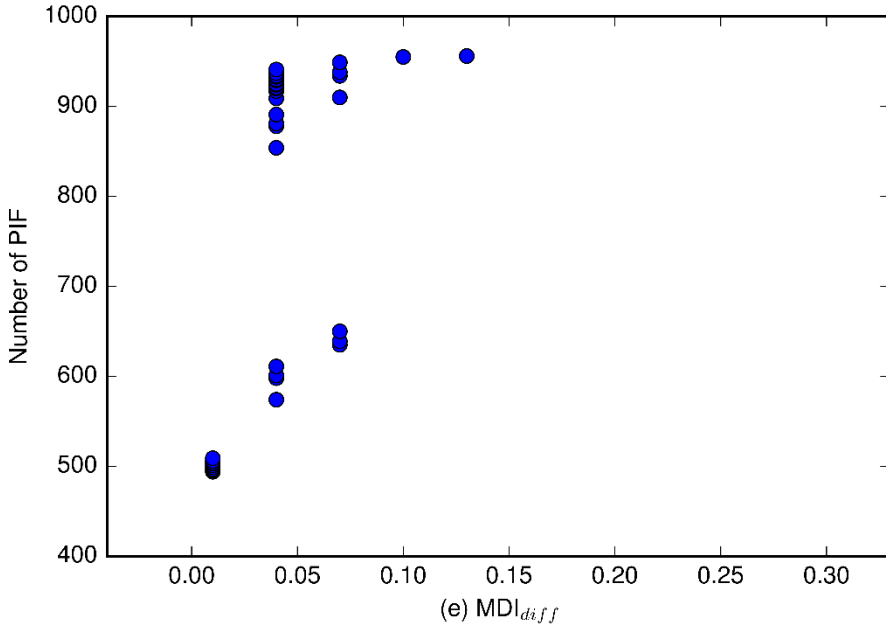


Figure 22 (e) Scatter plot MDI_{diff} - number of PIF for the Italian study area.

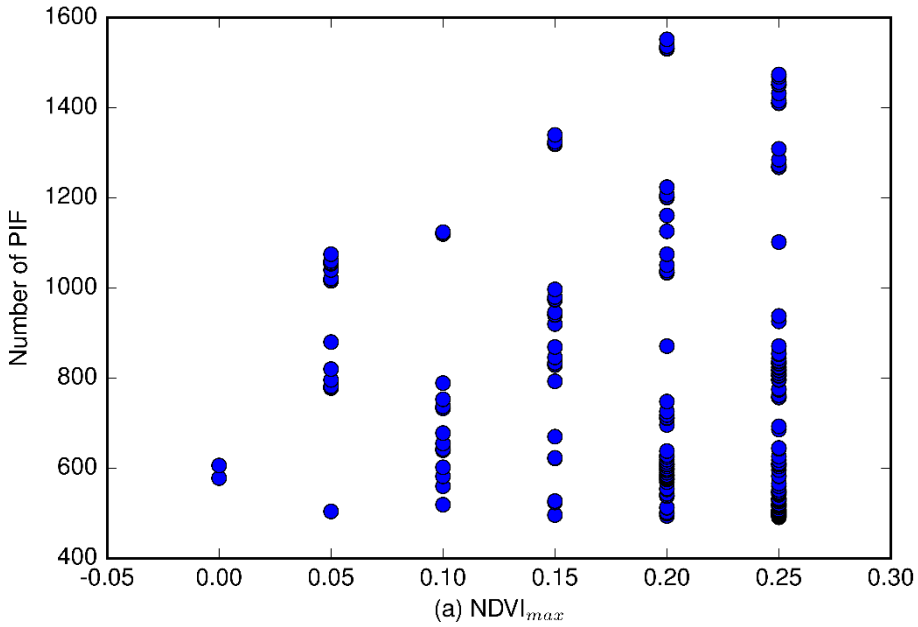


Figure 23 (a). Scatter plot $NDVI_{max}$ - number of PIF for the Nepalese study area.

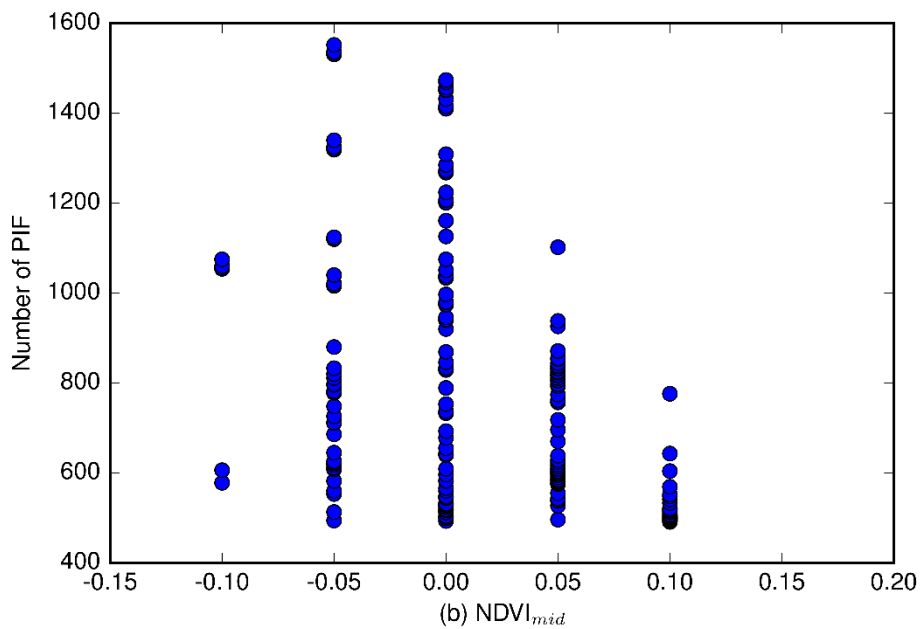


Figure 23 (b). Scatter plot $NDVI_{mid}$ - number of PIF for the Nepalese study area.

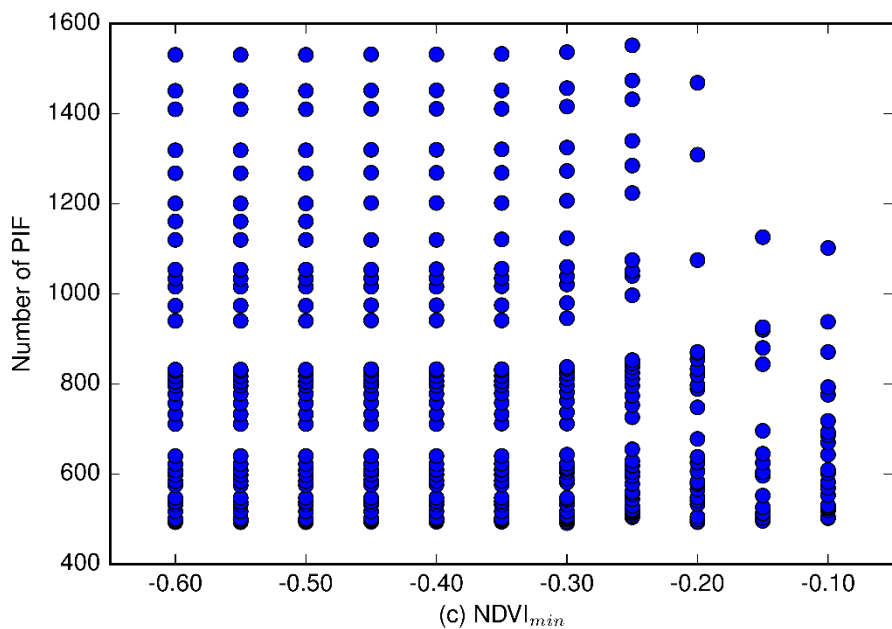


Figure 23 (c). Scatter plot $NDVI_{min}$ - number of PIF for the Nepalese study area.

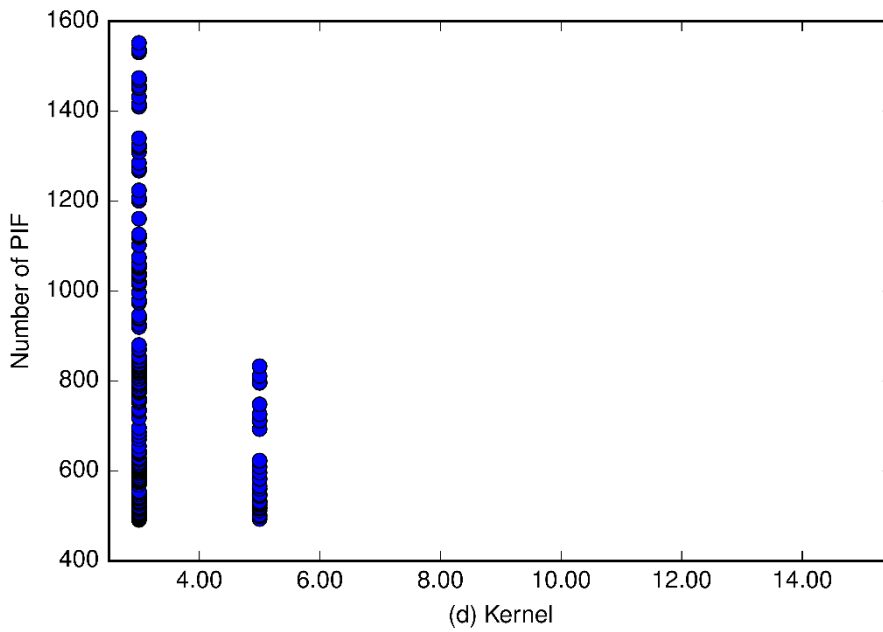


Figure 23 (d). Scatter plot Kernel - number of PIF for the Nepalese study area.

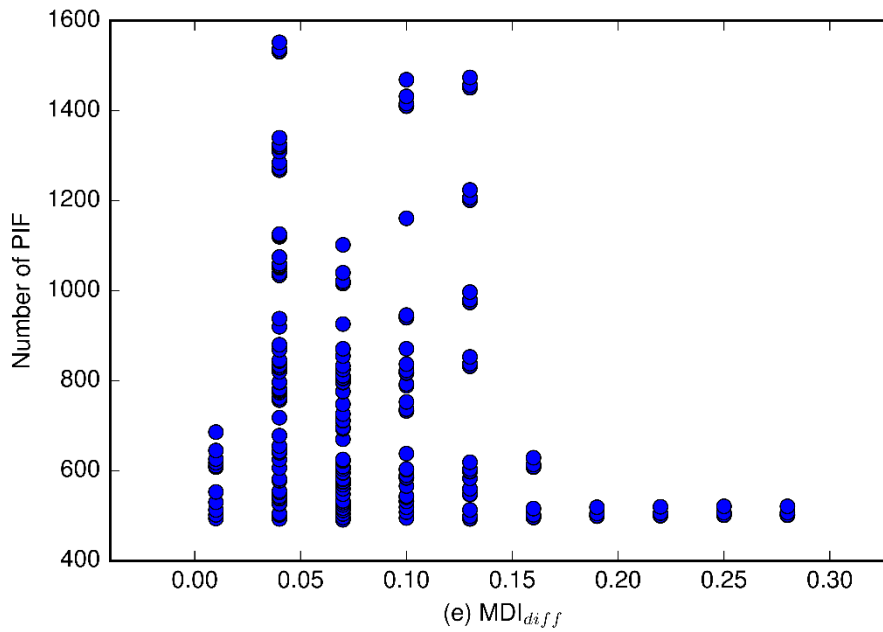


Figure 23 (e). Scatter plot MDI_{diff} - number of PIF for the Nepalese study area.

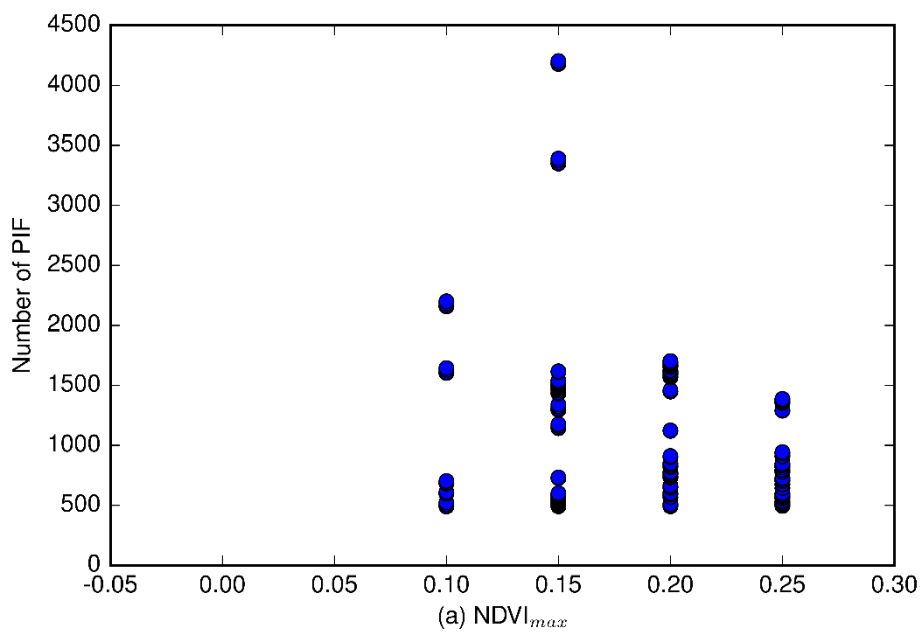


Figure 24 (a). Scatter plot $NDVI_{max}$ - number of PIF for the Spanish study area.

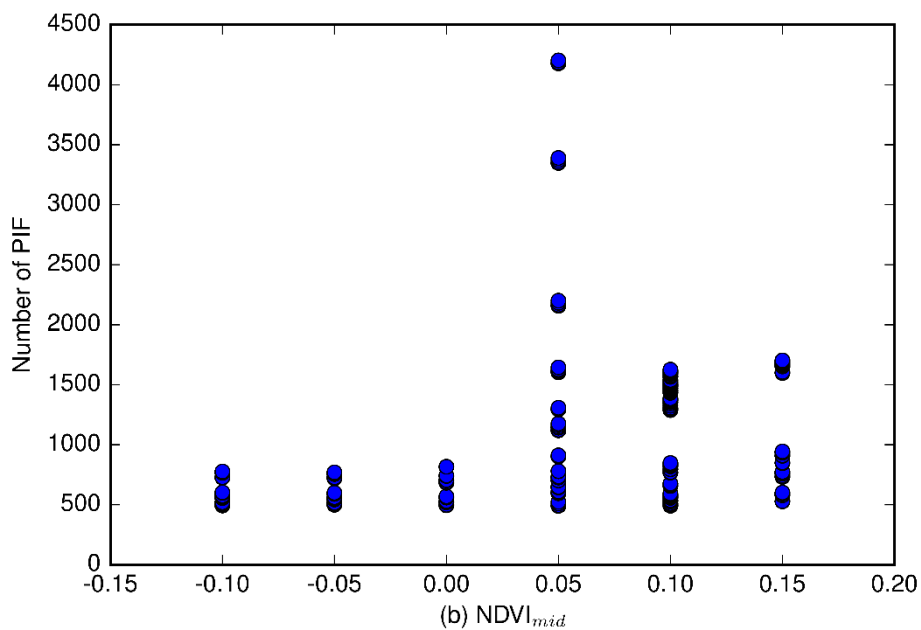


Figure 24 (b). Scatter plot $NDVI_{mid}$ - number of PIF for the Spanish study area.

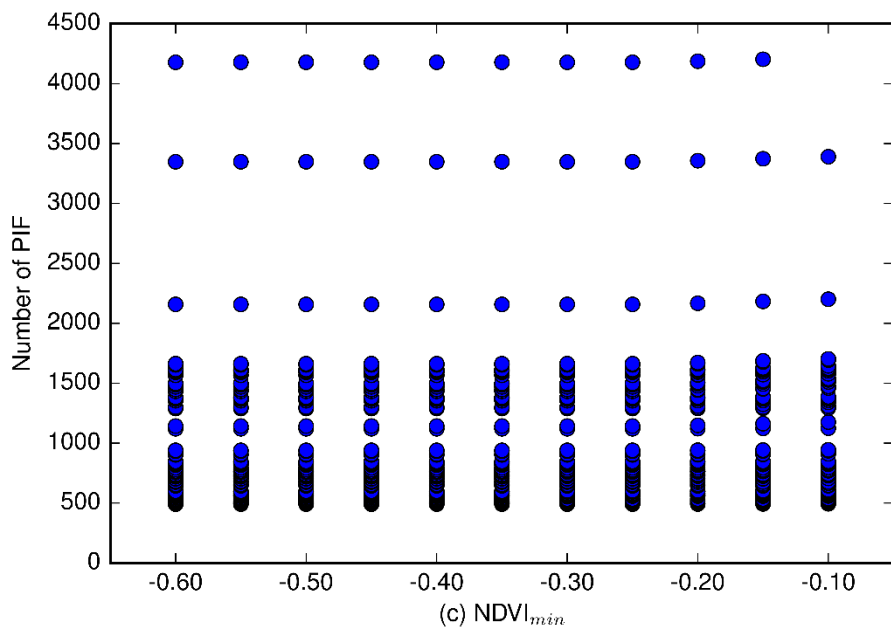


Figure 24 (c). Scatter plot $NDVI_{min}$ - number of PIF for the Spanish study area.

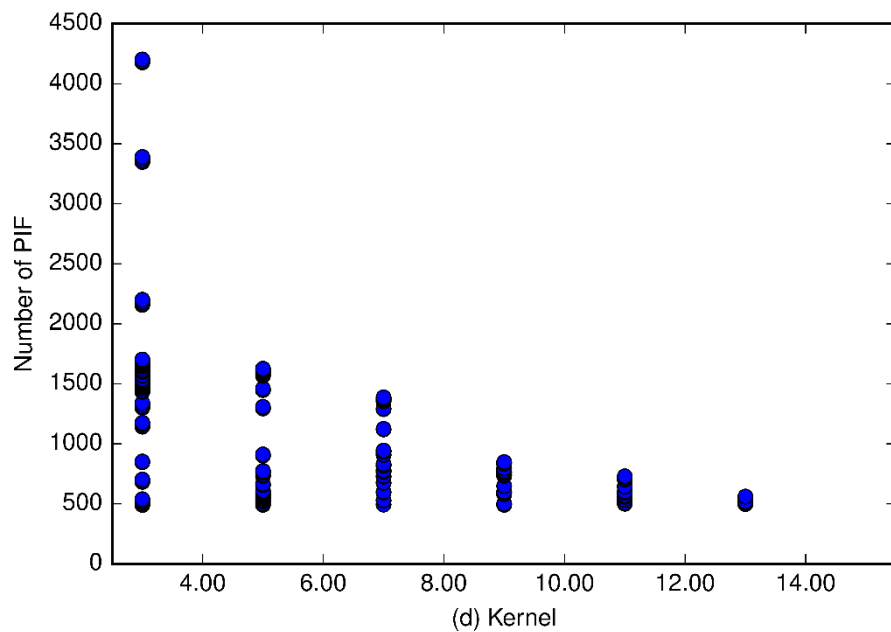


Figure 24 (d). Scatter plot Kernel - number of PIF for the Spanish study area.

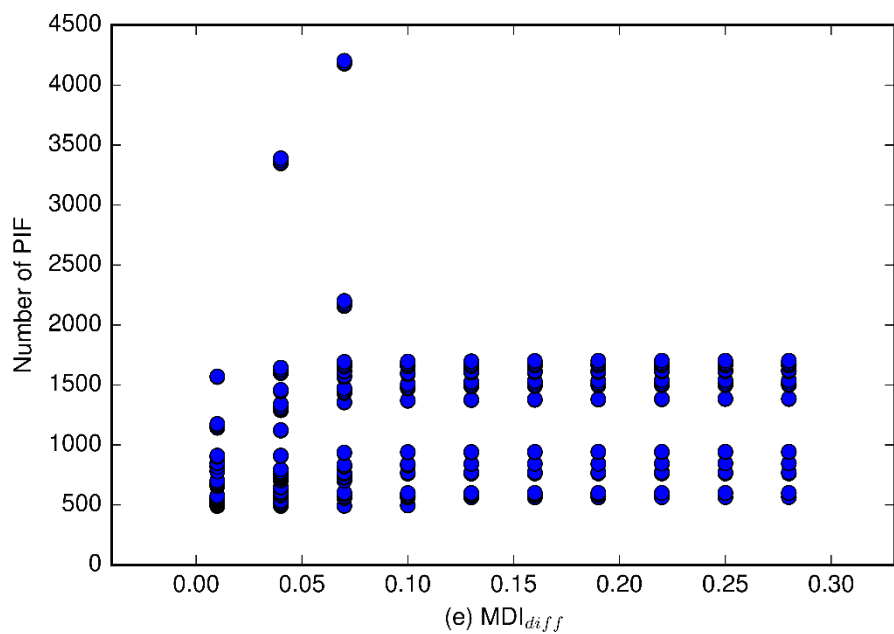


Figure 24 (e). Scatter plot MDI_{diff} - number of PIF for the Spanish study area.

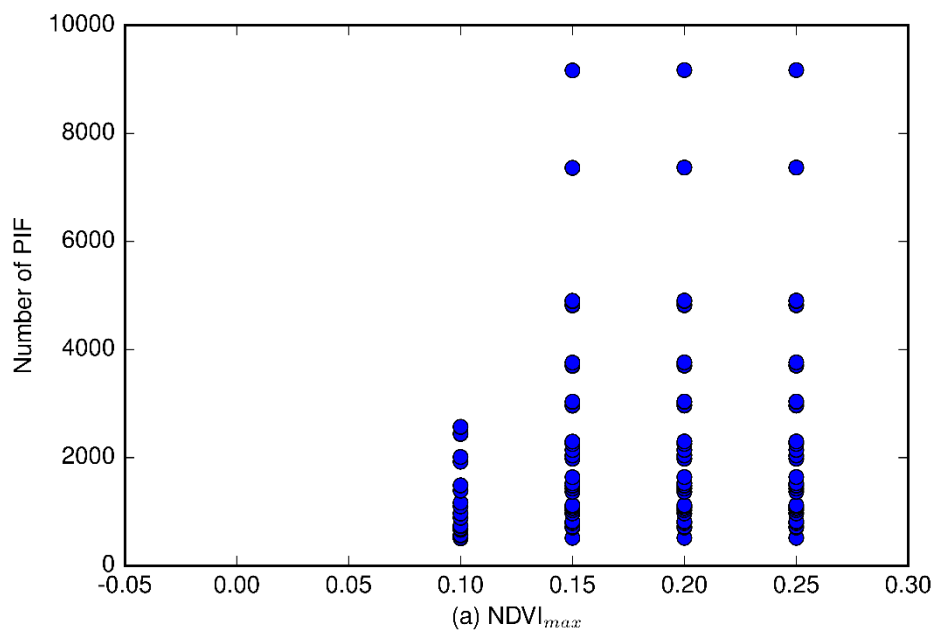


Figure 25 (a). Scatter plot $NDVI_{max}$ - number of PIF for the Egyptian study area.

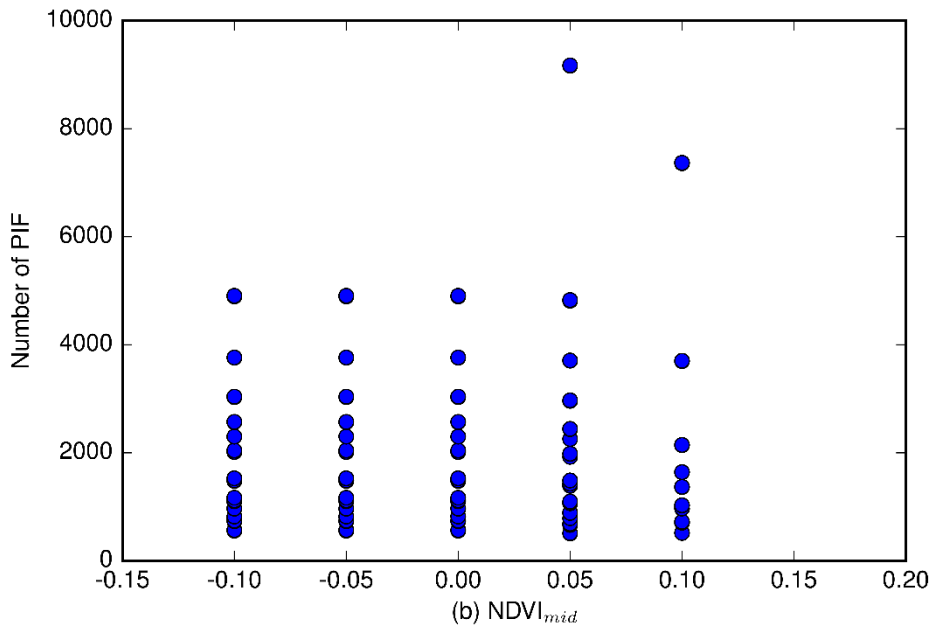


Figure 25 (b). Scatter plot $NDVI_{mid}$ - number of PIF for the Egyptian study area.

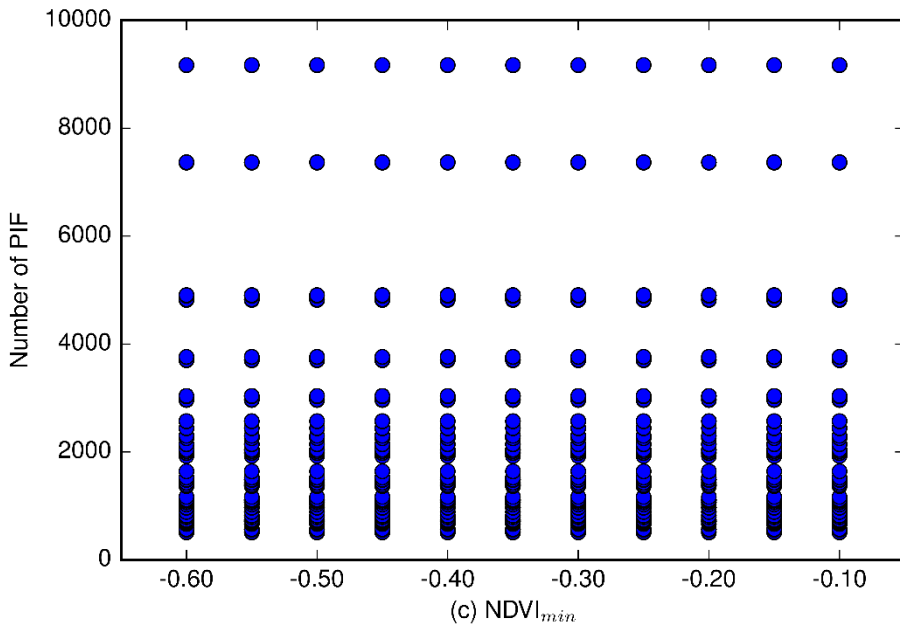


Figure 25 (c). Scatter plot $NDVI_{min}$ - number of PIF for the Egyptian study area.

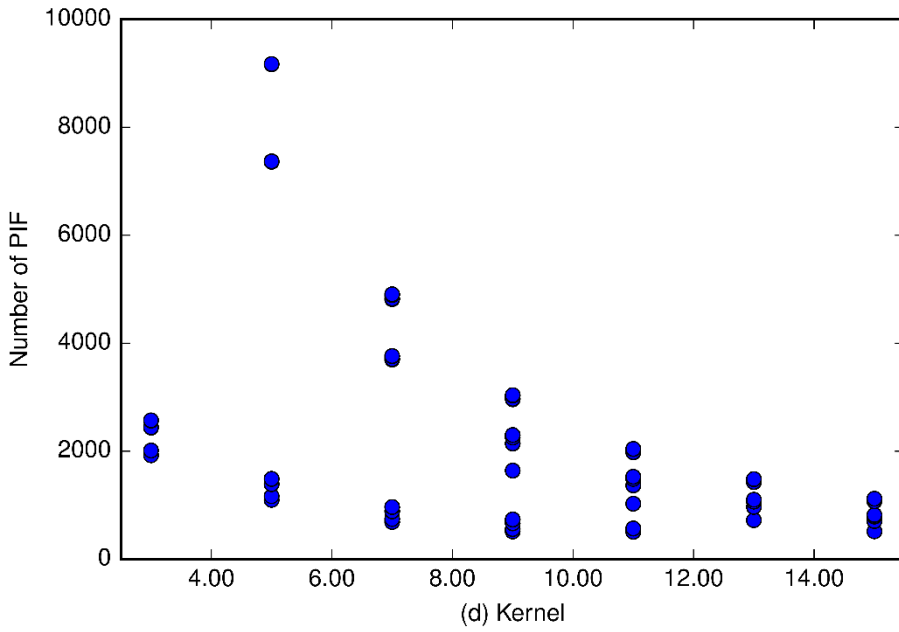


Figure 25 (d). Scatter plot Kernel - number of PIF for the Egyptian study area.

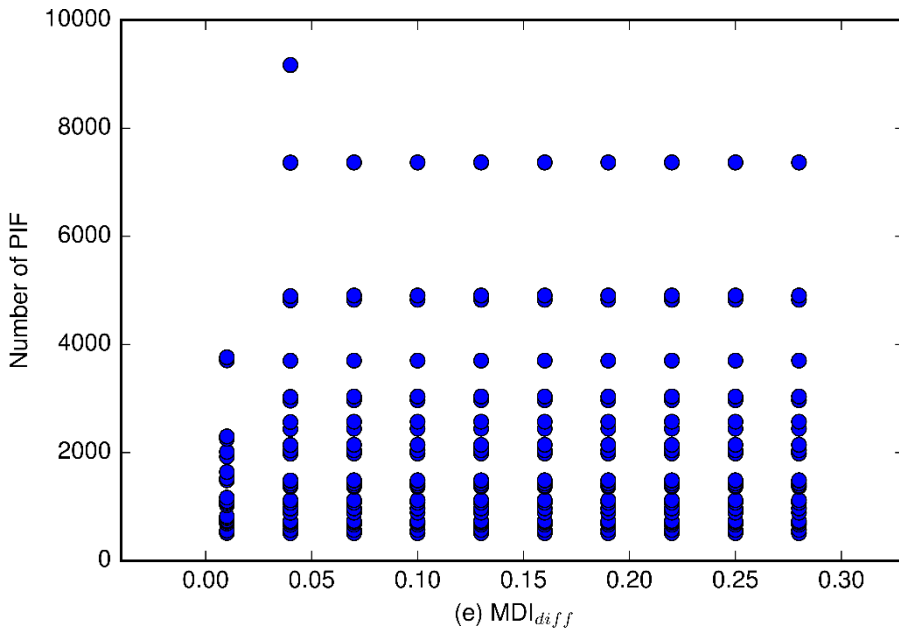


Figure 25 (e). Scatter plot MDI_{diff} - number of PIF for the Egyptian study area.

2.5.2 Comparisons with the IR-MAD algorithm

The well-known IR-MAD correction algorithm was used to test the performances of the proposed one. Since the proposed algorithm is dependent on user driven parameters more than the IR-MAD, the results showed in the previous section have been used to select one single test combination for each test area.

Test Area	NDVI _{max}	NDVI _{mid}	NDVI _{min}	MDI _{diff}	Kernel size
I	0.250	0.069	-0.205	0.040	3
N	0.210	0.000	-0.250	0.056	3
S	0.221	0.100	-0.503	0.030	7
E	0.189	0.006	-0.475	0.088	9

Table 17. Implemented thresholds and kernel size for the selected Italian (I), Nepalese (N), Spanish (S) and Egyptian (E) test areas. These parameters were the input of the proposed method implemented in the comparisons with the IR-MAD algorithm.

Each combination was randomly extracted from HQ-PIF test parameter intervals characterized by a high frequency of occurrence and removing the restriction adopted during the test phase to save computation time (i.e. the step showed in *Table 14*). The choice to consider only one random set of parameters was driven by the evidences showed in the previous scatterplots. Indeed, each single HQ-PIF extraction respects the conditions listed in the initial part of paragraph 2.5.1.

Table 17 shows the thresholds and the Kernel sizes, randomly selected, implemented in each study area with the TRRCA for comparison purposes with the IR-MAD algorithm.

For the IR-MAD algorithm, two different no-change probabilities (0.99 and 0.95) were tested. With the smaller one, the IR-MAD was able to find more PIF (*Table 18*) since a lower no-change probability increases the number of suitable PIF. However, their quality (e.g. correlations, and statistical tests) was lower than the one obtained with a no-change probability equal to 0.99. For this reason, only these IR-MAD results are shown and used for the performed comparisons.

All the combinations showed in *Table 17* performed a successful HQ-PIF extraction for the related test areas. *Table 18* compares the number of found PIF achieved for the all the test areas with the two different methods.

Test Area	No. of PIF TRRCA	No. of PIF IR-MAD 99%	No. of PIF IR-MAD 95%
I	907	561	2737
N	1141	713	2424
S	893	412	1703
E	3038	530	2918

Table 18. Number of TRRCA HQ-PIF for the selected Italian (I), Nepalese (N), Spanish (S) and Egyptian (E) test areas compared with IR-MAD number of PIF at 99% and 95% of no-change probability.

Table 18 shows that the random set of chosen parameters was coupled to a number of selected PIF greater than the IR-MAD at 99% of no-change probability but smaller, except for Egyptian study area, than the IR-MAD at 95% of no-change probability.

Figure 26 compares RGB visualizations of a magnified area of reference and corrected target with overlapped TRRCA HQ-PIF. All the test areas acquisition dates were shifted by at least one year (Table 12) to avoid too many similarities between reference and target images.

In Figure 26 a) is shown a subset of the heterogeneous Italian test area as representative of the whole Italian subset. Figure 26 a) clearly shows HQ-PIF falling within the sea, salt plains (in light brown), built-up areas, post-harvesting cultivated area and bare soil. The chosen subset purposely shows a portion of built-up areas (a small percentage of the whole Italian test area) with a high PIF density.

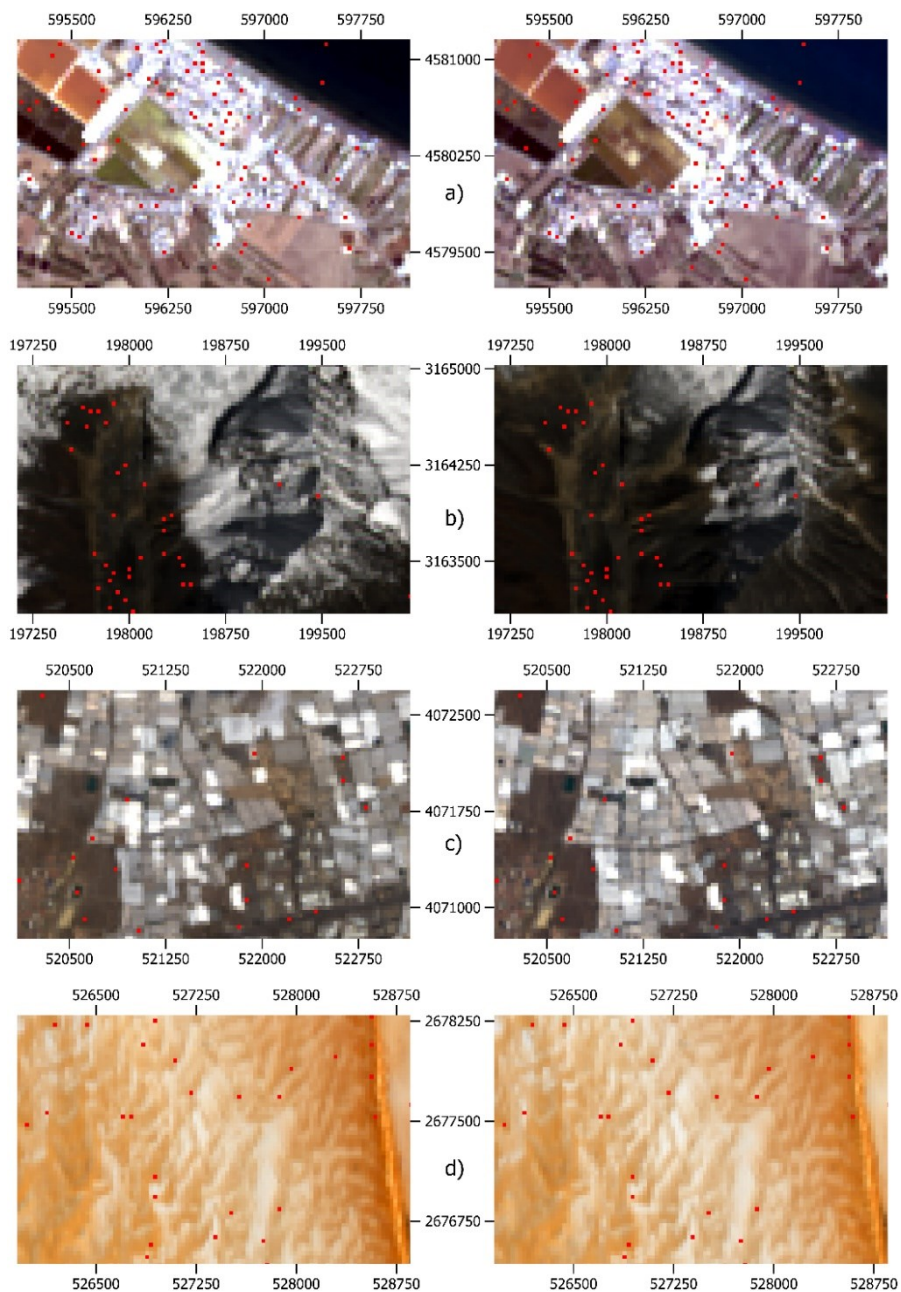


Figure 26. Comparison of RGB visualizations of Reference (R) image (on the left) and corrected Target (T) image (on the right) with overlapped PIF. a) Italian test area (I) (Coordinate System UTM WGS 84 zone 33N); b) Nepalese (N) test area (Coordinate System UTM WGS 84 zone 45N); c) Spanish (S) test area (Coordinate System UTM WGS 84 zone 30N); d) Egyptian (E) test area (Coordinate System UTM WGS 84 zone 35N).

The PIF selection was able to recognize as PIF pixels falling over very different land covers. Particularly, Figure 26 a) shows a higher density of PIF in built-up areas (bright areas). In Figure 26 b) is shown a subset of the Nepalese test area. In this subset, there is a clear difference in snow/ice covered areas and thus selected PIF generally falls over areas not covered by permanent snow/ice. These areas are characterized by low NDVI and are near to watersheds. Figure 26 c) shows a subset of the Spanish test area. In the Spanish test area, the major part of the PIF falls within artificial pools, bare soil, built-up areas and highways. Although the large amount of plastic covered greenhouses, PIF do not fall within them. Indeed, greenhouses are generally covered by plastic sheets characterized by different spectral signatures over time. This is mainly due to their different spectral properties, thickness and local agricultural practices (Novelli and Tarantino, 2015a). In Figure 26 d) is shown a portion of the Egyptian test area. The two areas feature a very similar visual landscape and this is confirmed also by the large amount of found PIF (see Table 18). Indeed, this was expected since similar results were achieved in the Canty and Nielsen (2008) work with desert/arid test areas.

Table 19, Table 20, Table 21 and Table 22 compare the achieved gains, offsets, correlation coefficient (r), RMSE, two-sample t-test, two-sample F-test and two-sample Wilcoxon rank sum test results between the TRRCA and the IR-MAD for the four test areas. Moreover, the different statistical test results achieved before (Pre) and after (Post) the correction are shown for the TRRCA method. They show that the TRRCA was able to find PIF with a strong linear agreement in each test area. The IR-MAD equally performs good results although, especially in the S area, shows some localized errors. For each computed gain of the TRRCA the significance of the linear relationship was tested against the null hypothesis of absence of slope. All tests strongly rejected the null hypothesis. It is thus possible to conclude that the method produces a feasible linear regression model. Considering the evaluated RMSE and r , the TRRCA always shows high quality and stable results (small variance).

The same cannot be said for the IR-MAD, in which the RMSE values are characterized by a stronger variability and greater values than TRRCA. With regard to the r values, the IR-MAD features mean r values greater than the TRRCA in the Egyptian and in the Nepalese areas, smaller than the TRRCA in the Spanish area and comparable values in the Italian test area. Particularly, the IR-MAD algorithm performed the worst results in the

Spanish test area (see Table 21), probably because of the large amount of plastic covered areas, whereas the Egyptian test area features the best achieved results (see Table 22). For the Spanish area, the error was mainly focused in the green band (band 3) and occurred also with 0.95 % of no-change probability.

Lastly, the showed tables depict also the results of statistical tests performed over the selected PIF. After the application of the correction with the TRRCA all the performed tests failed to reject the null hypothesis. Moreover, p-values indicate that all the null hypothesis would be accepted by using a level of confidence far beyond the default one. Considering each typology of test, this respectively indicates a strong statistical similarity between the variance, the means and medians of the reflectance values of test PIF extracted from the reference and corresponding normalized reflectance values of PIF extracted from the target. This was an expected result since the definition of HQ-PIF imposes the respect of all statistical tests. For all the test areas, the effects of the corrections were bigger on the median of the distributions of the selected PIF. This is demonstrated by the pre/post Wilcoxon rank sum test. The performed corrections show their influence also on the variances and the mean values of the extracted PIF. The effect over the variances is quite important on the Spanish and the Egyptian test areas whereas the improvement over the mean values occurred for at least two bands in each test area (with a peak of four bands in the S and the E areas).

The results achieved with the IR-MAD showed that all the two sample t-tests, for all the test areas, failed to reject the null hypothesis. Only the S test area featured a rejection of the null hypothesis with the regard to two sample F-test. The respect of the Wilcoxon rank sum test was the most restrictive one for the IR-MAD. Indeed, in the Nepalese test area four bands, associated to the extracted PIF, rejected the null hypothesis. Only for the Egyptian test area were satisfied all the tested null hypothesis. And this confirms the good performance of the IR-MAD over arid and natural areas.

TRRCA																
Band	gains	offsets	r	RMSE	F p-value		F h		t p-value		t h		W p-value		W h	
					Pre	Post	Pre	Post	Pre	Post	Pre	Post	Pre	Post	Pre	Post
1	1.044	-0.004	0.964	0.009	0.21	0.96	0	0	0.02	1.00	1	0	0.00	0.64	1	0
2	1.059	-0.006	0.963	0.012	0.10	0.95	0	0	0.03	1.00	1	0	0.00	0.59	1	0
3	1.111	-0.013	0.956	0.020	0.00	0.89	1	0	0.02	1.00	1	0	0.00	0.68	1	0
4	1.081	-0.005	0.964	0.025	0.02	0.93	1	0	0.01	1.00	1	0	0.00	0.37	1	0
5	1.022	0.003	0.980	0.028	0.52	0.99	0	0	0.18	1.00	0	0	0.00	0.15	1	0
6	1.053	-0.008	0.968	0.040	0.14	0.96	0	0	0.29	1.00	0	0	0.00	0.40	1	0
7	1.067	-0.004	0.972	0.030	0.06	0.96	0	0	0.05	1.00	0	0	0.00	0.59	1	0

IR-MAD												
Band	gains	Offsets	R	RMSE	F p-value		F h	t p-value		t h	W p-value	W h
1	0.940	0.018	0.894	0.019	0.74		0	0.83		0	0.08	0
2	0.930	0.017	0.907	0.026	0.76		0	0.85		0	0.04	1
3	0.821	0.025	0.973	0.067	0.92		0	0.99		0	0.94	0
4	0.917	0.013	0.995	0.315	0.97		0	0.99		0	0.33	0
5	0.952	0.011	0.999	3.219	0.99		0	0.99		0	0.12	0
6	0.966	0.001	0.997	1.220	0.96		0	0.98		0	0.11	0
7	0.983	-0.001	0.997	0.791	0.95		0	0.99		0	0.09	0

Table 19. Italian (I) test area: Evaluated band-by-band gain, offset, correlation r and RMSE. F p-value, t p-value, W p-value are p-values for the two sample F test, two sample t test and the Wilcoxon rank sum test. The result h = 1 indicates a rejection of the null hypothesis, and h = 0 indicates a failure to reject the null hypothesis at the 5% significance level.

TRRCA																
Band	Gains	offsets	r	RMSE	F p-value		F h		t p-value		t h		W p-value		W h	
					Pre	Post	Pre	Post	Pre	Post	Pre	Post	Pre	Post	Pre	Post
1	0.993	0.010	0.988	0.010	0.82	1.00	0	0	0.00	1.00	1	0	0.00	0.21	1	0
2	0.973	0.010	0.984	0.011	0.37	0.99	0	0	0.02	1.00	1	0	0.00	0.35	1	0
3	1.010	0.002	0.983	0.014	0.73	1.00	0	0	0.31	1.00	0	0	0.00	0.35	1	0
4	0.981	0.003	0.979	0.017	0.52	0.99	0	0	0.99	1.00	0	0	0.02	0.14	1	0
5	0.986	-0.001	0.978	0.018	0.65	0.99	0	0	0.38	1.00	0	0	0.00	0.11	1	0
6	1.024	-0.006	0.967	0.023	0.44	0.98	0	0	0.56	1.00	0	0	0.00	0.53	1	0
7	1.001	-0.003	0.965	0.021	0.99	1.00	0	0	0.46	1.00	0	0	0.00	0.13	1	0
IR-MAD																
Band	Gains	offsets	r	RMSE	F p-value		F h		t p-value		t h		W p-value		W h	
1	1.446	-0.026	0.997	0.598	0.92		0		0.97		0		0.20		0	
2	1.458	-0.021	0.995	0.481	0.90		0		0.96		0		0.03		1	
3	1.458	-0.013	0.989	0.274	0.85		0		0.97		0		0.00		1	
4	1.440	-0.008	0.986	0.229	0.80		0		0.96		0		0.00		1	
5	1.008	-0.002	0.949	0.128	0.65		0		0.99		0		0.00		1	
6	1.021	-0.000	0.995	0.290	0.88		0		0.97		0		0.77		0	
7	1.050	0.000	0.992	0.158	0.91		0		0.97		0		0.76		0	

Table 20. Nepalese (N) test area: Evaluated band-by-band gain, offset, correlation r and RMSE; F p-value, t p-value, W p-value are p-values for the two sample F test, two sample t test and the Wilcoxon rank sum test. The result h = 1 indicates a rejection of the null hypothesis, and h = 0 indicates a failure to reject the null hypothesis at the 5% significance level.

TRRCA																
Band	gains	offsets	r	RMSE	F p-value		F h		t p-value		t h		W p-value		W h	
					Pre	Post	Pre	Post	Pre	Post	Pre	Post	Pre	Post	Pre	Post
1	1.0761	-0.006	0.963	0.007	0.03	0.94	1	0	0.00	1.00	1	0	0.00	0.83	1	0
2	1.0625	-0.006	0.965	0.008	0.08	0.95	0	0	0.00	1.00	1	0	0.00	0.74	1	0
3	1.0806	-0.013	0.963	0.010	0.03	0.93	1	0	0.66	1.00	0	0	0.04	0.34	1	0
4	1.1158	-0.023	0.960	0.013	0.00	0.90	1	0	0.75	1.00	0	0	0.03	0.37	1	0
5	1.1895	-0.051	0.945	0.020	0.00	0.78	1	0	0.70	1.00	0	0	0.70	0.51	0	0
6	1.2720	-0.066	0.956	0.021	0.00	0.76	1	0	0.00	1.00	1	0	0.00	0.67	1	0
7	1.2547	-0.045	0.961	0.017	0.00	0.79	1	0	0.00	1.00	1	0	0.00	0.52	1	0

IR-MAD											
Band	gains	Offsets	r	RMSE	F p-value	F h	t p-value	t h	W p-value	W h	
1	0.1575	0.109	0.435	0.002	0.00	1	0.67	0	0.64	0	
2	-0.1083	0.126	-0.173	0.001	0.00	1	0.58	0	0.00	1	
3	39.0422	-4.451	0.056	0.245	0.00	1	0.56	0	0.29	0	
4	3.6598	-0.314	0.833	0.058	0.00	1	0.90	0	0.22	0	
5	1.6055	-0.124	0.998	1.069	0.98	0	0.98	0	0.67	0	
6	1.5515	-0.104	0.998	1.100	0.96	0	0.99	0	0.22	0	
7	1.6448	-0.089	0.995	0.471	0.90	0	1.00	0	0.00	1	

Table 21. Spanish (S) test area: Evaluated band-by-band gain, offset, correlation r and RMSE; F p-value, t p-value, W p-value are p-values for the two sample F test, two sample t test and the Wilcoxon rank sum test. The result h = 1 indicates a rejection of the null hypothesis, and h = 0 indicates a failure to reject the null hypothesis at the 5% significance level.

TRRCA																
Band	gains	offsets	r	RMSE	F p-value		F h		t p-value		t h		W p-value		W h	
					Pre	Post	Pre	Post	Pre	Post	Pre	Post	Pre	Post	Pre	Post
1	0.872	0.026	0.984	0.002	0.00	0.90	1	0	0.00	1.00	1	0	0.00	0.62	1	0
2	0.885	0.024	0.988	0.003	0.00	0.93	1	0	0.00	1.00	1	0	0.00	0.57	1	0
3	0.914	0.023	0.994	0.004	0.00	0.98	1	0	0.74	1.00	0	0	0.00	0.39	1	0
4	0.940	0.024	0.995	0.007	0.00	0.99	1	0	0.90	1.00	0	0	0.00	0.61	1	0
5	0.956	0.023	0.995	0.010	0.01	0.99	1	0	0.69	1.00	0	0	0.06	0.60	0	0
6	0.958	0.029	0.994	0.010	0.02	0.99	1	0	0.16	1.00	0	0	0.00	0.27	1	0
7	0.972	0.021	0.994	0.009	0.13	0.99	0	0	0.00	1.00	1	0	0.00	0.15	1	0
IR-MAD																
Band	Gains	offsets	r	RMSE	F p-value		F h		t p-value		t h		W p-value		W h	
1	0.927	0.015	0.998	0.160	0.93		0		0.99		0		0.94		0	
2	0.928	0.015	0.998	0.204	0.93		0		0.99		0		0.93		0	
3	0.929	0.018	0.999	0.323	0.96		0		1.00		0		0.94		0	
4	0.942	0.023	0.999	0.474	0.98		0		0.99		0		0.98		0	
5	0.954	0.023	0.999	0.618	0.97		0		1.00		0		0.98		0	
6	0.965	0.023	0.998	0.341	0.99		0		0.99		0		0.97		0	
7	0.970	0.022	0.999	0.443	0.97		0		1.00		0		0.96		0	

Table 22. Egyptian (E) test area: Evaluated band-by-band gain, offset, correlation r and RMSE; F p-value, t p-value, W p-value are p-values for the two sample F test, two sample t test and the Wilcoxon rank sum test. The result h = 1 indicates a rejection of the null hypothesis, and h = 0 indicates a failure to reject the null hypothesis at the 5% significance level.

ACKNOWLEDGEMENTS Chapter 2

The Ph.D. candidate is thankful to Prof. M.A. Aguilar and Doc. Benedetto Figorito for their suggestions related to chapter two.

References of Chapter 2

- AGUILAR, M. A., NEMMAOUI, A., NOVELLI, A., AGUILAR, F. J. & GARCÍA LORCA, A. 2016. Object-Based Greenhouse Mapping Using Very High Resolution Satellite Data and Landsat 8 Time Series. *Remote Sensing*, 8, 513.
- BAO, N., LECHNER, A., FLETCHER, A., MELLOR, A., MULLIGAN, D. & BAI, Z. 2012. Comparison of relative radiometric normalisation methods using pseudo-invariant features for change detection studies in rural and urban landscapes. *Journal of Applied Remote Sensing*, 6, 1-18.
- BIDAY, S. G. & BHOSLE, U. 2010. Radiometric correction of multitemporal satellite imagery. *Journal of Computer Science*, 6, 1027.
- BOGGS, P. T., BYRD, R. H. & SCHNABEL, R. B. 1987. A stable and efficient algorithm for nonlinear orthogonal distance regression. *SIAM Journal on Scientific and Statistical Computing*, 8, 1052-1078.
- BROWN, P. J. & FULLER, W. A. 1990. *Statistical Analysis of Measurement Error Models and Applications: Proceedings of the AMS-IMS-SIAM Joint Summer Research Conference Held June 10-16, 1989, with Support from the National Science Foundation and the US Army Research Office*, American Mathematical Soc.
- CANTY, M. J. & NIELSEN, A. A. 2008. Automatic radiometric normalization of multitemporal satellite imagery with the iteratively re-weighted MAD transformation. *Remote Sensing of Environment*, 112, 1025-1036.
- CANTY, M. J. & NIELSEN, A. A. 2012. Linear and kernel methods for multivariate change detection. *Computers & Geosciences*, 38, 107-114.

- CANTY, M. J., NIELSEN, A. A. & SCHMIDT, M. 2004. Automatic radiometric normalization of multitemporal satellite imagery. *Remote Sensing of Environment*, 91, 441-451.
- CAPOBIANCO, R. & PICUNO, P. Remote sensing and thematic mapping of protected cultivation in Southern Italy agricultural landscapes. Agricultural and biosystems engineering for a sustainable world. International Conference on Agricultural Engineering, Hersonissos, Crete, Greece, 23-25 June, 2008, 2008. European Society of Agricultural Engineers (AgEng), OP-1160.
- CAPRIOLI, M., FIGORITO, B. & TARANTINO, E. Radiometric Normalization of Landsat Etm+ data for Multitemporal Analysis. Proceedings of ISPRS Commission VII Mid-Term Symposium on "Remote Sensing: from Pixels to Processes", Enschede (unpaginated CD-ROM), 2006.
- CASELLES, V. & LOPEZ GARCIA, M. 1989. An alternative simple approach to estimate atmospheric correction in multitemporal studies. *International Journal of Remote Sensing*, 10, 1127-1134.
- CHAVEZ JR, P. S. 1988. An improved dark-object subtraction technique for atmospheric scattering correction of multispectral data. *Remote sensing of environment*, 24, 459-479.
- CHEN, X., VIERLING, L. & DEERING, D. 2005. A simple and effective radiometric correction method to improve landscape change detection across sensors and across time. *Remote Sensing of Environment*, 98, 63-79.
- COPPIN, P. R. & BAUER, M. E. 1996. Digital change detection in forest ecosystems with remote sensing imagery. *Remote sensing reviews*, 13, 207-234.
- DE CARVALHO, O. A., GUIMARÃES, R. F., SILVA, N. C., GILLESPIE, A. R., GOMES, R. A. T., SILVA, C. R. & DE CARVALHO, A. P. F. 2013. Radiometric Normalization of Temporal Images Combining Automatic Detection of Pseudo-Invariant Features from the Distance and Similarity Spectral Measures, Density Scatterplot Analysis, and Robust Regression. *Remote Sensing*, 5, 2763-2794.
- DU, Y., TEILLET, P. M. & CIHLAR, J. 2002. Radiometric normalization of multitemporal high-resolution satellite images with quality control for land cover change detection. *Remote Sensing of Environment*, 82, 123-134.
- ECKHARDT, D., VERDIN, J. & LYFORD, G. 1990. Automated update of an irrigated lands GIS using SPOT HRV imagery. *Photogrammetric Engineering and Remote Sensing*, 56, 1515-1522.
- EIVAZI, A., KOLESNIKOV, A., JUNTILA, V. & KAURANNE, T. 2015. Variance-preserving mosaicing of multiple satellite images for forest parameter estimation: Radiometric normalization. *ISPRS Journal of Photogrammetry and Remote Sensing*, 105, 120-127.
- EL HAJJ, M., BÉGUÉ, A., LAFRANCE, B., HAGOLLE, O., DEDIEU, G. & RUMEAU, M. 2008. Relative radiometric normalization and atmospheric correction of a SPOT 5 time series. *Sensors*, 8, 2774-2791.

- ELVIDGE, C. D., YUAN, D., WEERACKOON, R. D. & LUNETTA, R. S. 1995. Relative radiometric normalization of Landsat Multispectral Scanner (MSS) data using a automatic scattergram-controlled regression. *Photogrammetric Engineering and Remote Sensing*, 61, 1255-1260.
- FERNANDES, R. & LEBLANC, S. G. 2005. Parametric (modified least squares) and non-parametric (Theil–Sen) linear regressions for predicting biophysical parameters in the presence of measurement errors. *Remote Sensing of Environment*, 95, 303-316.
- FURBY, S. & CAMPBELL, N. 2001. Calibrating images from different dates to 'like-value'digital counts. *Remote Sensing of Environment*, 77, 186-196.
- GARCIA-TORRES, L., CABALLERO-NOVELLA, J. J., GOMEZ-CANDON, D. & DE-CASTRO, A. I. 2014. Semi-automatic normalization of multi-temporal remote images based on vegetative pseudo-Invariant Features. *PloS one*, 9, e91275.
- GIORDANO, R., D'AGOSTINO, D., APOLLONIO, C., SCARDIGNO, A., PAGANO, A., PORTOGHESE, I., LAMADDALENA, N., PICCINNI, A. F. & VURRO, M. 2015. Evaluating acceptability of groundwater protection measures under different agricultural policies. *Agricultural Water Management*, 147, 54-66.
- GONZALEZ, R. C. & WOODS, R. E. 2008. Digital image processing. Prentice hall Upper Saddle River, NJ, USA:.
- HADJIMITSIS, D. G., CLAYTON, C. & RETALIS, A. On the darkest pixel atmospheric correction algorithm: a revised procedure applied over satellite remotely sensed images intended for environmental applications. *Proc. of SPIE Vol*, 2003. 465.
- HALL, F. G., STREBEL, D. E., NICKESON, J. E. & GOETZ, S. J. 1991. Radiometric rectification: toward a common radiometric response among multidecade, multisensor images. *Remote Sensing of Environment*, 35, 11-27.
- HENEBRY, G. M. & SU, H. 1993. Using landscape trajectories to assess the effects of radiometric rectification. *International Journal of Remote Sensing*, 14, 2417-2423.
- HEO, J. & FITZHUGH, T. W. 2000. A standardized radiometric normalization method for change detection using remotely sensed imagery. *Photogrammetric Engineering and Remote Sensing*, 66, 173-181.
- HONG, G. & ZHANG, Y. 2008. A comparative study on radiometric normalization using high resolution satellite images. *International Journal of Remote Sensing*, 29, 425-438.
- HUETE, A. R. & LIU, H. Q. 1994. An error and sensitivity analysis of the atmospheric-and soil-correcting variants of the NDVI for the MODIS-EOS. *IEEE Transactions on Geoscience and Remote Sensing*, 32, 897-905.
- HURTADO, S., GARCÍA-LEÓN, M. & GARCÍA-TENORIO, R. 2006. A revision of energy and resolution calibration method of Ge detectors. *Nuclear Instruments and Methods in Physics Research Section A: Accelerators, Spectrometers, Detectors and Associated Equipment*, 564, 295-299.

- HUSSAIN, M., CHEN, D., CHENG, A., WEI, H. & STANLEY, D. 2013. Change detection from remotely sensed images: From pixel-based to object-based approaches. *ISPRS Journal of Photogrammetry and Remote Sensing*, 80, 91-106.
- JANZEN, D. T., FREDEEN, A. L. & WHEATE, R. D. 2006. Radiometric correction techniques and accuracy assessment for Landsat TM data in remote forested regions. *Canadian Journal of Remote Sensing*, 32, 330-340.
- JENSEN, J. 1996. Chapter 6:" Image Preprocessing: Radiometric and Geometric Correction,". *Introductory Digital Image Processing*. 30p.
- KIM, D. S., PYEON, M. W., EO, Y. D., BYUN, Y. G. & KIM, Y. I. 2012. Automatic pseudo-invariant feature extraction for the relative radiometric normalization of hyperion hyperspectral images. *GIScience & Remote Sensing*, 49, 755-773.
- KOUKAL, T., SUPPAN, F. & SCHNEIDER, W. 2007. The impact of relative radiometric calibration on the accuracy of kNN-predictions of forest attributes. *Remote Sensing of Environment*, 110, 431-437.
- LIN, C.-H., LIN, B.-Y., LEE, K.-Y. & CHEN, Y.-C. 2015. Radiometric normalization and cloud detection of optical satellite images using invariant pixels. *ISPRS Journal of Photogrammetry and Remote Sensing*, 106, 107-117.
- MARPU, P. R., GAMBA, P. & CANTY, M. J. 2011. Improving change detection results of IR-MAD by eliminating strong changes. *IEEE Geoscience and Remote Sensing Letters*, 8, 799-803.
- MICHENER, W. K. & HOUHOULIS, P. F. 1997. Detection of vegetation changes associated with extensive flooding in a forested ecosystem. *Photogrammetric Engineering and Remote Sensing*, 63, 1363-1374.
- MUSTAFIZUR RAHMAN, M., HAY, G. J., COULOIGNER, I., HEMACHANDRAN, B. & BAILIN, J. 2014. An Assessment of Polynomial Regression Techniques for the Relative Radiometric Normalization (RRN) of High-Resolution Multi-Temporal Airborne Thermal Infrared (TIR) Imagery. *Remote Sensing*, 6, 11810-11828.
- NIELSEN, A. A., CONRADSEN, K. & ANDERSEN, O. B. 2002. A change oriented extension of EOF analysis applied to the 1996–1997 AVHRR sea surface temperature data. *Physics and Chemistry of the Earth, Parts A/B/C*, 27, 1379-1386.
- NIELSEN, A. A., CONRADSEN, K. & SIMPSON, J. J. 1998. Multivariate alteration detection (MAD) and MAF postprocessing in multispectral, bitemporal image data: New approaches to change detection studies. *Remote Sensing of Environment*, 64, 1-19.
- NOVELLI, A., AGUILAR, M. A., NEMMAOUI, A., AGUILAR, F. J. & TARANTINO, E. 2016a. Performance evaluation of object based greenhouse detection from Sentinel-2 MSI and Landsat 8 OLI data: A case study from Almería (Spain). *International Journal of Applied Earth Observation and Geoinformation*, 52, 403-411.
- NOVELLI, A., CARADONNA, G. & TARANTINO, E. Evaluation of relative radiometric correction techniques on Landsat 8 OLI sensor data. Fourth International

- Conference on Remote Sensing and Geoinformation of the Environment, 2016b. International Society for Optics and Photonics, 968808-968808-9.
- NOVELLI, A. & TARANTINO, E. 2015. Combining ad hoc spectral indices based on LANDSAT-8 OLI/TIRS sensor data for the detection of plastic cover vineyard. *Remote Sensing Letters*, 6, 933-941.
- O'CONNELL, J., CONNOLLY, J., VERMOTE, E. F. & HOLDEN, N. M. 2013. Radiometric normalization for change detection in peatlands: a modified temporal invariant cluster approach. *International journal of remote sensing*, 34, 2905-2924.
- OLTHOF, I., POULIOT, D., FERNANDES, R. & LATIFOVIC, R. 2005. Landsat-7 ETM+ radiometric normalization comparison for northern mapping applications. *Remote Sensing of Environment*, 95, 388-398.
- PHILPOT, W. & ANSTY, T. 2013. Analytical Description of Pseudoinvariant Features. *Geoscience and Remote Sensing, IEEE Transactions on*, 51, 2016-2021.
- POLEMIO, M. & LONIGRO, T. 2013. Climate Variability and Landslide Occurrence in Apulia (Southern Italy). *Landslide Science and Practice*. Springer.
- RAHMAN, M., HAY, G., COULOIGNER, I., HEMACHANDRAN, B. & BAILIN, J. 2015. A comparison of four relative radiometric normalization (RRN) techniques for mosaicing H-res multi-temporal thermal infrared (TIR) flight-lines of a complex urban scene. *ISPRS Journal of Photogrammetry and Remote Sensing*, 106, 82-94.
- ROY, D., WULDER, M., LOVELAND, T., CE, W., ALLEN, R., ANDERSON, M., HELDER, D., IRONS, J., JOHNSON, D. & KENNEDY, R. 2014. Landsat-8: Science and product vision for terrestrial global change research. *Remote Sensing of Environment*, 145, 154-172.
- ROY, D. P., BORAK, J. S., DEVADIGA, S., WOLFE, R. E., ZHENG, M. & DESCLOITRES, J. 2002. The MODIS land product quality assessment approach. *Remote Sensing of Environment*, 83, 62-76.
- SADEGHI, V., EBADI, H. & AHMADI, F. F. 2013. A new model for automatic normalization of multitemporal satellite images using Artificial Neural Network and mathematical methods. *Applied Mathematical Modelling*, 37, 6437-6445.
- SALAS, E. A. L., BOYKIN, K. G. & VALDEZ, R. 2016. Multispectral and Texture Feature Application in Image-Object Analysis of Summer Vegetation in Eastern Tajikistan Pamirs. *Remote Sensing*, 8, 78.
- SALAS, E. A. L. & HENEGBRY, G. M. 2012. Separability of maize and soybean in the spectral regions of chlorophyll and carotenoids using the Moment Distance Index. *Israel Journal of Plant Sciences*, 60, 65-76.
- SALAS, E. A. L. & HENEGBRY, G. M. 2013. A new approach for the analysis of hyperspectral data: Theory and sensitivity analysis of the Moment Distance Method. *Remote Sensing*, 6, 20-41.

- SCHEIDT, S., RAMSEY, M. & LANCASTER, N. 2008. Radiometric normalization and image mosaic generation of ASTER thermal infrared data: An application to extensive sand sheets and dune fields. *Remote Sensing of Environment*, 112, 920-933.
- SCHOTT, J. R. S., C VOLCHOK, W J 1989. Radiometric scene normalization using pseudo invariant features. *Remote Sensing of Environment*, 26, 1-16.
- SCHROEDER, T. A., COHEN, W. B., SONG, C., CANTY, M. J. & YANG, Z. 2006. Radiometric correction of multi-temporal Landsat data for characterization of early successional forest patterns in western Oregon. *Remote Sensing of Environment*, 103, 16-26.
- SONG, C., WOODCOCK, C. E., SETO, K. C., LENNEY, M. P. & MACOMBER, S. A. 2001. Classification and change detection using Landsat TM data: when and how to correct atmospheric effects? *Remote sensing of Environment*, 75, 230-244.
- SYKAS, D., KARATHANASSI, V. & KOLOKOUSSIS, P. 2013. Development of a New Automatic Relative Radiometric Normalization Methodology for Multispectral and Hyperspectral Images. *Journal of Remote Sensing*, 1, 75-83.
- TAN, K. C., SAN LIM, H., MATJAFRI, M. Z. & ABDULLAH, K. 2012. A comparison of radiometric correction techniques in the evaluation of the relationship between LST and NDVI in Landsat imagery. *Environmental monitoring and assessment*, 184, 3813-3829.
- TOKOLA, T., LÖFMAN, S. & ERKKILÄ, A. 1999. Relative calibration of multitemporal Landsat data for forest cover change detection. *Remote Sensing of Environment*, 68, 1-11.
- TUCKER, C. J. 1979. Red and photographic infrared linear combinations for monitoring vegetation. *Remote sensing of Environment*, 8, 127-150.
- VAN DER WALT, S., COLBERT, S. C. & VAROQUAUX, G. 2011. The NumPy array: a structure for efficient numerical computation. *Computing in Science & Engineering*, 13, 22-30.
- WULDER, M. A., WHITE, J. C., LOVELAND, T. R., WOODCOCK, C. E., BELWARD, A. S., COHEN, W. B., FOSNIGHT, E. A., SHAW, J., MASEK, J. G. & ROY, D. P. 2015. The global Landsat archive: Status, consolidation, and direction. *Remote Sensing of Environment*.
- XU, Q., HOU, Z. & TOKOLA, T. 2012. Relative radiometric correction of multi-temporal ALOS AVNIR-2 data for the estimation of forest attributes. *ISPRS Journal of Photogrammetry and Remote Sensing*, 68, 69-78.
- YANG, X. & LO, C. 2000. Relative radiometric normalization performance for change detection from multi-date satellite images. *Photogrammetric Engineering and Remote Sensing*, 66, 967-980.
- YUAN, D. & ELVIDGE, C. D. 1996. Comparison of relative radiometric normalization techniques. *ISPRS Journal of Photogrammetry and Remote Sensing*, 51, 117-126.

Conclusions

In this Ph.D. thesis was examined the topic of the enhancement of the pre-processing phase of passive remote sensing imagery. This topic was developed in two different ways: a specific application for Plastic Covered Greenhouse areas, and a general approach related to the development of a new algorithm for Relative Radiometric Correction.

The former and more specific topic was developed both with a pixel-based approach and with an OBIA approach. Considering the pixel-based approach, the Landsat 8 OLI and TIRS sensor data were conjunctly used for agricultural plastic cover detection, testing four normalized difference indices. The procedure benefitted from the use of information gathered through the Quality Assessment and Cloud Quality bands. Specifically, this is the first work that exploited the Landsat 8 Quality Assessment band for plastic covered greenhouse detection. The use of Cloud Quality bands reduced sampling time and improved the collection of spectral information related to plastic surfaces. The overall accuracies observed were on average higher than 80%. Moreover, the low cost of the used open dataset, lacking ancillary data, demonstrated the reliability of the proposed method, proving its suitability for pilot environmental and agricultural monitoring over large areas.

Better results were achieved through OBIA approach. To the best knowledge of the Ph.D. candidate, the proposed OBIA study was the first regarding plastic covered greenhouses detection comparing Sentinel-2 and Landsat-8 satellite data by applying an OBIA approach and RF classifier. The high geometric contribution of WorldView-2 based segmentation was employed to test the effectiveness of Sentinel-2 and Landsat 8 starting from a common and very good segmented image dataset. The accuracy values achieved using very small training sets were very high for both sensors, also thanks to the modified Euclidean Distance 2 index used to quantitatively assess the reliability of the best estimated segmentations. This can be considered a further confirmation of the relevant contribution of the segmentation process in the final plastic covered greenhouse detection. In this sense, another finding of this work was related to prove that Blue, Green and NIR bands are strongly related to the best segmentation of greenhouses for atmospherically corrected

Sentinel-2, Landsat-8 and WorldView-2 data. Future research can benefit from this information to save computation time. Overall, the results showed that Sentinel-2 performed better than Landsat-8, particularly when the best common segmentation from WorldView-2 was used for both satellites.

The capabilities of the command line tool AssesSeg, created and used in this thesis to assess the accuracy of the performed segmentations were also described. Particularly this command line tool is user-friendly and available both for scientific and technical purposes. The use of the very popular ESRI shapefiles data format makes AssesSeg widely compatible with the outputs of the most common OBIA software. Thanks to AssesSeg, were found: (I) the above mentioned optimal bands combination; (II) the ideal parameters setting headed up to carry out an optimal plastic covered greenhouses areas segmentation by using the well-known multiresolution segmentation algorithm included within eCognition. Lastly, the use of the tool also pointed out to the importance of increasing the number of reference objects to diminish the uncertainty in assessing the segmentation quality through the Euclidean Distance 2 modified metrics.

With regard the first chapter, the accuracy of the results obtained in this study makes this OBIA approach highly recommended for plastic covered greenhouses mapping and detection. Further research will be focused both on the definition of new and more performant segmentation quality metrics and in the assessment of the best Sentinel-2 and Landsat-8 features. Although the procedure and tools showed in this chapter are related to plastic greenhouse extraction, the achieved results and the showed methods can be considered valid also in other environments that can benefit from optimized segmentation parameters (e.g. object detection by means OBIA).

The second topic was related to the enhancement of the pre-processing for passive remotely sensed data. Particularly, was shown a new PIF selecting algorithm combining spectral momentum measures, NDVI masks and extraction of local maximum and minimum through morphological operators. The method was tested with Landsat-8 images but its design is suitable for other passive sensors with a similar spectral resolution (e.g. Sentinel-2).

Due to its dependence by user driven thresholds, many combinations were tested over four different study areas around the world. Particularly the chosen study areas were extremely different and characterized by high heterogeneity between reference and target

scenes (Italian test area), by the presence of an extreme anthropic impact (Spanish area with its plastic covered greenhouses) and by a low anthropic impact over different natural climatic conditions (Egyptian and Nepalese test area). All the test performed were driven to obtain the distribution of thresholds able to perform a good relative radiometric normalization.

The method was also compared with the well-known IR-MAD algorithm by selecting randomly a set of parameters for each study area. In this case, the proposed algorithm recognized a great number of PIF for each selected area and performed a correction on the selected PIF able to eliminate statistical differences between reference PIF and corrected target PIF. From this point of view, the TRRCA performed better than the IR-MAD. Moreover, thanks to the orthogonal distance regression, the algorithm performed better than the IR-MAD also with regard the RMSE associated to the regressions.

To the Ph.D. candidate opinion, the showed results confirm the effectiveness of the method as new relative radiometric normalization technique and as a valid alternative to established methods from the scientific literature. Future development will be focused on the improvement of the quality of selected PIF, on the analysis of a greater spectral range and in an improved reduction of user driven parameter.

European curriculum vitae format



PERSONAL INFORMATION

Name	ANTONIO NOVELLI
Address	VIA RENATO GUTTUSO 2, RIGNANO GARGANICO (FG) 71010, ITALY
Cell phone	0039 3408236442
E-mail	antonio.novelli@poliba.it, antonio.novelli87@gmail.com
Nationality	Italian

EDUCATION AND TRAINING (POST MASTER DEGREE)

date	January 2014 - Present
Occupation or Position held	PHD STUDENT. PHD SCHOOL - RISK AND ENVIRONMENTAL, TERRITORIAL AND BUILDING DEVELOPMENT
Name and Type of Organisation	Politecnico di BARI - Via Amendola, 126/B – BARI, ITALY Department of Civil, Environmental, Territory planning, Construction Engineering and Chemistry (DICATECh)

SCIENTIFIC AWARDS

Date	16 - 19 March 2015
Occupation or Position held	Ph.D. student
Award	BEST POSTER AWARD Tarantino E., Novelli A. , Laterza M., Gioia A. (2015). Testing high spatial resolution WorldView-2 imagery for retrieving the leaf area index. In: Third International Conference on Remote Sensing and Geoinformation of the Environment (RSCy2015). Cyprus, doi:10.1117/12.2192561

PATENT AND INTELLECTUAL PROPERTY

Typology	Pending request of Intellectual property (Spain)
Autor's	M. A. Aguilar, Tarantino E., Novelli A. , F. J. Aguilar
Description	Programa con objetivo evaluar la calidad de la segmentacion en entornos OBIA (software for the evaluation of the quality of the segmentation of digital images)
Programming Language	Python 2.7
Reference number (Andalusian Government)	AL-109-16
Name	AssesSeg

REVIEW ACTIVITY FOR INTERNATIONAL JOURNALS

iForest - Biogeosciences and Forestry (2015) – online ISSN: 1971-7458
European Journal of Remote Sensing (2016) -- online ISSN: 2279-7254
International Journal of Remote Sensing (2016) – online ISSN: 1366-5901
Journal of Forest Research (2016) – online ISSN: 1610-7403
Remote Sensing (2016) -- online ISSN: 2072-4292
Sensors (2016) -- online ISSN: 1424-8220
Algorithms (2016) -- online ISSN: 1999-4893
ISPRS Journal of Photogrammetry and Remote Sensing (2016-2017) -- online ISSN: 0924-2716

PARTICIPATION TO RESEARCH PROJECTS AND CONVENTIONS

date	January 2016 – Present
Occupation or Position held	PH.D. STUDENT
Project	Member of the Project Identificación basada en objetos de cultivos ortícolas bajo invernadero a partir de estéreo imágenes del satélite orldview-3 yseries temporales de Landsat 8. Referencia: AGL2014-56017-R. Funded by: Ministerio de Economía y Competitividad - Secretaría de Estado de Investigación, Desarrollo e Innovación - Plan Estatal de Investigación Científica y Técnica y de Innovación 2013-2016. Coordinator: Prof. Aguilar Torres, Manuel Angel
Name and Type of Organisation	Escuela Superior de Ingeniería de la Unversidad de Almeria (UAL), Almeria Ctra. Sacramento s/n 04120 – La Cañana de San Urbano Almería, Spain.

RESEARCH INTERESTS

S.S.D. ICAR/06 TOPOGRAPHY AND CARTOGRAPHY 08/A4 - GEOMATIC

Change detection methodologies from remotely sensed passive sensor data ranging from low to very high resolution (geometric, and spectral). Thematic map creation from remotely sensed data aimed at the monitoring of environment, landscape and for culture heritage.

Pre/post- processing of 3D point cloud data (both from active or passive sensors) for in GIS environments aimed at the environmental monitoring.

Data fusion and statistical time series analysis.

Development and implementation of web based informative systems (WebGIS) that implement instantaneous geospatial analysis capabilities.

RESEARCH PRODUCTS

Starting from 2014 Antonio Novelli is author and co-author of international peer reviewed journal papers (WoS – Scopus; **Total IF 2015: 16,949**), international (WoS-Scopus) and national proceedings:

- **10** articles published in international peer reviewed journals (WoS-Scopus). **Five of them with foreign co-authors (*)**;
- **7** (WoS -Scopus) proceedings of international conferences;
- **6** proceedings of national conferences;

Peer reviewed journals (WoS - Scopus)

- * Siad, S. M., Gioia, A., Hoogenboom, G., Iacobellis, V., Novelli, A., Tarantino, E., & Zdruli, P. (2017). Durum Wheat Cover Analysis in the Scope of Policy and Market Price Changes: A Case Study in Southern Italy. *Agriculture*, 7(2), 12. ISSN: 2077-0472 ,DOI: 10.3390/agriculture7020012 (**Scopus**)
- * **NOVELLI, A.**, Aguilar, M. A., Aguilar, F. J., Nemmaoui, A., & Tarantino, E. AssesSeg—A Command Line Tool to Quantify Image Segmentation Quality: A Test Carried Out in Southern Spain from Satellite Imagery. *REMOTE SENSING*, ISSN: 2072-4292, DOI: 10.3390/rs9010040 **IF 2015: 3,036**;
- * Aguilar, M.A., Nemmaoui, A., Aguilar, F. J., **NOVELLI, A.**, García Lorca, A (2017 – in press). Improving georeferencing accuracy of very high resolution satellite imagery using freely available ancillary data at global coverage. *INTERNATIONAL JOURNAL OF DIGITAL EARTH*, DOI: 10.1080/17538947.2017.1280549 **IF 2015: 2,762**;
- Apollonio, C., Balacco, G., **NOVELLI, A.**, Tarantino, E., & Piccinni, A. F. (2016). Land Use Change Impact on Flooding Areas: The Case Study of Cervaro Basin (Italy). *SUSTAINABILITY*, vol 8, issue 10, Article 996, ISSN: 2071-1050. DOI: 10.3390/su8100996 **IF 2015: 1.343**
- * **NOVELLI, A.**, Aguilar, M. A., Nemmaoui, A., Aguilar, F. J., & Tarantino, E. (2016). Performance evaluation of object based greenhouse detection from Sentinel-2 MSI and Landsat 8 OLI data: A case study from Almería (Spain). *INTERNATIONAL JOURNAL OF APPLIED EARTH OBSERVATION AND GEOINFORMATION*, vol 52, pp 403-411. ISSN: 1569-8432. DOI: 10.1016/j.jag.2016.07.011 **IF 2015: 3,798**
- * Aguilar, M. A., Nemmaoui, A., **NOVELLI, A.**, Aguilar, F. J., & García Lorca, A. (2016). Object-Based Greenhouse Mapping Using Very High Resolution Satellite Data and Landsat 8 Time Series. *REMOTE SENSING*, vol 8, Issue 6, Article 513, ISSN: 2072-4292, DOI: 10.3390/rs8060513 **IF 2015: 3,036**
- Caradonna G., **NOVELLI A.**, Tarantino E., Figorito B., Fratino U. (2016). A Webgis Framework for Disseminating Processed Remotely Sensed on Land Cover Transformations. In: *Reports on Geodesy and Geoinformatics 100(1)* · June 2016. Doi: 10.1515/rgg-2016-0004. (**WoS-Scopus**)
- NOVELLI A.**, Tarantino E., Fratino U., Iacobellis V., Romano G., Gentile F. (2016). A data fusion algorithm based on the Kalman filter to estimate leaf area index evolution in durum wheat by using field measurements and MODIS surface

International proceedings (WoS - Scopus)

reflectance data. REMOTE SENSING LETTERS, vol. 7; p. 476-484, ISSN: 2150-704X, DOI: 10.1080/2150704X.2016.1154219. **IF 2015:1,487**

NOVELLI A., Tarantino E. (2015). Combining ad hoc spectral indices based on LANDSAT-8 OLI/TIRS sensor data for the detection of plastic cover vineyard. REMOTE SENSING LETTERS, vol. 6; p. 933-941, ISSN: 2150-704X, DOI: 10.1080/2150704X.2015.1093186. **IF 2015:1,487**

Tarantino E., **NOVELLI A.**, Aquilino M., Figorito B., Fratino U. (2015). Comparing the MLC and JavaNNS Approaches in Classifying Multi-Temporal LANDSAT Satellite Imagery over an Ephemeral River Area. INTERNATIONAL JOURNAL OF AGRICULTURAL AND ENVIRONMENTAL INFORMATION SYSTEMS, vol. 6; p. 83-102, ISSN: 1947-3192, DOI: 10.4018/IJAEIS.2015100105. (**Scopus**)

NOVELLI A. (2016). A data fusion Kalman Filter algorithm to estimate Leaf Area index evolution by using Modis LAI and PROBA-V Top Of Canopy synthesis data. In: Fourth International Conference on Remote Sensing and Geoinformation of the Environment (RSCy2016). Cyprus. DOI: 10.1117/12.2240733. (**WoS-Scopus**)

NOVELLI A., Caradonna G., Tarantino E. (2016). Evaluation of Relative Radiometric Correction techniques on Landsat 8 OLI sensor data. In: Fourth International Conference on Remote Sensing and Geoinformation of the Environment (RSCy2016). Cyprus. DOI: 10.1117/12.2241002 (**WoS-Scopus**)

NOVELLI A., Tarantino E., Caradonna G., Apollonio C., Balacco G., Piccinni AF. (2016). Improving the ANN classification accuracy of Landsat data through spectral indices and linear transformations (PCA and TCT) aimed at LU/LC monitoring of a river basin. In: ICCSA 2016. Pechino. DOI: 10.1007/978-3-319-42108-7_32. (**WoS-Scopus**)

NOVELLI A., Tarantino E. (2015). The contribution of Landsat 8 TIRS sensor data to the identification of plastic covered vineyards. In: Third International Conference on Remote Sensing and Geoinformation of the Environment (RSCy2015). Cyprus, DOI: 10.1117/12.2192095. (**WoS-Scopus**)

Tarantino E., **NOVELLI A.**, Laterza M., Gioia A. (2015). Testing high spatial resolution WorldView-2 imagery for retrieving the leaf area index. In: Third International Conference on Remote Sensing and Geoinformation of the Environment (RSCy2015). Cyprus, DOI: 10.1117/12.2192561. (**WoS-Scopus**)

Aquilino M., **NOVELLI A.**, Tarantino E., Gentile F., Iacobellis V. (2014). Evaluating the potential of GeoEye data in retrieving LAI at watershed scale. In: Proc. SPIE 9239, Remote Sensing for Agriculture, Ecosystems, and Hydrology XVI, 92392B (21 October 2014), DOI: 10.1117/12.2067185. (**WoS-Scopus**)

Caradonna G.; Figorito B.; **NOVELLI A.**; Tarantino E.; Fratino U. Geomatic techniques for disseminating processed remotely sensed open data in an interactive WebGIS. Plurimondi. An International Forum for Research and Debate on Human Settlements. in press.

National proceedings

Peppino C., **NOVELLI A.**, Caradonna G., Pagano A., Tarantino E., Fratino U. (2016) Comparazione di dati pluviometrici e satellitari orientata alla rilevazione delle criticità legate alla desertificazione. In *ATTI CONFERENZA NAZIONALE ASITA. In Press*

Fiore G., Gioia A., Totaro V., CARADONNA G., **NOVELLI A.**, E. Tarantino E., Iacobellis V., Fratino U. (2016). L'utilizzo di immagini satellitari per la definizione di aree inondabili. In *ATTI CONFERENZA NAZIONALE ASITA. ITA. In press*

Caradonna G., Tarantino E., **NOVELLI A.**, Figorito B., Fratino U. (2015). Un WebGIS per la divulgazione delle analisi dei processi di desertificazione del territorio

della Puglia. In: ATTI CONFERENZA NAZIONALE ASITA, p. 217-223, ISBN/ISSN: 978-88-941232-2-7

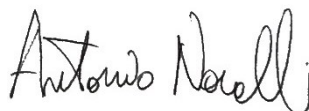
NOVELLI A. (2014). Classificazioni di uso del suolo con Reti Neurali su serie storiche di dati LANDSAT della Puglia settentrionale. In: ATTI CONFERENZA NAZIONALE ASITA. Firenze, 14-16 ottobre 2014, ISBN/ISSN: 978-88-903132-9-5

Laterza M., **NOVELLI A.**, Tarantino E., Gioia A. (2014). Potenzialità del sensore WorldView-2 nella stima del Leaf Area Index (LAI). In: ATTI CONFERENZA NAZIONALE ASITA. Firenze, 14-16 ottobre 2014, ISBN/ISSN: 978-88-903132-9-5

Figorito B., Mancini F., **NOVELLI A.**, Tarantino E. (2014). Monitoring land cover changes at watershed scale using LANDSAT imagery. 1st WORKSHOP on the State of the art and Challenges Of Research Efforts @POLIBA December 3 - 5, 2014 - Politecnico di Bari, Italy. p. 215-219, ROMA: Gangemi, ISBN/ISSN: 978-88-492-2966-0

**BARI, 28 FEBBRAIO
2017**

FIRMA



Il sottoscritto ANTONIO NOVELLI, CODICE FISCALE: NVLNTN87T14D643I, NATO A FOGGIA PROV. FOGGIA IL 14/12/1987, ATTUALMENTE RESIDENTE A RIGNANO GARGANICO PROV. FOGGIA, IN VIA RENATO GUTTUSO N.2 C.A.P. 71010, TELEFONO (Prefisso) 340 NUMERO 4236442,

Consapevole che chiunque rilasci dichiarazioni mendaci, forma atti falsi o ne fa uso è punito ai sensi del codice penale e delle leggi speciali in materia, dichiara che quanto sopra corrisponde a verità ai sensi degli art. 46 e 47 del D.P.R. n. 445/2000.

Dichiara inoltre di essere informato, ai sensi e per gli effetti di cui al Decreto Legislativo 196/2003 che i dati personali raccolti saranno trattati, anche con strumenti informatici, esclusivamente nell'ambito del procedimento per il quale le presenti dichiarazioni vengono rese.